



Review

Recent development of lithium argyrodite solid-state electrolytes for solid-state batteries: Synthesis, structure, stability and dynamics

Chuang Yu^{a,b,1}, Feipeng Zhao^{a,1}, Jing Luo^{a,1}, Long Zhang^c, Xueliang Sun^{a,*}^a Department of Mechanical and Materials Engineering, The University of Western Ontario, London, Ontario N6A 5B9, Canada^b State Key Laboratory of Advanced Electromagnetic Engineering, while the 48neering and Technology, School of Electrical and Electronic Engineering, Huazhong University of Science and Technology, Wuhan 430074, China^c State Key Laboratory of Metastable Materials Science and Technology, Yanshan University, Qinhuangdao, Hebei 066004, China

ARTICLE INFO

Keywords:

Solid-state batteries

Lithium argyrodite

Synthesis

Structure

Dynamics

Stability

ABSTRACT

Solid electrolyte plays a key role to enable good safety reliability and high performance of all-solid-state lithium batteries. Among the diverse solid electrolytes, argyrodites represent a relatively new and promising class of sulfide-based lithium-ion superconductors due to their high ionic conductivity at room temperature, low cost and good compatibility towards Li metal. However, lithium argyrodites remain challenging for practical applications despite of the continuous improvements from research. Herein, we review the recent research advancements and limitations of lithium argyrodites from material to battery level. Material synthesis based on solid and liquid routes are summarized. The chemical structures of lithium argyrodites, their lithium-ion transport mechanism and various optimization strategies for high ionic conductivity are discussed. The chemical and electrochemical stabilities of lithium argyrodites towards cathode and anode materials and corresponding improvement approaches are discussed in detail. The perspectives on future research directions of lithium argyrodites are provided.

1. Introduction

Due to the high energy and power densities, lithium-ion batteries have attracted great attentions and been widely applied in many markets such as mobile electronic devices and electric vehicles [1–3]. Due to the presence of flammable liquid electrolytes, the currently commercial lithium batteries suffer safety issues [4–8]. Lithium batteries for electric vehicles require safer batteries with higher energy density to extend the driving distance, deliver higher power density to shorten the charging time, maintain longer cycling lives to reduce the maintenance cost [9, 10]. Higher energy density is achieved by increasing the battery size or the number of packing cells, which also means increasing the amount of flammable electrolytes in the device that casts more serious safety concern [5,11]. Replacement of the flammable liquid electrolytes with a non-flammable solid electrolyte is a feasible way to improve the safety of batteries [12–16]. In the absence of hazardous and flowable organic solvents, the use of solid electrolytes can also simplify the battery design [11,13,17,1819]. Direct stacking of multiple layers of solid-state batteries in one package can provide a high operating voltage and economize

the effective cell volume, paving the way for electric vehicle applications [7,15,18,20–22].

However, one of the key issues in the development of solid-state batteries is to obtain a solid electrolyte with high lithium-ion conductivity at room temperature [14,21]. In recent years, significant efforts have been invested to explore new families of inorganic solid electrolytes includes sulfides [23–26], nitrides [27,28], hydrides [29–31] halides [32–34], phosphates [35], and oxides [11,14,17,20,36]. Due to the larger ionic radius and more polarizability of S^{2-} compared to O^{2-} , sulfide based lithium solid electrolytes generally show higher ionic conductivities than most oxide based solid electrolytes, delivering a high conductivity of over 10^{-4} S/cm at room temperature [14]. Moreover, the sulfide based electrolytes usually have lower melting temperature and require lower synthesis temperature compared to the oxides and phosphates, leading to a low grain boundary resistance and good contact with electrodes at accessible conditions. Several sulfide-based electrolytes have been developed with comparable or even higher Li^+ conductivity than many liquid electrolytes. For examples, $Li_{10}GeP_2S_{12}$ (12 mS/cm) [37], $Li_{9.54}Si_{1.74}P_{1.44}S_{11.7}Cl_{0.3}$ (25 mS/cm) [38], and

* Corresponding author.

E-mail address: xsun9@uwo.ca (X. Sun).¹ The authors contribute equally to this work.

$\text{Li}_{5.5}\text{PS}_{4.5}\text{Cl}_{1.5}$ (12 mS/cm) [39] demonstrate a room-temperature Li^+ conductivity above 10^{-2} S/cm.

An important family of sulfide electrolytes is lithium argyrodite $\text{Li}_6\text{PS}_5\text{X}$ (X = Cl, Br). Low cost and high Li^+ conductivity (above 10^{-3} S/cm) at room temperature make argyrodites a promising group of solid electrolytes for solid-state battery [40–52]. The first reported argyrodite-type ion conductor was Ag_8GeS_6 with a high Ag^+ ionic conductivity and mobility. The Ag^+ in the structure can be substituted by other cations (e.g. Cu^+), while the argyrodite structure can be maintained after substitution of Ge and S by P and halogens, yielding fast Ag^+ or Cu^+ ion conductors such as $\text{A}_7\text{PS}_5\text{X}$ (A = Ag^+ , Cu^+ ; X = Cl, Br) [40, 53]. The similar ionic radii of Cu^+ provide the possibility of partial or full substitution of Cu^+ by Li^+ ions in the argyrodite structure for lithium argyrodites. Deiseroth et al. [40] have reported the analogous cubic lithium argyrodites with formulas of Li_7PS_6 and $\text{Li}_6\text{PS}_5\text{X}$ (X = Cl, Br, I). ^7Li NMR and impedance results showed that the room temperature Li^+ conductivities of $\text{Li}_6\text{PS}_5\text{X}$ (X = Cl, Br, I) are in the range of 10^{-2} to 10^{-3} S/cm, which makes these materials a potential candidate of solid electrolyte used for solid-state batteries. Fig. 1 shows a timeline of the development of lithium argyrodites from 2007 to date with key milestones.

We will comprehensively review the recent developments of lithium argyrodite solid electrolytes from their synthesis, structure, composition, ion conduction mechanism, to applications in solid-state batteries (Fig. 2). Different synthesis routes, including mechanical milling, classical mechanical milling followed by annealing, the direct solid-state sintering and the liquid phase route are summarized. The structure, compositions, lithium-ion conduction mechanisms of lithium argyrodites and effective methods to improve the ionic conductivity are discussed. Moreover, the compatibility of lithium argyrodites with different cathode active materials (e.g., S, Li_2S , $\text{LiMn}_x\text{Ni}_y\text{Co}_z\text{O}_2$ [$x + y + z = 1$; $0 < x, y, z < 1$] and LiCoO_2) and various anode materials (such as Li, In, $\text{Li}_4\text{Ti}_5\text{O}_{12}$) are systematically compared. Interfacial engineering strategies and lithium-ion transport behaviors in lithium argyrodites-based solid-state batteries, from the bulk electrolyte to the electrolyte-electrolyte interface and to electrode-electrolyte interface, are revealed.

2. Synthesis routes for lithium argyrodites

To promote the use of lithium argyrodites in solid-state batteries, it is important to be able to manufacture the materials with high Li^+ conductivity via a simple synthesis route. Synthesis methods for lithium argyrodite solid electrolytes commonly involve mechanical milling, classical mechanical milling followed by annealing, the direct solid-state sintering and the liquid phase route, as summarized in Fig. 3. The Li^+ conductivity values of lithium argyrodites obtained from different synthesis methods are summarized in Table S1 of Supplementary Information.

2.1. Mechanical milling route

Mechanical milling is a common method for preparing lithium argyrodites. Stoichiometric mixture of the raw materials is ball-milled at a low rotational speed to mix the precursors homogeneously and then followed by high-speed ball-milling for a long duration to generate the final product. At low rotational speeds (e.g., 110 rpm), the mechanical milling process generate a uniform mixture of precursor with reduced particle size. At high rotational speeds (e.g., 500 rpm), the high energy can break chemical bonds of the precursor compounds and mix materials to the atomic level, forming designated sulfide-based solid electrolytes after certain milling duration at a high rotation speed. Previous studies showed that crystalline argyrodites $\text{Li}_6\text{PS}_5\text{X}$ (X = Cl, Br, I) can be achieved by high-energy mechanical milling process without post heat-treatment, generating argyrodite electrolytes with high Li^+ conductivities at room temperature. However, there is a huge amount of amorphous phase in the milled lithium argyrodites which may have a great influence on the ionic conductivity and its applications.

The high-energy mechanical milling process require a delicate balance between the weights of total milling balls and the chemical precursors. Rao et al. [41] reported that the ball-milled products showed XRD patterns with partial argyrodite crystallinity and signs of residual precursors (Li_2S , P_2S_5 and LiX (X = Cl, Br, I)). Even after 24 h of ball-milling, the precursor phases were still rather prominent. However,

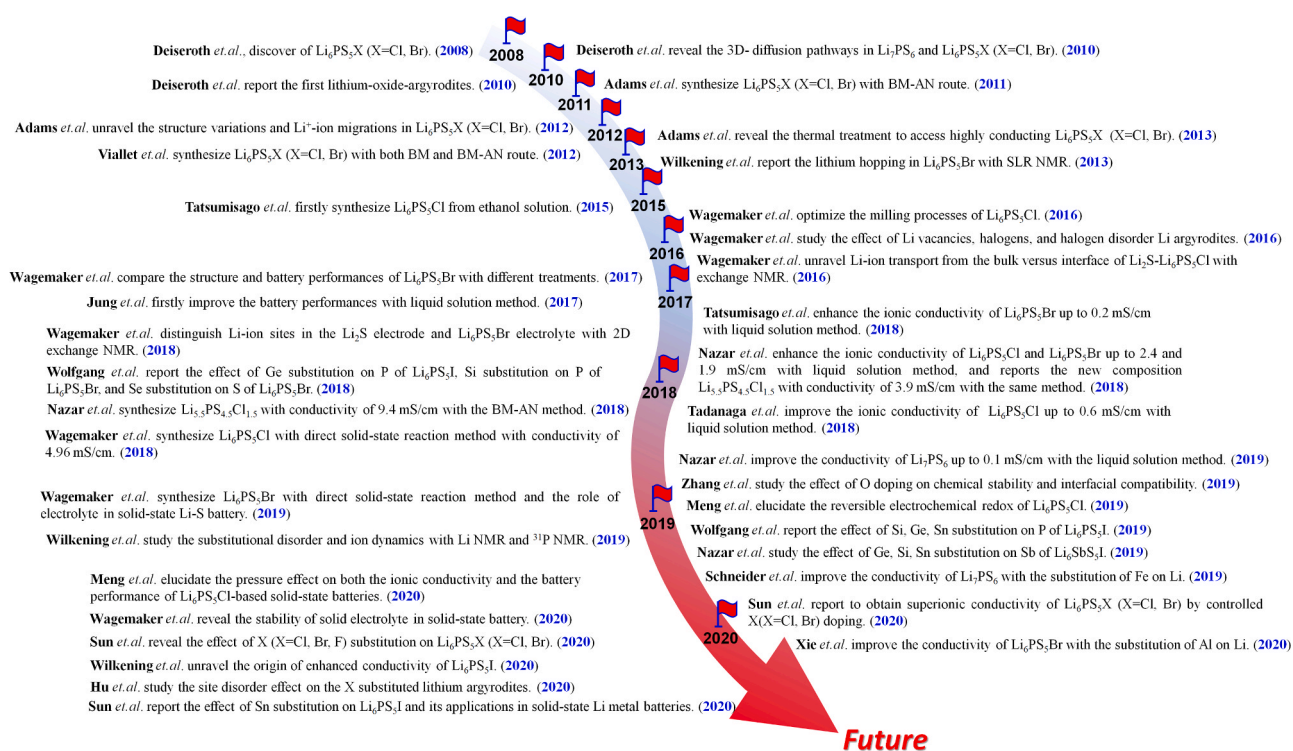


Fig. 1. The development of lithium argyrodites.

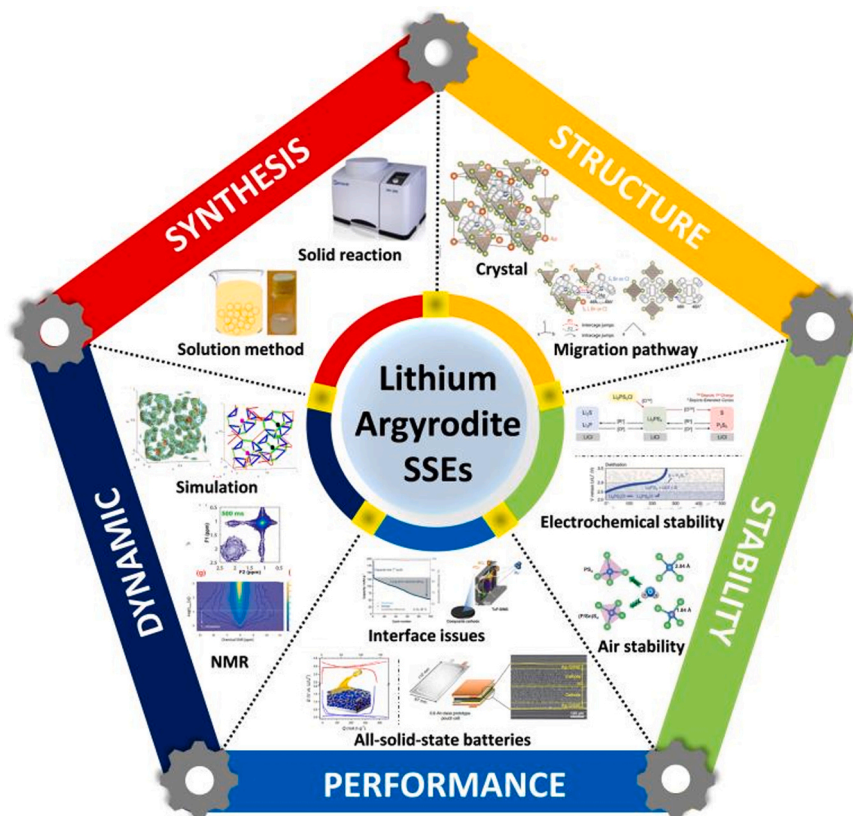


Fig. 2. Schematic summary of the contents in this review.

in other reported works, broadened diffraction peaks of lithium argyrodite phases are indexed, suggesting the formation of lithium argyrodite via mechanical milling route (also called mechanochemical milling route) [44,50,51]. Such different results are associated with the energy effectiveness of the mechanical milling process, which is highly affected by the materials, the number and sizes of balls, the weight ratio of total balls and precursors and milling speed/energy. Rao's milling experiments were performed in an agate jar using 15 agate balls with a diameter of 10 mm corresponding to an overall mass of 13.9 g [41]. In comparison, Boulineau et al. successfully obtained pure argyrodite products when they used 15 zirconia balls with a diameter of 10 mm correspond to an overall mass of 29.8 g [44]. Moreover, Yu et al. [50] used 10 tungsten carbide (WC) balls with the same diameter and a total mass of 80.0 g to perform the milling process in a WC coated (inner) stainless steel jar and obtained the pure lithium argyrodite phase after 10 h milling at 500 rpm. It should be noticed that the weight ratio of the balls and the raw materials in Boulineau's and Yu's were quite large, 29.8 and 40, respectively, suggesting the importance of ball-to-precursor ratio for obtaining a pure phase of lithium argyrodite with a high lithium-ion conductivity. The purity of the milled lithium argyrodite has a directly correlate to the ionic conductivity, which are associated with the milling parameters applied during milling process.

In addition to the ball-to-precursor weight ratio, the rotational speed for milling is also a critical parameter affecting the final product. Using similar agate balls as Rao et al. [41,42] did, Zhang et al. [51] successfully obtained pure-phase $\text{Li}_6\text{PS}_5\text{Cl}$ with a room-temperature Li^+ conductivity of 6.1×10^{-4} S/cm by increasing the rotational speed to 600 rpm (vs. 510 rpm), extending the milling duration (24 h vs. 20 h), and raising the ball-to-precursor weight ratio. Using zirconia balls and a balls-to-precursor weight ratio of 29.8, the ball-milled $\text{Li}_6\text{PS}_5\text{X}$ (X = Cl, Br, I) was prepared under a rotational speed of 600 rpm for 20 h, exhibiting a high conductivity of $2\text{--}7 \times 10^{-4}$ S/cm with an activation energy of 0.3–0.4 eV [44]. When WC balls were used with a

ball-to-precursor weight ratio of 40, pure $\text{Li}_6\text{PS}_5\text{Cl}$ and $\text{Li}_6\text{PS}_5\text{Br}$ were synthesized at 550 rpm for 16 h and 500 rpm for 15 h, respectively [47, 50]. The corresponding room-temperature Li^+ conductivity of $\text{Li}_6\text{PS}_5\text{Cl}$ and $\text{Li}_6\text{PS}_5\text{Br}$ were 1.0×10^{-3} S/cm and 6.2×10^{-4} S/cm, respectively. The kinetic energy of the balls is a function of their mass and velocity. Dense materials (such as steel or tungsten carbide) provide more energy than light materials (such as ceramics, zirconia and agate) [54]. During the mechanical milling process, a larger number of balls with the same diameter distribution means more energy, significantly influencing the physical and chemical properties of the final product. The required milling duration is interrelated to the choice of balls and the ball-to-precursor ratio. Last but not least, different types of milling equipment also have influence on the ball-milled product. According to several recent studies, high energy planetary ball mill (Fritsch, Pulverisette 7) is preferred [44,50,51].

Overall, mechanical milling is a promising synthesis route for lithium argyrodites, but there are still some drawbacks to be considered. The amount of product is limited by the size of the ball-milling jars. The high rotational speed and long duration of milling process could be time- and energy-consuming that should contribute to the manufacturing cost [46]. Moreover, the low densities of the starting materials make the mixture strongly adhesive to the balls and the inner wall of the jar that increase difficulty in handling and cause unnecessary weigh loss [46, 51].

2.2. Mechanical milling with post annealing

Mechanical milling followed by annealing is a typical method used to synthesize sulfide-based and oxide solid electrolytes. The starting materials are ball milled with high rotational speed to form a largely amorphous preliminary electrolyte, pressed into pallets and sealed in an ampule, then annealed in a furnace to get the final product. For lithium argyrodite electrolytes, this method is widely chosen for a resulting high

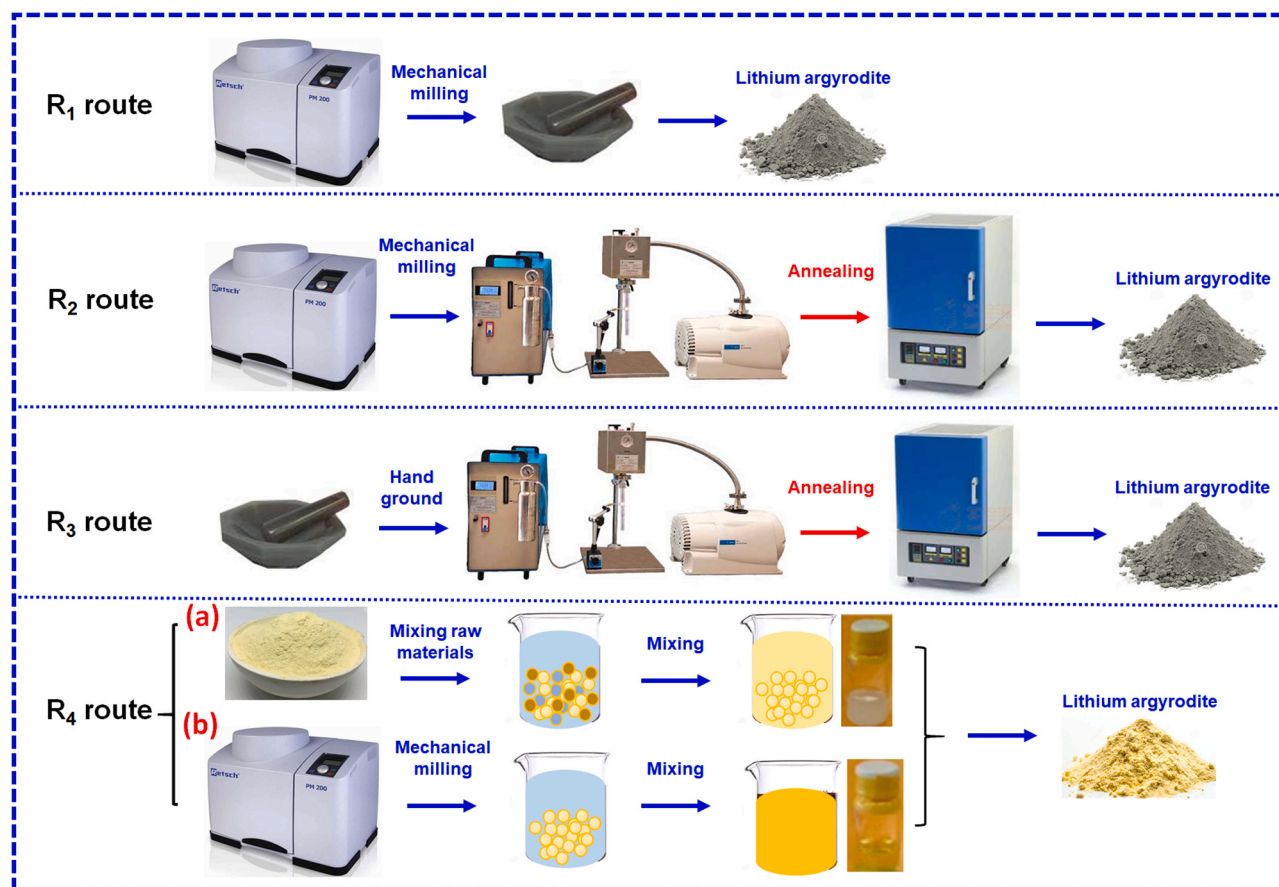


Fig. 3. Schematics of different synthesis routes for lithium argyrodite electrolytes, including the mechanical milling route (R_1), the mechanical milling followed by annealing route (R_2), the solid-state sintering route (R_3) and the liquid-phase method (R_4). The R_4 route can be divided into two sub-approaches: (a) the suspension synthesis approach involves suspending the starting materials, such as Li_2S , P_2S_5 and LiX ($X = \text{Cl, Br, I}$) in organic solvents; these starting materials form complexes in the organic solution, which can be precipitated through heating and evaporation of the solvent; (b) the dissolution-precipitation approach directly dissolves $\text{Li}_6\text{PS}_5\text{X}$ ($X = \text{Cl, Br, I}$) solid electrolytes in an organic solvent, and the solid $\text{Li}_6\text{PS}_5\text{X}$ is retrievable after removal of solvent [56].

room-temperature Li^+ conductivity that usually exceeds 10^{-3} S/cm.

Rao et al. [41] first reported the successful synthesis of $\text{Li}_6\text{PS}_5\text{X}$ ($X = \text{Cl, Br, I}$) via mechanical milling and post annealing route. Among the $\text{Li}_6\text{PS}_5\text{X}$ argyrodites, $\text{Li}_6\text{PS}_5\text{Cl}$ showed an ionic conductivity in the order of 10^{-4} S/cm at room temperature. Although this ionic conductivity is acceptable in the sulfide glassy electrolyte family, it is still much lower than that of the conventional liquid electrolytes (LiPF_6 in various carbonates). The low Li^+ conductivity may be associated with the materials of the balls using during the milling process. Agate is a light material, which is hard to provide high energy especially with a small amount of balls and simple distribution of ball sizes. Later, Boulineau et al. [44] chose the heavier zirconia balls for the mechanical milling process and introduced a post annealing step. After ball-milling at a rotational speed of 600 rpm for 20 h, the resultant powder was subsequently annealed at 550°C for 10 h, yielding $\text{Li}_6\text{PS}_5\text{Cl}$ electrolyte with an ionic conductivity of 1.33×10^{-3} S/cm at room temperature. Yu et al. [47,50] used even heavier WC balls for the milling process at lower rotation speeds (550 and 500 rpm) for much shorter milling durations (16 and 15 h) to prepare $\text{Li}_6\text{PS}_5\text{Cl}$ and $\text{Li}_6\text{PS}_5\text{Br}$ electrolytes. The resultant powders were annealed at 550°C for 5 h and 300°C for 5 h, respectively, showing 1.10×10^{-3} S/cm and 1.11×10^{-3} S/cm at room temperature. Obviously, the annealing treatment after ball milling can significantly improve the Li^+ conductivity of lithium argyrodite electrolytes. Although the argyrodite electrolytes with or without annealing exhibit similar diffraction patterns, the mechanical milling process may introduce numerous grain boundaries (small particle size) and partial amorphization that could lead to suboptimal Li^+ conductivity of the

argyrodite electrolytes [47]. The major phase of lithium argyrodites obtained via this synthesis route is the crystal, while a small amount of the amorphous may also exist in the sample due to the incomplete sintering during the annealing process.

To unravel the phase evolution of $\text{Li}_6\text{PS}_5\text{Cl}$ during the annealing process, in-situ neutron diffraction was performed on a stoichiometric mixture of precursors after ball-milling [42]. The results showed that an argyrodite phase was formed between 80 and 150°C with a moderate ionic conductivity and heat treatment at higher temperatures can further obtain the highly conducting phase. The initial conductive phase was identified as Li_7PS_6 , which was gradually converted into $\text{Li}_6\text{PS}_5\text{Cl}$ at higher temperature with larger Li^+ conductivity by annealing. Impedance analysis results showed that to reach a room temperature conductivity of 1 mS/cm and a low activation energy of 0.16 eV samples had to be heat-treated at least at 250°C [42]. Lithium argyrodite phase with highly conducting phase and optimal halogen ordering over 4a and 4c sites ratio is closely related to the annealing parameters, which are vital to achieving high ionic conductivity.

2.3. Solid-state sintering

Solid-state sintering is an easy route to synthesize lithium argyrodite electrolytes by thermal sintering precursors in an ampule. The mixture of the precursors could be hand grinded or ball-milled at low rotational speed pressed into pallets prior to sealing into ampules. Sintering duration, feeding composition of precursors and sintering temperature are important parameters for the success of obtaining argyrodite

electrolytes with a high ionic conductivity.

Early research achieved to obtain pure phase of lithium argyrodite via the solid-state reaction at 550 °C for 7 days [40]. However, such long annealing durations is energy- and time-consuming. Recent research reported by different groups found that the pure phase of $\text{Li}_6\text{PS}_5\text{X}$ ($\text{X} = \text{Cl}, \text{Br}$) can be obtained in a much shorter annealing duration [46, 51]. Yu et al. [46] reported a $\text{Li}_6\text{PS}_5\text{Cl}$ electrolyte with an ionic conductivity of 4.96×10^{-3} S/cm at 26.2 °C can be synthesized by annealing at 550 °C for 10 h. The Li^+ conductivity was higher than that of the $\text{Li}_6\text{PS}_5\text{Cl}$ electrolyte prepared by the classic mechanical milling and annealing combination route. The high Li^+ conductivity was confirmed by both temperature-dependent AC impedance and spin-lattice relaxation ^7Li NMR analyses. More specifically, Wang et al. [55] demonstrated a $\text{Li}_6\text{PS}_5\text{Cl}$ electrolyte with a room-temperature ionic conductivity of 3.15×10^{-3} S/cm by sintering the mixture of precursors at 550 °C for just 10 min, which was very close to the optimal ionic conductivity up to 3.43×10^{-3} S/cm at room temperature that achieved by sintering for 15 h.

Zhang et al. [51] compared the synthesis of $\text{Li}_6\text{PS}_5\text{X}$ ($\text{X} = \text{Cl}, \text{Br}, \text{I}$) between solid-state sintering and mechanical alloying. The solid-state sintering route preferred excess feeding of the Li_2S precursor, while the mechanical alloying route favored stoichiometric feeding of precursors for high-purity products and high Li^+ conductivity. Moreover, the $\text{Li}_6\text{PS}_5\text{X}$ electrolytes synthesized by solid-state sintering showed much higher Li^+ conductivities than those obtained by mechanical milling. Among all $\text{Li}_6\text{PS}_5\text{X}$ electrolytes, the solid-state sintered $\text{Li}_6\text{PS}_5\text{Cl}$ showed the highest ionic conductivity. Recently, Yu et al. [48] suggested that the optimal annealing temperature for $\text{Li}_6\text{PS}_5\text{Br}$ was 550 °C that gave a high Li^+ conductivity of 2.58×10^{-3} S/cm. The origin of the high ionic conductivity was due to its high purity, small mean lithium ion jumps, and the optimal Br ordering over 4a and 4c sites. Although the solid-state reaction route for lithium argyrodites $\text{Li}_6\text{PS}_5\text{X}$ ($\text{X} = \text{Cl}, \text{Br}, \text{I}$) is easy to scale, there are still some problems hindering the wide application of this synthesis route. Homogeneity of the solid-state sintered products could be a concern. Lithium argyrodite synthesized from this route is highly crystalline crystals with almost no amorphous phase due to the high sintering temperature and long annealing durations without a mechanical milling process.

2.4. Liquid-phase utilization

Liquid-phase synthesis route has many advantages over the above three solid-state methods in terms of synthesis temperature, duration and scalability. The liquid-phase synthesis route can also be a promising method to fabricate composites of electrode materials and solid electrolytes with good interfacial contact, which is vital for good solid-state battery performance. Practical battery companies would be very interested. Additionally, liquid-phase reaction method is an effective method to synthesize solid electrolytes particle with controllable particle size (from micro to nano scale) and morphology. Tuning of related properties for electrolytes becomes possible.

There are two typical liquid-phase approaches to synthesize lithium argyrodite electrolytes. One approach is to choose an organic solvent that is not soluble to the precursors to disperse the reactants. More specifically, the precursors Li_2S , P_2S_5 and LiX ($\text{X} = \text{Cl}, \text{Br}, \text{I}$) are dispersed in an organic solvent as a suspension; after removing the organic solvent by heat, the yielded powder is annealed to obtain lithium argyrodites. The other approach undergoes a dissolution-precipitation process. Lithium argyrodite solid electrolyte (prepared by mechanical milling with high rotation speed) is dissolved in an organic solvent to form a lithium argyrodite solution, where the lithium argyrodite is retrievable after removal of the organic solvent and annealing.

A liquid-phase method to prepare lithium argyrodite was first reported in 2015. Yubuchi et al. [57] successfully prepared a $\text{Li}_6\text{PS}_5\text{Cl}$ solid electrolyte using the dissolution-reprecipitation process with

ethanol solution, showing a room temperature lithium ionic conductivity of 1.4×10^{-5} S/cm and an activation energy of 0.342 eV. Similarly, $\text{Li}_6\text{PS}_5\text{Br}$ was also retrievable after a liquid-phase process [58]. Preparation parameters such as different alcohol solvents, dissolution times and drying temperatures were carefully investigated. Drying temperature was crucial for the complete removal of residual organic impurities and for obtaining a highly crystalline argyrodite, so that a high Li^+ conductivity can be ensured. The $\text{Li}_6\text{PS}_5\text{Br}$ solid electrolytes dried at 80, 150 and 200 °C exhibited increasing Li^+ conductivities (and activation energies) of 5.5×10^{-5} S/cm (0.415 eV), 1.9×10^{-4} S/cm (0.332 eV) and 2.5×10^{-4} S/cm (0.311 eV), respectively [58]. Moreover, to tailor the particle size and the shape of sulfide solid electrolytes during dissolution, the addition of dispersant in the mixture of acetonitrile and ethanol can effectively result in a homogenous and submicron-sized $\text{Li}_6\text{PS}_5\text{Cl}$ particles. $\text{Li}_6\text{PS}_5\text{Cl}$ synthesized without or with via liquid-phase route showed a room-temperature Li^+ conductivity of 3.0×10^{-4} S/cm and 6.0×10^{-4} S/cm, respectively [59]. However, it should be noted that the precipitation of high-purity lithium argyrodite requires a pure-phase lithium argyrodite (which could be obtained by high-energy mechanical milling) in the first place.

Another liquid-phase approach to apply lithium argyrodites can be achieved via suspension. A designated material is dispersed in the suspension of argyrodite electrolytes or their precursors; subsequently, evaporation of the solvent and appropriate annealing can result in a composite of the desired material and lithium argyrodite electrolyte. Recently, Ziolkowska et al. [60] demonstrated that removal of the solvent from a solution of Li_2S and P_2S_5 in acetonitrile followed by heat treatment resulted in $\beta\text{-Li}_3\text{PS}_4$. A high-purity Li_7PS_6 argyrodite solid electrolyte was synthesized through stoichiometric chemical reaction of Li_2S and $\beta\text{-Li}_3\text{PS}_4$ in ethanol medium. The Li_7PS_6 electrolyte showed a high room-temperature ionic conductivity of 1.1×10^{-3} S/cm, which is much higher than Li_7PS_6 synthesized by conventional route. Chida et al. [61] prepared $\text{Li}_6\text{PS}_5\text{Br}$ by ultrasonically Li_2S , P_2S_5 and LiBr in ethyl propionate-ethanol and subsequent heating at 453 K, showing a room-temperature ionic conductivity of 3.4×10^{-5} S/cm. Zhang et al. [62] synthesized $\text{Li}_6\text{PS}_5\text{Cl}$ through dissolving Li_2S , P_2S_5 and LiCl in ethanol solvent followed by heat treatment, demonstrating a room-temperature ionic conductivity of 2.1×10^{-4} S/cm.

By adjusting the feeding sequence of precursors and careful selection of solvents, morphological control of the synthesized lithium argyrodite electrolytes and further improvement of their ionic conductivity are possible. Choi et al. [63] have successfully synthesized rod-like $\text{Li}_6\text{PS}_5\text{Cl}$ with a high room-temperature conductivity of 1.1×10^{-3} S/cm by controlling the feeding sequence of precursors. The starting materials (Li_2S and LiCl) with low solubilities were first stirred into ethyl acetate followed by addition of P_2S_5 . Drying the solution at 30 °C for 12 h to completely remove the ethyl acetate and then heating at 550 °C for 5 h gave the final $\text{Li}_6\text{PS}_5\text{Cl}$ electrolyte. In order to further improve the ionic conductivity of lithium argyrodite prepared by the liquid-phase route, Yubuchi et al. [56] designed a four-step liquid-phase synthesis route to prepare $\text{Li}_6\text{PS}_5\text{Br}$. Part of the starting materials Li_2S and P_2S_5 with a molar ratio of 3:1 was first dispersed in super-dehydrated tetrahydrofuran (THF) to obtain a Li_3PS_4 precursor-containing suspension in THF. Separately, the rest of Li_2S and LiBr with the target molar ratio were dissolved in anhydrous ethanol (EtOH) to form a solution. This obtained solution was mixed with the THF suspension to get a pale green precursor solution of $\text{Li}_6\text{PS}_5\text{Br}$ in THF-EtOH. Finally, the organic solvents were removed from the solution and the resultant powder was heated at 550 °C to get the final product. A high ionic conductivity of 3.1×10^{-3} S/cm at room temperature was demonstrated. Meanwhile, Zhou et al. [64] used a similar liquid-phase method to prepare $\text{Li}_{6-y}\text{PS}_{5-y}\text{Cl}_{1+y}$ ($y = 0-0.5$), showing a high Li^+ conductivity up to 3.9×10^{-3} S/cm at room temperature.

Overall, liquid-phase synthesis routes for lithium argyrodite electrolytes have been demonstrated viable and have many advantages including low synthesis temperature, short duration, scalability and

applicability for composites synthesis. Nevertheless, there are still some concerns to be addressed. Firstly, lithium argyrodites are sensitive to air and moisture, so the synthesis process and conditions are usually demanding. Secondly, the organic solvents are toxic and require strict handling procedures for manufacturing scale up. Last but not least, the low solubilities of the starting materials and the unclear/incomplete reaction mechanism can lead to unknown impurities that ultimately limit the performance of the argyrodite electrolytes. More research efforts are required to reveal the underlying mechanism, thus to improve the electrolyte performance and synthesis process. The sample obtained from this route is also a mixture of crystal and amorphous phase due to the low annealing temperature.

3. Structure, dynamics and new compositions of lithium argyrodite

3.1. Structure and lithium conduction mechanism of $\text{Li}_6\text{PS}_5\text{X}$ ($\text{X} = \text{Cl}, \text{Br}, \text{I}$)

Lithium argyrodites electrolytes $\text{Li}_6\text{PS}_5\text{X}$ ($\text{X} = \text{Cl}, \text{Br}, \text{I}$) have a cubic $F43m$ face centered (fc) symmetry. The crystal structure of $\text{Li}_6\text{PS}_5\text{X}$ is displayed in Fig. 4a. In the structure, the S^{2-} and Cl^-/Br^- anions form a face-centered cubic lattice (the 4a and 4d sites) and PS_4^{3-} tetrahedra on the octahedral sites (P on the 4b site). The S^{2-} and X in $\text{Li}_6\text{PS}_5\text{X}$ can occupy three different crystallographic positions, where the 16e site is

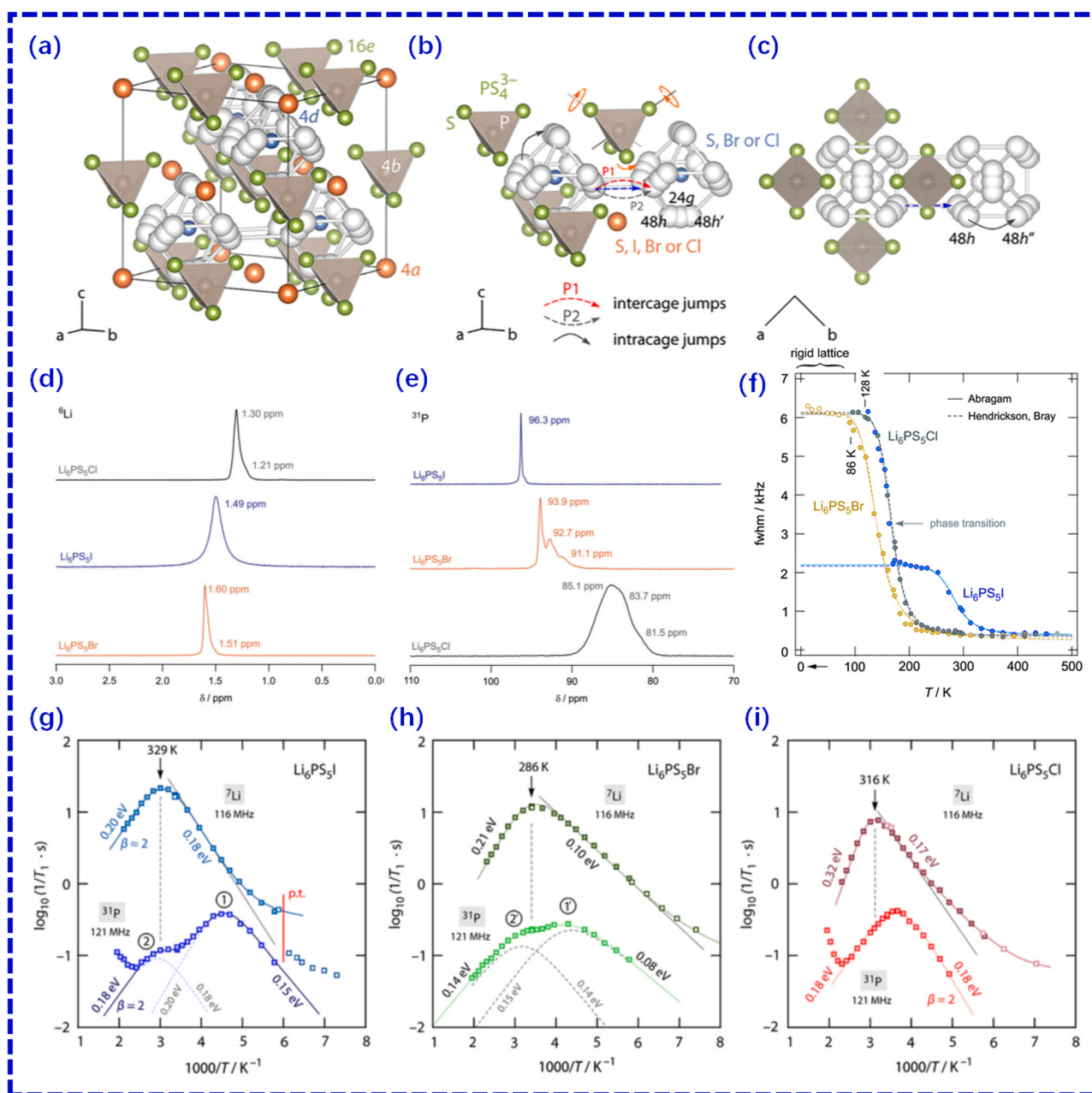


Fig. 4. (a) Crystal structure of lithium argyrodite $\text{Li}_6\text{PS}_5\text{X}$ ($\text{X} = \text{Cl}, \text{Br}, \text{I}$). (b) The intra-cage and inter-cage lithium diffusion pathways in $\text{Li}_6\text{PS}_5\text{X}$ ($\text{X} = \text{Cl}, \text{Br}, \text{I}$). The lithium hopping is influenced by S^{2-} anions of a nearby PS_4^{3-} tetrahedral, while the lithium jumping distance depends on the lattice constant and halogen substitution. (c) The structure of lithium argyrodite viewed along the c -axis. Two S^{2-} anions of the PS_4^{3-} tetrahedra are located slightly above the direct 48–48 h exchange pathway. (d) ^6Li MAS NMR spectra of $\text{Li}_6\text{PS}_5\text{Cl}$, $\text{Li}_6\text{PS}_5\text{Br}$ and $\text{Li}_6\text{PS}_5\text{I}$ recorded at 73.6 MHz and a spinning speed of 25 kHz. (e) ^{31}P MAS NMR spectra of $\text{Li}_6\text{PS}_5\text{Cl}$, $\text{Li}_6\text{PS}_5\text{Br}$ and $\text{Li}_6\text{PS}_5\text{I}$ recorded at 202.4 MHz and a spinning frequency of 25 kHz. (f) Temperature-dependent of the ^7Li NMR line widths of lithium argyrodites $\text{Li}_6\text{PS}_5\text{X}$ ($\text{X} = \text{Cl}, \text{Br}, \text{I}$). The comparison of the ^{31}P spin-lattice relaxation NMR rate peaks ($1/T_1$) for $\text{Li}_6\text{PS}_5\text{Cl}$, $\text{Li}_6\text{PS}_5\text{Br}$, and $\text{Li}_6\text{PS}_5\text{I}$. Diffusion-induced ^7Li (116 MHz) and ^{31}P (121 MHz) spin-lattice relaxation NMR rates as a function of temperature of (g) $\text{Li}_6\text{PS}_5\text{I}$, (h) $\text{Li}_6\text{PS}_5\text{Br}$ and (i) $\text{Li}_6\text{PS}_5\text{Cl}$ [65,66].

fully occupied by S^{2-} anions and the 4a and 4b sites are shared by the S^{2-} and X^- anions. Due to the similar ionic radii of S^{2-} (170 pm) and Cl^- (167 pm)/ Br^- (182 pm), the site disorder between S^{2-} and Cl^-/Br^- anions are observed in Li_6PS_5Cl and Li_6PS_5Br .

Three different types of lithium-ion jumps have been identified in the lithium argyrodite structure for Li^+ conduction (Fig. 4b and 4c), including the short-range back-and-forth transitions (48h-48h), the short-range intra-cage transitions between different 48 h pairs and the long-range inter-cages transitions interconnecting the four cages in each Li_6PS_5X unit cell. Macroscopic Li^+ conductivity is achieved by the occurrence of all three types of jumps, with the slowest jumping type as the rate limiting step.

Magic angle spinning (MAS) NMR is a powerful tool for understanding the structure and ion conduction mechanism of solid electrolytes. As shown in Fig. 4d, 6Li MAS NMR spectra of Li_6PS_5Cl and Li_6PS_5Br show a slightly asymmetric line with isotropic chemical shift (δ_{iso}) of 1.3 and 1.6 ppm, respectively, while the line of Li_6PS_5I shows a much more symmetric NMR line shape and line broadening. The 6Li MAS NMR spectra of Li_6PS_5Br , Li_6PS_5I and Li_6PS_5Cl show an increasing δ_{iso} value in order. The electron density distribution in the direct neighborhood of the Li spins for Li_6PS_5X is significantly influenced by the halogen anions. Li_6PS_5Br delivers the highest electron density among those three compositions. ^{31}P MAS NMR was applied to investigate the local structures of Li_6PS_5X (Fig. 4e). The ^{31}P MAS NMR resonance of Li_6PS_5I shows a sharp NMR line shape centered at $\delta_{iso} = 96.3$ ppm, indicating an ordered anion framework with I anions non-randomly occupying selected crystal sites. The small shoulders in the ^{31}P MAS NMR spectra of Li_6PS_5I near the major chemical shift line is associated with the P defect sites in the synthesized material. The broadened ^{31}P MAS NMR line of Li_6PS_5Cl ranging from 85 to 81 ppm reveal an anion disorder in Li_6PS_5Cl structure. In comparison, the ^{31}P MAS NMR line of Li_6PS_5Br is composed of three distinct lines located at 93.9 ppm, 92.7 ppm and 91.1 ppm, respectively, indicating the instant positions. The shape of Li_6PS_5Br NMR chemical shift is narrower than those of Li_6PS_5Cl , but broader than those of Li_6PS_5I , indicating an intermediate anion disorder in the structure. The anion disorders (S/Cl, S/Br and S/I) in the structure of Li_6PS_5X is expected to have a significant impact on both the Li ion diffusion and ionic conductivity in Li_6PS_5X [67,68].

To investigate the ionic dynamics in a local diffusion length scale of Li_6PS_5X NMR motional line narrowing has been applied to roughly extract the Li^+ diffusion information. The inter-cage jumps in lithium argyrodite are expected to result in the averaging of homonuclear (Li-Li) dipole-dipole interactions. If the full averaging of the NMR line width is reached at a certain temperature, the corresponding inter-cage exchange rate in lithium argyrodite reaches high values on the order of kHz scale [66]. As shown in Fig. 4f, the 7Li NMR line width for both Li_6PS_5Br and Li_6PS_5Cl continuously decreases with increasing temperature, suggesting typical motional narrowing curves, while the change of 7Li NMR line width for Li_6PS_5I occurs in two steps. The extreme regime is reached at 250 K for both Li_6PS_5Cl and Li_6PS_5Br ($\nu_{\infty} \approx 300$ Hz), while the corresponding line of Li_6PS_5I is still broad with a width of $\nu = 2.2$ kHz, and finally reaches ν_{∞} at 350 K. The full averaging of the line width for Li_6PS_5I is shifted to an even higher temperature. This latter step corresponds to the inter-cage lithium ion jumps with a larger activation barrier, suggesting a much slower lithium-ion diffusion process occurs in the Li_6PS_5I structure compared to that of Li_6PS_5Cl . The inflexion points of the motional narrowing curves for Li_6PS_5Cl and Li_6PS_5Br are located at 128 and 86 K, respectively. The activation energy corresponding to long-range ion dynamics in the material can be deduced from the motional narrowing curves. The activation energies obtained by the Arrhenius fit are 0.06 eV for Li_6PS_5Br , 0.11 eV for Li_6PS_5Cl and 0.23 eV for Li_6PS_5I . The activation energy can be also obtained from the Hendrickson and Bray fit as 0.09 eV for Li_6PS_5Br , 0.18 eV for Li_6PS_5Cl and 0.38 eV for Li_6PS_5I , but these values are higher than those calculated from Arrhenius fit.

In addition to the line shape analysis, another powerful method to

probe ion dynamics in solid electrolytes on short time scales is NMR relaxometry. Both 7Li and ^{31}P spin-lattice relaxation (SLR) were applied to probe ion dynamics in Li_6PS_5X as shown in Fig. 4(g-i). The lithium ion jumps frequency and the corresponding activation energy can be deduced from the temperature dependence of the SLR rate. When $T_{1\rho}^{-1}$ reaches a maximum as a function of temperature, the hopping frequency is on the order of the Larmor frequency or locking frequency. As shown in Fig. 4(g-i), the 7Li NMR SLR rate peaks of Li_6PS_5X appear at 329 K for Li_6PS_5I , 286 K for Li_6PS_5Br and 316 K for Li_6PS_5Cl , respectively. The corresponding activation energies deduced from the low-temperature flank were 0.10 eV for Li_6PS_5Br , 0.17 eV for Li_6PS_5Cl and 0.18 eV for Li_6PS_5I , respectively. Meanwhile, the ^{31}P SLR NMR analysis offered Supporting Information. The ^{31}P SLR NMR peak of Li_6PS_5X was a result of fast PS_4^3- rotational dynamics on the high-temperature flank in lithium argyrodites. The maximum temperature of the ^{31}P SLR NMR peak agreed well with that of the 7Li SLR NMR peaks. It seems that the ^{31}P spins indirectly sense the rapid lithium exchange process in their direct neighborhood at high temperatures [65].

The activation energies obtained from NMR line shape analysis and NMR relaxometry show a similar trend that the values decrease in order for Li_6PS_5I , Li_6PS_5Cl and Li_6PS_5Br (i.e. $E_a, Li_6PS_5I > E_a, Li_6PS_5Cl > E_a, Li_6PS_5Br$), indicating the increase in anion polarizability ($I > Br > Cl$). The anion polarizability in Li_6PS_5X leads to both anion disorder and low hopping barriers. In order to unravel the mechanism for the effects of polarizability of anion sublattice on the Li^+ transport in Li_6PS_5X , fractional occupancy of the halogen anions (Cl, Br, and I) was designed to alter the anion framework [69]. Changing from Cl to Br or I leads to a clear change in the volume of lattice and site disorder. With an increasing unit cell volume, the intra-cage and inter-cage jumps distances increase, while the 48–48 h double jump distance decreases. However, unlike site disorders observed between S^{2-} and Cl^-/Br^- anions in Li_6PS_5Cl and Li_6PS_5Br , no disorder was observed for Li_6PS_5I due to the big difference of ionic radii of S^{2-} (170 pm) and I (206 pm). Therefore, the activation energy barrier for the Li^+ jumps increase in Li_6PS_5I , which explains its poor ionic conductivity.

Moreover, the halogen components have a striking influence on the Li^+ transport of Li_6PS_5X in terms of different lattice softness. Softer bonds not only lower the activation energy barrier, but also decrease the pre-factor of the moving ions [69]. By tailoring the lattice softness of lithium argyrodites, $Li_6PS_5Cl_{0.5}Br_{0.5}$ with the optimum lattice softness showed the much higher lithium ion conductivity in Li_6PS_5X .

Precise disorder of the halogen ions (Cl^- and/or Br^-) in the lithium argyrodite structure tunes the Li^+ conductivity. By molecular dynamics (MD) simulations, Klerk et al. found that the limiting jump rate for Li^+ conductivity in Li_6PS_5Cl was the doublet or inter-cage jumps which dependent on the Cl ordering over 4a and 4c sites [70]. Additionally, MD simulation results predicted that the highest Li^+ conductivity can be obtained when 3/4 of the 4c sites are occupied by Cl^- ions. Empirically, Rao et al. successfully tailored the disorder of Cl in Li_6PS_5Cl by annealing and confirmed disorder phenomena by in-situ neutron diffraction [42]. Due to the small difference of scattering factor for S, Cl and Br, neutron diffraction is a useful tool to distinguish the disorder between S^{2-} and Cl^-/Br^- in Li_6PS_5Cl and Li_6PS_5Br . As the correlation between the Cl disorder and Li^+ conductivity of lithium argyrodites has been verified experimentally with the trend predicted by MD simulations, it is promising to optimize the synthesis conditions to produce Li_6PS_5Cl a 1:3 Cl distribution over the 4a and 4c sites, which can possibly enhance the Li^+ conductivity [70]. Recently, Yu et al. [48] have optimized the annealing temperatures for Li_6PS_5Br using the direct solid-state sintering route and obtained pure Li_6PS_5Br with a Li^+ conductivity of 2.58 mS/cm at room temperature, which is approximately 2.5 times higher than the common Li_6PS_5Br (2.58 mS/cm vs. 1.0 mS/cm). With the help of powder neutron diffraction, they found that the Br ordering over the 4a and 4c sites ratio was close to 3 for this optimal Li_6PS_5Br , which is in good agreement with the theoretical prediction.

Although Li_6PS_5I has the same cubic argyrodite structure as Li_6PS_5Cl

and $\text{Li}_6\text{PS}_5\text{Br}$, $\text{Li}_6\text{PS}_5\text{I}$ exhibits a much lower Li^+ conductivity by several orders of magnitude (10^{-6} vs. 10^{-3} S/cm) compared to the other two analogs. Actually, NMR results showed that $\text{Li}_6\text{PS}_5\text{I}$ also possesses fast lithium-ion dynamics as $\text{Li}_6\text{PS}_5\text{Cl}$ and $\text{Li}_6\text{PS}_5\text{Br}$ on a local to medium-range length scale (double jumps and intra-cage jumps), but the long-range lithium-ion transport (inter-cage jumps) is switched off due to the ordered anion sublattice and the larger lattice constant [66]. Recently, the rapid lithium ion dynamics in $\text{Li}_6\text{PS}_5\text{X}$ is found be affected

by the rotational jumps of the PS_4^{3-} units based on the ^{31}P MAS NMR [65]. Specifically, the rotational jumps of PS_4^{3-} units in $\text{Li}_6\text{PS}_5\text{I}$ are decoupled due to its soft lattice, while the much slower rotational dynamics of PS_4^{3-} units in $\text{Li}_6\text{PS}_5\text{Cl}$ influences the inter-cage jumps in the structure. However, it seems that an optimal balance between lattice properties, site disorder and fast rotational jumps is established for $\text{Li}_6\text{PS}_5\text{Br}$, leading to facile translational lithium-ion displacements. From $\text{Li}_6\text{PS}_5\text{I}$ to $\text{Li}_6\text{PS}_5\text{Br}$ and further to $\text{Li}_6\text{PS}_5\text{Cl}$, the anion substitution

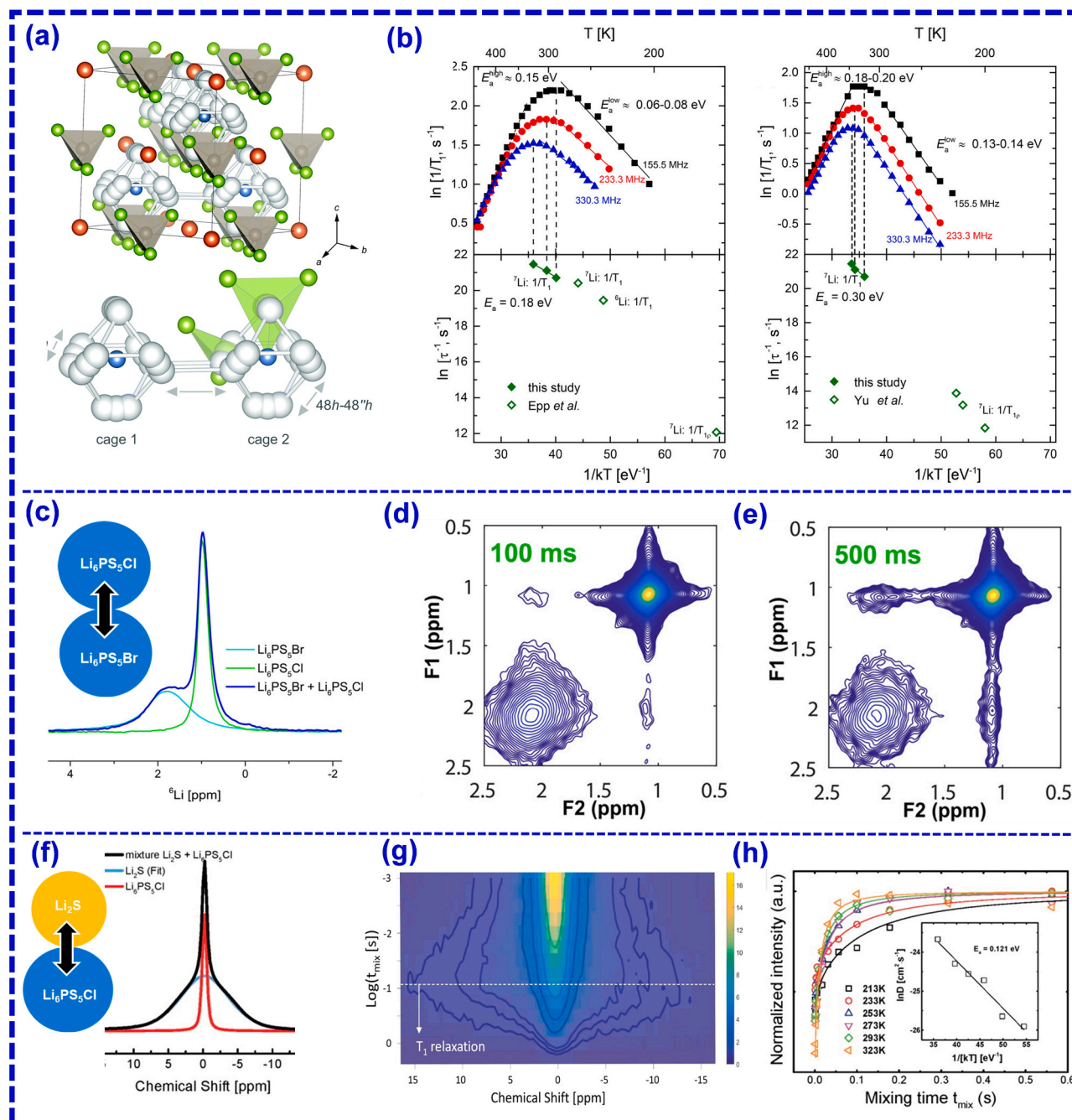


Fig. 5. Probing lithium ion dynamics in lithium argyrodite electrolytes from bulk to the interface. **(a)** Common crystal structure of $\text{Li}_6\text{PS}_5\text{X}$ ($\text{X} = \text{Cl}$ and Br) and three different types of lithium jumps in the structure [66]. **(b)** ^7Li spin-lattice relaxation rates of $\text{Li}_6\text{PS}_5\text{Br}$ (left) and $\text{Li}_6\text{PS}_5\text{Cl}$ (right) plotted as a function of the recording temperature measured at different field strengths (9.4, 14.1 and 20 T). **(c)** The ^6Li MAS NMR spectra of the nanosized $\text{Li}_6\text{PS}_5\text{Br}$, $\text{Li}_6\text{PS}_5\text{Cl}$ and a mixture of $\text{Li}_6\text{PS}_5\text{Br}$ - $\text{Li}_6\text{PS}_5\text{Cl}$ measured at a spinning speed of 10 kHz. The experiment was performed at 25 °C. **(d)** ^6Li - ^6Li exchange NMR spectra of the $\text{Li}_6\text{PS}_5\text{Br}$ - $\text{Li}_6\text{PS}_5\text{Cl}$ mixture were measured at 25 °C with mixing time of 100 ms **(d)** and 500 ms **(e)** at a spinning speed of 10 kHz. Cross-peaks are observable in those two peaks on the diagonal [71]. **(f)** The static ^7Li NMR spectrum of the Li_2S - $\text{Li}_6\text{PS}_5\text{Cl}$ mixture. **(g)** $1\text{D } ^7\text{Li}$ - ^7Li exchange NMR experiment probing lithium ion transport from the $\text{Li}_6\text{PS}_5\text{Cl}$ electrolyte to the Li_2S cathode at room temperature. **(h)** Normalized intensity of the static ^7Li NMR spectrum of Li_2S , T_1 corrected, as a function of the mixing time at different temperatures. The inset shows lithium-ion diffusion parameter changes as a function of the recording temperature [45].

contracts the lattice due to the decreasing ionic radii from I⁻ to Cl⁻. The NMR results have confirmed that the anion substitution affects the lattice parameters, the lattice softness and the lithium environment in the structure of Li₆PS₅X.

3.2. Probing lithium ion diffusion in lithium argyrodites from bulk to interface

3.2.1. Probing lithium-ion diffusion from the long-length to the short-length scale in lithium argyrodites

A typical characterization method to obtain the ionic conductivity of lithium argyrodite electrolytes is through the temperature-dependent AC impedance spectroscopy. The lithium-ion conductivity can be estimated based on the equation:

$$R = \rho l/S$$

where R is the resistance obtained from the impedance spectroscopy, l is the diffusion length (usually the thickness of the solid electrolyte pellet), S represents the surface area of the solid electrolyte pellet in contact with electrode and ρ is the resistivity. The Li⁺ conductivity at different temperatures can be calculated based on the impedance measurements recorded at corresponding temperatures.

Lithium argyrodite is an inorganic ion conductor which obeys the Arrhenius behavior. The activation energy for Li⁺ conduction can be calculated from the temperature-dependent ionic conductivity plots. However, it is not easy to distinguish the bulk ionic conductivity from the grain boundary ionic conductivity due to the influence of porosity, grain boundaries and contact with the blocking electrodes [45]. Moreover, the ionic conductivity and activation energy obtained from the impedance spectroscopy are average results of multiple lithium jump behaviors in parallel in lithium argyrodites as shown in Fig. 5a. To unravel the three different kinds of lithium jumps, solid-state NMR is a powerful tool [45–47,65,66,72]. Variable temperature ⁷Li line width of NMR resonances can give some insight into the lithium dynamics in Li₆PS₅Cl and Li₆PS₅Br. When the temperature is extremely high enough, the ⁷Li-⁷Li dipolar interactions are averaged out, so the lithium jump rate τ^{-1} of lithium argyrodite is much smaller than the spectral width of the dipolar broadened Gaussian NMR central line. The lithium jumping processes become faster as a function of the increasing temperature, and the rate of which is comparable to the NMR spectra width. The jump rate at the onset temperature of the motional narrowing curve and the corresponding activation energy can be deduced. The Li₆PS₅Br electrolyte exhibited an extremely low onset temperature of 87 K with a jump rate in the order of 10^{-3} s^{-1} , suggesting an ultrafast Li⁺ diffusion process in the material [72]. Similar characterization method and conclusions have also been reported in our previous work [45,47]. However, due to the temperature limitations of NMR instrument, the onset temperature sometimes cannot be reached.

To quantitatively quantify the lithium jump rate, the ⁶Li and ⁷Li SLR rates in the laboratory and the rotating frame can be used to specify the lithium jump rate in the lithium argyrodite electrolytes [45–48,65,66]. In both frames, the lithium jump rate ($R_{1(\rho)}$) initially increased with increasing temperature in the low-temperature flank, then reached a maximum at a special T_{max} , and decreased as a function of temperature in the high-temperature flank. At T_{max} , the lithium hopping frequency (τ^{-1}) in Li₆PS₅Cl and Li₆PS₅Br is in the order of magnitude as the Larmor frequency (ω_0) or the locking frequency (ω_1), following the expressions of $\omega_0 \tau_c \approx 1$ and $\omega_1 \tau_1 \approx 0.5$, respectively. The accurate Li⁺ jumping rate and the corresponding activation energy at T_{max} can be calculated correspondingly. Due to the fact that Larmor frequency and the locking frequency are significantly different (10^8 vs. 10^4 Hz), the short-range and long-range Li⁺ motions occurring at different time scales can be probed by SLR NMR. The maximum relaxation rates (R_1) of Li₆PS₅Cl and Li₆PS₅Br were reached at 345 and 383 K, respectively, and were estimated to be approximately $9.8 \times 10^8 \text{ s}^{-1}$ for both electrolytes. In the

rotating frame, the maximum $R_{1\rho}$ of Li₆PS₅Cl was determined as $1.38 \times 10^5 \text{ s}^{-1}$ at 200 K, $5.30 \times 10^5 \text{ s}^{-1}$ at 215 K and $1.06 \times 10^6 \text{ s}^{-1}$ at 220 K for the locking frequencies of 11, 42 and 84 kHz, respectively, compared to. While the lithium jump rates in the rotating frame at 20 kHz is $2.51 \times 10^5 \text{ s}^{-1}$ at 228 K for Li₆PS₅Br. The activation energy deduced from the low-temperature and high-temperature flanks of SLR NMR were 0.09 and 0.29 eV for Li₆PS₅Cl and 0.10 and 0.15 eV for Li₆PS₅Br, respectively. Comparison of these SLR NMR results and the MD simulations results identifies the correspondence between the SLR NMC temperature flanks and the Li⁺ diffusion behaviors. The low-temperature flank of the SLR NMR rates in the laboratory frame represents the short-range diffusion, which includes a combination of the back-and-forth and the intra-cage transitions. The high temperature flank represents the long-range inter-cage transitions, which are responsible for the macroscopic diffusion in Li₆PS₅Cl and Li₆PS₅Br.

Different methods including the high-temperature flank of SLR NMR and temperature-dependent AC impedance spectroscopy have been used to determine the activation energy for long-range Li⁺ conduction in the “bulk” lithium argyrodite. For Li₆PS₅Br, the activation energy was reported as 0.15 eV [47] and 0.20 eV [72] was reported based on the SLR NMR results, while the activation energy obtained from AC impedance reported by Deiseroth et al. [40] and Kraft et al. [69] for Li₆PS₅Br are 0.58 eV and 0.30 eV. The complexity of Li⁺ diffusion process in lithium argyrodites results in a broadened hopping-induced spectrum, leading to an underestimation of the activation energy for the bulk diffusion deduced from the SLR NMR measurement [71]. To probe the bulk Li⁺ diffusion in lithium argyrodites more accurately, SLR NMR as a function of temperature and resonance frequency was proposed by Ganapathy et al. [71] to study the Li⁺ dynamics in Li₆PS₅Cl and Li₆PS₅Br (synthesized by the direct solid-state reaction) at three different ⁷Li Larmor frequencies of 155.5, 233.3 and 330.3 MHz, as shown in Fig. 5b. The corresponding maximum rates R_1 of Li₆PS₅Cl were $8.30 \times 10^{11} \text{ s}^{-1}$ at 322 K, $1.30 \times 10^{12} \text{ s}^{-1}$ at 339 K and $8.00 \times 10^{11} \text{ s}^{-1}$ at 345 K, respectively. The maximum rates of Li₆PS₅Br were $6.40 \times 10^{11} \text{ s}^{-1}$ at 290 K, $7.80 \times 10^{11} \text{ s}^{-1}$ at 303 K and $3.10 \times 10^{11} \text{ s}^{-1}$ at 323 K, respectively. By fitting the maximum rates to different frequencies, the activation energy for Li⁺ conduction in Li₆PS₅Cl and Li₆PS₅Br were determined to be 0.29 and 0.18 eV, respectively. These values are higher than those deduced from the high-temperature flank of SLR rates but are more representative of the actual Li⁺ diffusion in bulk lithium argyrodites [71].

3.2.2. Probing lithium-ion diffusion across lithium argyrodite particles

It is difficult to decouple to the contributions of Li⁺ conduction in lithium argyrodites from bulk to grain boundary. Not to mention, probing Li⁺ transport between two lithium argyrodite single particles (Li₆PS₅Cl-Li₆PS₅Cl, Li₆PS₅Br-Li₆PS₅Br) is very challenging. Dawson et al. [73] emphasized the often underestimation of activation energy due to the complex contributions of Li⁺ conduction across grain boundaries. AC impedance spectroscopy is not an ideal method to probe Li⁺ motions between lithium argyrodites single particles. Exchange NMR is a powerful tool to probe lithium exchange between two lithium sites in the same structure or between two kinds of lithium-containing materials [45,74]. For example, Li₆PS₅Cl and Li₆PS₅Br have different chemical shifts (Fig. 5c) and different spin-lattice relaxation time, so the Li⁺ transport across the Li₆PS₅Cl-Li₆PS₅Br interface can be probed by 2D ⁶Li-⁶Li exchange NMR. However, exchange NMR cannot distinguish Li⁺ motions between two lithium argyrodite particles of the same kind (e.g. Li₆PS₅Cl-Li₆PS₅Cl or Li₆PS₅Br-Li₆PS₅Br interface), because there is no difference in chemical shift, NMR resonance line shape, or spin-lattice relaxation time. Nevertheless, Li₆PS₅Cl and Li₆PS₅Br are similar in structure and ionic conductivity, so the study of the Li₆PS₅Cl-Li₆PS₅Br interface is an ingenious design to obtain hints for understanding the Li⁺ transport at the Li₆PS₅Cl-Li₆PS₅Cl and Li₆PS₅Br-Li₆PS₅Br interfaces. The 2D ⁶Li-⁶Li exchange NMR analyses of Li₆PS₅Cl-Li₆PS₅Br mixtures were performed at various temperatures and mixing times. The spectra of mixing time of 100 ms and 500 ms are depicted in Fig. 5d and Fig. 5e,

respectively. The clear cross-peak intensities indicated lithium-ion exchange between the $\text{Li}_6\text{PS}_5\text{Cl}$ and $\text{Li}_6\text{PS}_5\text{Br}$ phases. The evolution of the normalized cross-peak intensity as a function of the mixing time measured at various temperatures (25, 50, 75 and 100 °C) can be used to extract the Li^+ diffusion parameters across the interface of $\text{Li}_6\text{PS}_5\text{Cl}$ - $\text{Li}_6\text{PS}_5\text{Br}$. The Li^+ diffusion rate was quantified by fitting the evolution of the cross-peak intensity as a function of the mixing time to a diffusion model derived from the Fick's law. The Li^+ diffusion coefficients (D) across the $\text{Li}_6\text{PS}_5\text{Cl}$ - $\text{Li}_6\text{PS}_5\text{Br}$ interface at various temperatures were fitted. The activation energy for Li^+ transport at the interface of $\text{Li}_6\text{PS}_5\text{Cl}$ - $\text{Li}_6\text{PS}_5\text{Br}$ was determined as 0.27 eV, which is approximately the energy barrier of NMR relaxometry. Therefore, the Li^+ diffusion across the grain boundaries is not the rate-limiting step of lithium argyrodite electrolytes.

3.2.3. Probing lithium-ion transport across the electrode-argyrodites interface

Understanding of the Li^+ transport between electrode and lithium argyrodite electrolytes is hindered by the limited techniques for precise probing at the interface. Our previous work attempted to track Li^+ transport at the interface of Li_2S cathode and $\text{Li}_6\text{PS}_5\text{Cl}$ electrolyte by ^7Li exchange NMR [45]. The different line widths of Li_2S and $\text{Li}_6\text{PS}_5\text{Cl}$ (Fig. 5f) can be used to identify the lithium exchange between the two materials. The $\text{Li}_6\text{PS}_5\text{Cl}$ electrolyte showed a narrower ^7Li NMR resonance due to the fast Li^+ mobility, while the Li_2S cathode with slower Li^+ mobility exhibited a much broader ^7Li NMR resonance. After filtering out the Li_2S resonance by an echo experiment, the transfer of magnetization was realized by the diffusion of Li^+ ions from the $\text{Li}_6\text{PS}_5\text{Cl}$ electrolyte to the Li_2S cathode. The results monitored as a function of the mixing time (t_{mix}) are shown in Fig. 5g. The transfer of magnetization from $\text{Li}_6\text{PS}_5\text{Cl}$ to Li_2S caused a broad resonance, indicating Li^+ ions from Li_2S (Fig. 5h). The emerging Li_2S signal due to the magnetization transfer carried by the Li^+ ions can be fitted with a diffusion model to quantify the lithium-ion exchange between $\text{Li}_6\text{PS}_5\text{Cl}$ electrolyte and Li_2S cathode. The self-diffusion coefficient of Li^+ ions transfer at the $\text{Li}_6\text{PS}_5\text{Cl}$ - Li_2S interface at different temperatures and the corresponding activation energy can be estimated.

3.3. Structural stability and hydrolysis resistance of lithium argyrodites

Structural stability and hydrolysis resistance are two critical properties of lithium argyrodites to be applied as high-performance electrolytes for solid-state batteries. Structural stability of lithium argyrodites determines the difficulty for synthesis and stability upon electrochemical cycling. Hydrolysis resistance is highly relevant to the storage method of the electrolytes and handling environment for assembling solid-state batteries [75].

Temperature-dependent anion disorders were observed in $\text{Li}_{7-x}\text{PS}_{6-x}\text{X}_x$ ($X = \text{Cl}, \text{Br}$) and its analogues by neutron diffractions [42, 46, 48, 70]. This "structural instability" is a partial inversion between the occupancies of the nominal S^{2-} and X^- ($X = \text{Cl}, \text{Br}$) sites in the structure. Based on the simulation, the occurrence of anion disorders is not only a kinetic effect, but also enthalpy driven [75]. Lithium argyrodites rapidly degrades upon exposure to air and moisture, so atmosphere control is usually required throughout the entire material synthesis and battery fabrication processes. Unraveling the hydrolysis mechanism of lithium argyrodites could help to better design strategies for stability improvement. Ultimately, air-stable lithium argyrodite electrolytes shall significantly reduce the production costs and improve the long-term reliability of lithium argyrodite-based solid-state batteries. The typical hydrolysis reactions of lithium argyrodites, $\text{Li}_{12-x-m}\text{M}^{m+}\text{S}_{6-x}\text{X}_x$ ($M = \text{P}, \text{As}, \text{Si}, \text{Ge}, \text{Sn}, X = \text{Cl}, \text{Br}$), are highly related to the cation M^{m+} . Taking $\text{Li}_{7-x}\text{PS}_{6-x}\text{X}_x$ as an example, the hydrolysis reaction occurs with an equation as follows:



Ab initio simulations have shown different sensitivity of lithium argyrodites to moisture. While P and Si based lithium argyrodites are highly sensitive to moisture, Ge, Sn and As based lithium argyrodites are less vulnerable to hydrolysis [75]. In addition, the hydrolysis resistance is also influenced by the halogen components in the lithium argyrodite structure.

Substitution of the chalcogens (Y^{2-}) and halogens (X^-) in $\text{Li}_{7-x}(\text{PY}_4)\text{Y}_{2-x}\text{X}_x$ is a possible strategy to improve the structural and chemical stabilities. [75] Based on the simulations, the chemical and electrochemical stabilities of lithium argyrodites increase in the order of $\text{Te} \ll \text{Se} < \text{S} < \text{O}$ for the chalcogen component. The O-based argyrodites show the highest hydrolysis resistance, while Se-based argyrodites and S-based argyrodites are easily hydrolyzed with different hydrolysis products. Kong et al. [76] have successfully synthesized $\text{Li}_6\text{PO}_5\text{Cl}$, but the Li^+ conductivity is low (10^{-9} S/cm at room temperature). The O-based argyrodites also showed a higher activation energy than S- or Se-based argyrodites (0.66 eV vs. 0.33 eV). Recently, Zhang et al. [52] introduced O into $\text{Li}_6\text{PS}_5\text{Br}$ to partially substitute the S elements, delivering excellent Li dendrite suppressing capability for Li metal batteries, good electrochemical and chemical stability against electrodes (both Li metal anode and high voltage oxide cathodes), and good air stability.

3.4. Strategies to improve ionic conductivity for lithium argyrodite electrolytes

3.4.1. Introduction of lithium vacancy

The disorder of S^{2-} and Cl^-/Br^- anions in $\text{Li}_6\text{PS}_5\text{Cl}$ and $\text{Li}_6\text{PS}_5\text{Br}$ can promote Li^+ mobility in the structure, while the larger Γ cannot be exchanged with S^{2-} resulting in an anion-ordered $\text{Li}_6\text{PS}_5\text{I}$ with poor Li^+ conductivity [42, 43, 77]. To unravel the underlying reason for the difference in ionic conductivity among the lithium argyrodites, MD simulation was used to reveal the Li^+ densities in Li_7PS_6 , $\text{Li}_6\text{PS}_5\text{Cl}$ and $\text{Li}_6\text{PS}_5\text{I}$ (Fig. 6a-c). Li_7PS_6 and $\text{Li}_6\text{PS}_5\text{Cl}$ showed similar Li^+ densities inside the cage. The regions with high Li^+ densities are connected to neighboring high-density regions inside a cage for both Li_7PS_6 and $\text{Li}_6\text{PS}_5\text{Cl}$, but the Li^+ ions appeared to be more localized in Li_7PS_6 than in $\text{Li}_6\text{PS}_5\text{Cl}$. The distributed Li^+ density suggests fast moving Li^+ ions inside the cage of $\text{Li}_6\text{PS}_5\text{Cl}$. In contrary, as shown in Fig. 6a, $\text{Li}_6\text{PS}_5\text{I}$ presented different Li^+ density. The high Li^+ density regions reflect a high lithium mobility between pairs of 48 h sites (the doublet jumps) and no lithium diffusion paths between the pairs of 48 h are visible, suggesting that only local lithium jumps exist in $\text{Li}_6\text{PS}_5\text{I}$.

As discussed in the above section, the disorder of Cl^-/Br^- and S^{2-} in argyrodite can be tailored by different annealing temperatures and durations to yield high Li^+ conductivity [42, 48]. Increasing the number of vacancy sites for Li^+ to a certain degree can enhance the Li^+ diffusivity [70]. For example, partial substitution of S^{2-} with Cl^- in Li_7PS_6 over the 4a and 4c sites can lead to Li^+ vacancies in $\text{Li}_6\text{PS}_5\text{Cl}$ with a much higher ionic conductivity [78]. Klerk et al. studied the correlation between Li^+ conductivity and the degree of Li^+ vacancies by MD simulations and comparison between $\text{Li}_5\text{PS}_4\text{X}_2$ ($X = \text{Cl}, \text{Br}, \text{I}$) [70]. The Li^+ conductivities of $\text{Li}_5\text{PS}_4\text{Cl}_2$ and $\text{Li}_5\text{PS}_4\text{Br}_2$ are found to be similar to those of $\text{Li}_6\text{PS}_5\text{Cl}$ and $\text{Li}_6\text{PS}_5\text{Br}$, respectively. However, Zhu et al. [79] reported that $\text{Li}_5\text{PS}_4\text{Cl}_2$ with an orthorhombic $C2mm$ space groups should have a room-temperature Li^+ conductivity of 1.85 mS/cm and an activation energy of 0.304 eV. $\text{Li}_5\text{PS}_4\text{Cl}_2$ has two symmetrically distinct Li sites with a 3D diffusion networks. The Li^+ probability density function (PDF) was calculated to unravel the atomistic diffusion mechanisms and pathways of $\text{Li}_5\text{PS}_4\text{Cl}_2$. In each Li1 plane in the b-c plane stacked along the a direction, $\text{Li}_5\text{PS}_4\text{Cl}_2$ shows extremely low energy barrier for lithium vacancy migration. Adeli et al. [39] recently confirmed the prediction and experimentally demonstrated enhanced Li^+ diffusivity and ionic conductivity in $\text{Li}_6\text{PS}_5\text{Cl}$ by further halide substitution. An optimal halide-rich composition, $\text{Li}_{5.5}\text{PS}_{4.5}\text{Cl}_{1.5}$, showed an ultrafast Li^+ conductivity of 9.4 mS/cm with a low activation energy of 0.29 eV,

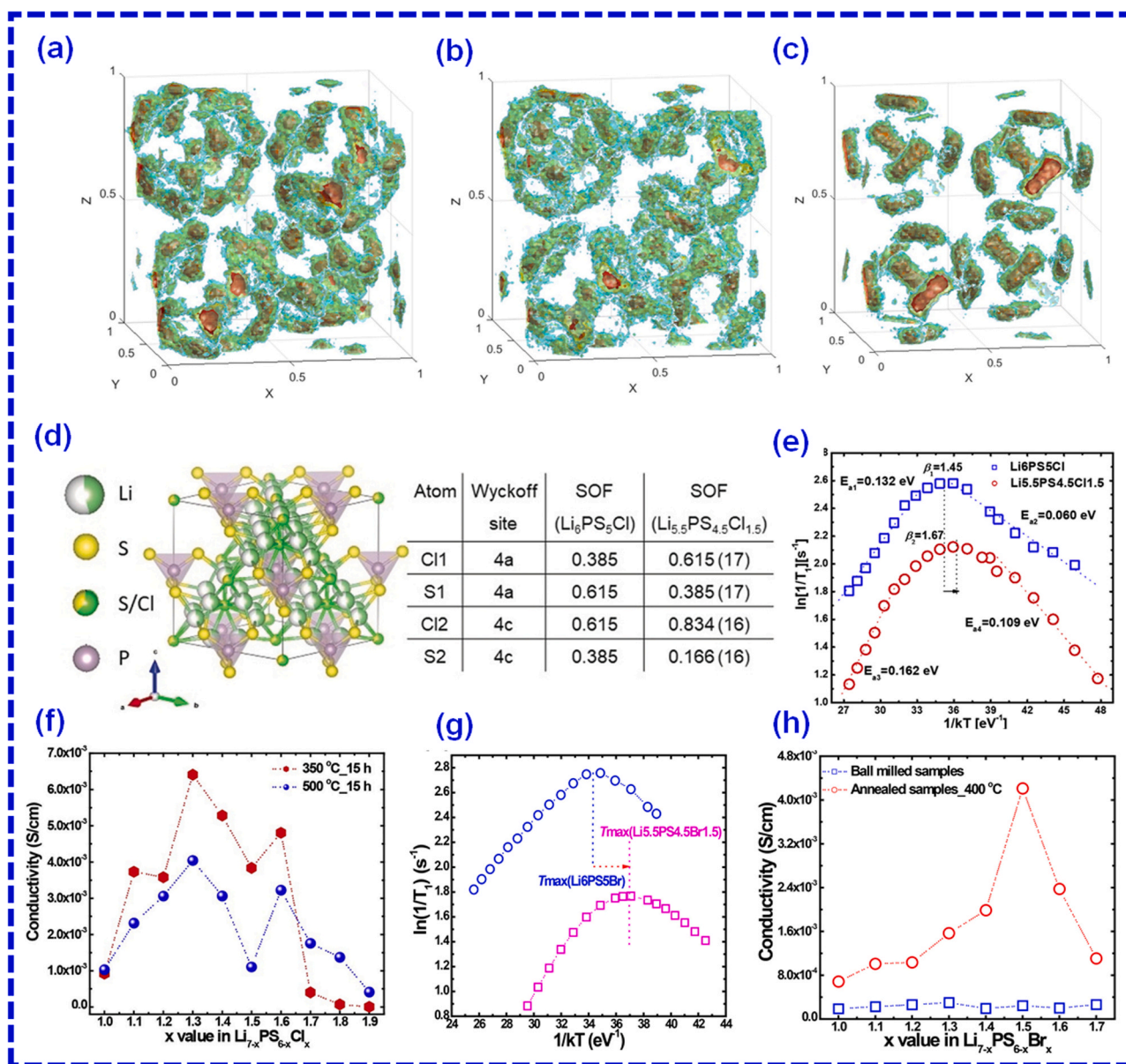


Fig. 6. Li-ion density in the lithium argyrodite unit cell during MD simulations at 450 K of (a) Li_7PS_6 , (b) $\text{Li}_6\text{PS}_5\text{Cl}$ and (c) $\text{Li}_6\text{PS}_5\text{I}$. Red, yellow, green and blue indicate decreasing Li-ion densities in order [70]. (d) Crystal structure of $\text{Li}_{5.5}\text{PS}_{4.5}\text{Cl}_{1.5}$ showing the PS_4^{3-} tetrahedra, the cage-like polyhedra formed by Li^+ ions, free $\text{S}^{2-}/\text{Cl}^-$ anions and comparison of occupancies (SOF) on the 4a and 4c sites between $\text{Li}_6\text{PS}_5\text{Cl}$ and $\text{Li}_{5.5}\text{PS}_{4.5}\text{Cl}_{1.5}$ [39]. (e) Temperature-dependent ^7Li SLR NMR rates for $\text{Li}_6\text{PS}_5\text{Cl}$ and $\text{Li}_{5.5}\text{PS}_{4.5}\text{Cl}_{1.5}$ electrolytes measured in the laboratory frame of the reference. The Larmor frequency is 155.248 MHz. (f) Room temperature Li^+ conductivity of $\text{Li}_{7-x}\text{PS}_{6-x}\text{Cl}_x$ ($x = 1.0, 1.1, 1.2, 1.3, 1.4, 1.5, 1.6, 1.7, 1.8$ and 1.9) annealed at two different temperatures for 15 h [49]. (g) Temperature-dependent ^7Li spin-lattice relaxation time (T_1) changes of the corresponding $\text{Li}_6\text{PS}_5\text{Br}$ and $\text{Li}_{5.5}\text{PS}_{4.5}\text{Br}_{1.5}$. (h) The Li^+ conductivity of $\text{Li}_{7-x}\text{PS}_{6-x}\text{Br}_x$ ($x = 1.0, 1.1, 1.2, 1.3, 1.4, 1.5, 1.6$ and 1.7) obtained from mechanical milling synthesis (550 rpm, 16 h) and heat treatment processes (400 °C/10 h) [80].

which is almost four-fold higher than that of the pristine $\text{Li}_6\text{PS}_5\text{Cl}$. In the framework of $\text{Li}_{5.5}\text{PS}_{4.5}\text{Cl}_{1.5}$, only the 4b site is occupied by Li, while S and Cl share the 4a and 4c sites with the additional Cl being distributed evenly over both sites (Fig. 6d). The increased Li^+ diffusivity and lowered activation barrier are associated with the increase of Cl and Li vacancy contents. Yu et al. [49,80] also demonstrated enhanced ionic conductivity of $\text{Li}_6\text{PS}_5\text{X}$ ($X = \text{Cl}, \text{Br}$) by the introduction of lithium vacancy.

Lithium jumps in $\text{Li}_6\text{PS}_5\text{Cl}$ and $\text{Li}_{5.5}\text{PS}_{4.5}\text{Cl}_{1.5}$ in the local diffusion length-scale were characterized by ^7Li SLR NMR (Fig. 6e). $\text{Li}_{5.5}\text{PS}_{4.5}\text{Cl}_{1.5}$ showed the same lithium jump frequency at a lower temperature when compared to $\text{Li}_6\text{PS}_5\text{Cl}$, indicating a faster local Li^+ jump rate in $\text{Li}_{5.5}\text{PS}_{4.5}\text{Cl}_{1.5}$ than in $\text{Li}_6\text{PS}_5\text{Cl}$, which is in good agreement with the simulation results [49]. Ab initio molecular dynamics (AIMD)

simulations proved that the improvement in ionic conductivity is due to the decreased energy barriers for Li^+ migration in local diffusion length scales. More recently, Adeli et al. [81] investigated the influence of aliovalent cation substitution and mechanical compression on lithium-ion conductivity and diffusivity in lithium argyrodite solid electrolyte and found that $\text{Li}_{5.35}\text{Ca}_{0.1}\text{PS}_{4.5}\text{Cl}_{1.55}$ exhibits a superionic room temperature conductivity of $10.2 \text{ mS}\cdot\text{cm}^{-1}$ in the cold-pressed state and an exceptional diffusivity of $1.21 \times 10^{-11} \text{ m}^2/\text{s}$.

The optimal composition for sufficient lithium vacancy and high ionic conductivity can be further tailored by controlling the halogen content in the argyrodite structure [49,80]. As shown in Fig. 6f, $\text{Li}_{5.7}\text{PS}_{4.7}\text{Cl}_{1.3}$ presented the highest ionic conductivity ($6.4 \text{ mS}/\text{cm}$) among the modified lithium argyrodites $\text{Li}_{7-x}\text{PS}_{6-x}\text{Cl}_x$ ($x = 1.1-1.9$). Meanwhile, the effects of annealing temperatures were investigated. A

lower annealing temperature of 350 °C was found suitable for low doping amount of Cl ($x = 1.0$ – 1.6) to get pure phase with high lithium-ion conductivity, while a much higher annealing temperature of 500 °C was required for high doping contents of Cl ($x = 1.7$, 1.8 and 1.9). However, over Cl doping turned out to be a drawback to ionic conductivity. Recently, Feng et al. [82] reported that they have successfully prepared $\text{Li}_{5.3}\text{PS}_{4.3}\text{Cl}_{1.7}$ electrolyte with ionic conductivity of 17 mS/cm at room temperature, and found that the increased conductivity is associated with the anion disorder-induced ion transport.

Similarly, by tuning the Br content in $\text{Li}_{7-x}\text{PS}_{6-x}\text{Br}_x$ ($x = 1.0$ – 1.7), $\text{Li}_{5.5}\text{PS}_{4.5}\text{Br}_{1.5}$ showed a much higher Li^+ conductivity (4.17 mS/cm) than that of the pristine $\text{Li}_6\text{PS}_5\text{Br}$ (0.8 mS/cm) [80]. The ^7Li SLR NMR analysis gave consistent results (Fig. 6g). Different annealed $\text{Li}_{6-x}\text{PS}_{5-x}\text{Br}_x$ ($x = 1.0$ – 1.7) electrolytes actually varied a lot in ionic

conductivities (Fig. 6h), which is associated with the $\text{Br}^-/\text{S}^{2-}$ disorder in the structure. Moreover, experimental results showed that the introduction of Br can not only increase the ionic conductivity but also improve compatibility with Li metal anode. Wang et al. [83] found that $\text{Li}_{5.3}\text{PS}_{4.3}\text{Br}_{1.7}$ shows the highest ionic conductivity (11 mS/cm) among $\text{Li}_{6-x}\text{PS}_{5-x}\text{Br}_{1+x}$ due to the increased Li^+ occupancy at 24 g sites.

3.4.2. Doping

The basic composition of lithium argyrodite is Li_7PS_6 , [40] existing in high- and low-temperature phases (LT- Li_7PS_6 and HT- Li_7PS_6 , respectively). The ionic conductivity of the two phases are extremely low, 1.6×10^{-6} S/cm for LT- Li_7PS_6 and 3.0×10^{-5} S/cm for HT- Li_7PS_6 , respectively [87]. Fig. 7a summarizes three categories of doping with different elemental substitutions in Li_7PS_6 , including Li, P and S sites. To

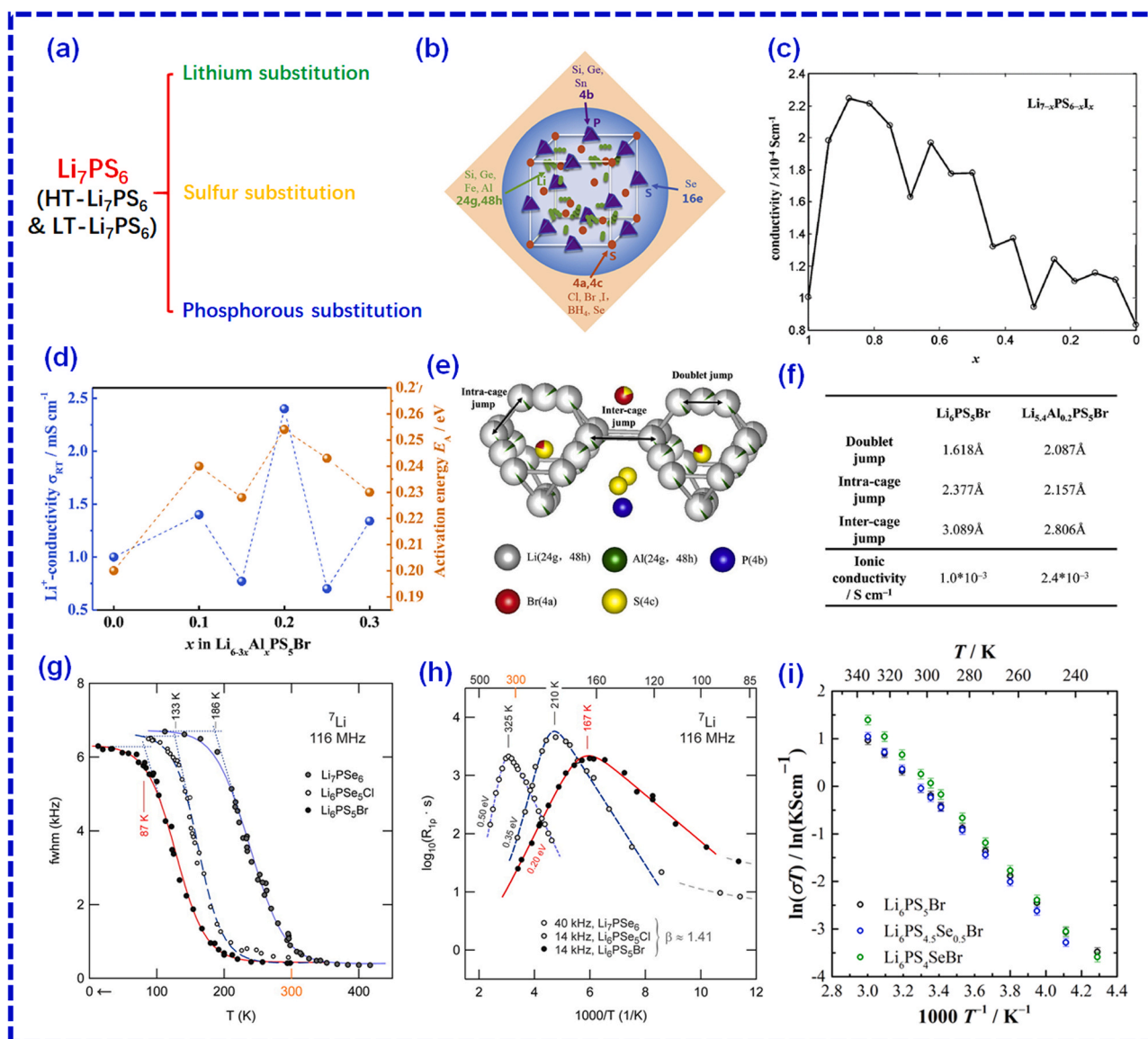


Fig. 7. (a) Elemental substitutions of different constituents in Li_7PS_6 for improving ionic conductivity. (b) Schematic diagram of elemental substitutions at various sites in the Li_7PS_6 argyrodite structure [84]. (c) Conductivity of $\text{Li}_{7-x}\text{PS}_{6-x}\text{I}_x$ single-crystal models ($4 \times 4 \times 4$ super-cells) calculated from 15 ns molecular dynamics simulation at 1 atm and 500 K [85]. (d) Room-temperature ionic conductivity and activation energy of the $\text{Li}_{6-3x}\text{Al}_x\text{PS}_5\text{Br}$ ($x = 0, 0.1, 0.15, 0.2, 0.25, 0.3$) electrolytes. (e) Crystal structure of $\text{Li}_{5.4}\text{Al}_{0.2}\text{PS}_5\text{Br}$ shows the jump distance between different lithium jumps (the 48h-48h doublet jump, the intra-cage jumps and the inter-cage jumps) and (f) the corresponding parameters in $\text{Li}_{5.4}\text{Al}_{0.2}\text{PS}_5\text{Br}$ [84]. (g) Temperature dependence of the ^7Li NMR line widths (full width at half-maximum) of Li_7PSe_6 , $\text{Li}_6\text{PSe}_5\text{Cl}$ and $\text{Li}_6\text{PS}_5\text{Br}$. (h) The ^7Li spin-lattice relaxation NMR rates of Li_7PSe_6 , $\text{Li}_6\text{PSe}_5\text{Cl}$ and $\text{Li}_6\text{PS}_5\text{Br}$ recorded at specific locking frequencies. The farther the diffusion-induced NMR relaxation peak is shifted toward lower T , the faster Li exchange and the smaller the activation energy turns out. Lithium diffusion drastically increases in the following order: $\text{Li}_7\text{PSe}_6 < \text{Li}_6\text{PSe}_5\text{Cl} < \text{Li}_6\text{PS}_5\text{Br}$ [72]. (i) The Arrhenius plots of the conductivity values for $\text{Li}_6\text{PS}_{5-x}\text{Se}_x\text{Br}$ ($x = 0, 0.5, 1.0$) obtained from temperature-dependent impedance spectroscopy [86].

increase Li^+ conductivity, Deiseroth et al. [40] proposed a new composition of $\text{Li}_6\text{PS}_5\text{X}$ ($\text{X} = \text{Cl}, \text{Br}$) with ultrafast Li^+ diffusion by partially substituting S with halogen elements. The $\text{Li}_6\text{PS}_5\text{X}$ electrolytes obtained by mechanochemical and annealing synthesis route usually deliver a Li^+ conductivity between 1.0 and 2.0×10^{-3} S/cm at room temperature [41–44,47,50], but $\text{Li}_6\text{PS}_5\text{I}$ shows a poor ionic conductivity in the order of 10^{-6} S/cm [69,88,89]. More doping options at the Li, P and S sites in lithium argyrodites for the ionic conductivity enhancement are summarized in Fig. 7b. The Li positions at 24 g and 48 h sites can be substituted by high-valence dopants such as Fe^{2+} [90], Al^{3+} , Si^{4+} and Ge^{2+} [84].

In order to stabilize the HT- Li_7PS_6 structure and increase ionic conductivity, partial substitution of Li^+ ions in HT- Li_7PS_6 by Fe^{2+} ions led a new group of lithium argyrodite electrolytes with a formula of $\text{Li}_{7-2x}\text{Fe}_x\text{PS}_6$ [90]. The optimal composition, $\text{Li}_6\text{Fe}_{0.5}\text{PS}_6$, showed a high Li^+ conductivity of 1.4×10^{-4} S/cm, which is much higher than that of HT- Li_7PS_6 (vs. 10^{-5} S/cm). Recently, Zhang et al. [84] studied the effect of partial substitution of Li^+ with a small amount of Al^{3+} in $\text{Li}_6\text{PS}_5\text{Br}$. Different amounts of Al^{3+} were incorporated into the $\text{Li}_6\text{PS}_5\text{Br}$ structure to form $\text{Li}_{6-3x}\text{Al}_x\text{PS}_5\text{Br}$ ($x = 0, 0.1, 0.15, 0.20, 0.25, 0.3$). Their ionic conductivities and corresponding activation energies are shown in Fig. 7d. By tailoring the fraction of Al^{3+} , the maximum room-temperature ionic conductivity reached 2.4×10^{-3} S/cm by $\text{Li}_{5.4}\text{Al}_{0.2}\text{PS}_5\text{Br}$, which was much higher than the ionic conductivity of pristine $\text{Li}_6\text{PS}_5\text{Br}$ (0.9 mS/cm). The improved ionic conductivity was attributed to the shortened lithium diffusion distance of the inter-cage jumps as shown in Fig. 7e and 7f. Moreover, our ongoing work shows that Na^+ substitution of Li^+ in $\text{Li}_6\text{PS}_5\text{Br}$ can also enhance the Li^+ conductivity from 1.0×10^{-3} to 1.54×10^{-3} S/cm at room temperature. In summary, successful cation substitutions at the Li positions, no matter with high-valence cations or large alkaline ions, can lead to enhanced ionic conductivity for lithium argyrodite electrolytes.

Substitution of S^{2-} in HT- Li_7PS_6 by halogen ions (X , e.g. Br^- or Cl^-) yields a new family of lithium argyrodite electrolytes, in form of $\text{Li}_6\text{PS}_5\text{X}$ ($\text{X} = \text{Cl}, \text{Br}$), with much higher conductivity close to 10^{-2} S/cm at room temperature [40]. However, the highly ordered S^{2-} and Γ in the $\text{Li}_6\text{PS}_5\text{I}$ structure hinders Li^+ transport. The ionic conductivity of $\text{Li}_6\text{PS}_5\text{I}$ is lower by 3 orders of magnitude compared to that of $\text{Li}_6\text{PS}_5\text{Cl}$ and $\text{Li}_6\text{PS}_5\text{Br}$ [40,66]. Nevertheless, a high Li^+ conductivity can be achieved by $\text{Li}_{7-x}\text{PS}_{6-x}\text{I}_x$ with a series of interstitial sites. The interstitial sites are essential for forming a Li^+ conductive network across the $\text{Li}_{7-x}\text{PS}_{6-x}\text{I}_x$ structure. As shown in Fig. 7c, the conductivity of $\text{Li}_{7-x}\text{PS}_{6-x}\text{I}_x$ can be more than doubled depending on the Γ content in the S^{2-} sites based on simulations [85]. The highest Li^+ conductivities are reached by $\text{Li}_{7-x}\text{PS}_{6-x}\text{I}_x$ when $0.75 \leq x \leq 0.95$.

In addition to S based Li_7PS_6 , the Se based Li_7PSe_6 is another well-established lithium argyrodite electrolyte. Epp et al. [72] found that the Li^+ diffusivity increased in the order of Li_7PSe_6 , $\text{Li}_6\text{PSe}_5\text{Cl}$, $\text{Li}_6\text{PS}_5\text{Br}$ based on multiple NMR methods (Fig. 7g and 7h). The onset temperatures of motional narrowing were 186 K for Li_7PSe_6 , 133 K for $\text{Li}_6\text{PSe}_5\text{Cl}$ and 87 K for $\text{Li}_6\text{PS}_5\text{Br}$, respectively. Since the measurements were performed at the same frequency, the lithium jump rate τ^{-1} was expected to be in the order of 10^{-3} s^{-1} at the onset point of the motional narrowing curve. A lower onset temperature means a faster lithium jump rate. Therefore, $\text{Li}_6\text{PS}_5\text{Br}$ with a lowest onset temperature possesses the highest Li^+ conductivity among the three lithium argyrodite electrolytes. Meanwhile, the ^7Li SLR NMR rates of the three argyrodite electrolytes also verified the ultrafast Li^+ diffusion in these electrolytes. The asymmetric rate peak appeared at 325 K for Li_7PSe_6 , 210 K for $\text{Li}_6\text{PSe}_5\text{Cl}$ and 167 K for $\text{Li}_6\text{PS}_5\text{Br}$, respectively. A consistent conclusion regarding the fastest Li^+ conduction in $\text{Li}_6\text{PS}_5\text{Br}$ among the three electrolytes was reached.

The partial substitution of S with large halogen ions in Li_7PS_6 and its analogues induces structural mismatch and strain. Due to the different polarizabilities of the substituting anions, the resulting Li^+ diffusivity of the differently doped lithium argyrodite electrolytes vary. Bernges et al.

[86] demonstrated that incorporation of the larger and more polarizable Se^{2-} (compared to S^{2-}) into the $\text{Li}_6\text{PS}_5\text{Br}$ lattice enhanced the ionic conductivity of lithium argyrodites. Among the $\text{Li}_6\text{PS}_{5-x}\text{Se}_x\text{Br}$ ($0 \leq x \leq 1$) electrolytes, $\text{Li}_6\text{PS}_4\text{SeBr}$ showed the highest room-temperature ionic conductivity of 3.9 S/cm (Fig. 7i). The lattice parameters of $\text{Li}_6\text{PS}_{5-x}\text{Se}_x\text{Br}$ and the occupancy of the 16e site by Se^{2-} increase as a function of the Se^{2-} substitution content. The drastic decrease in the $\text{Br}^-/\text{Ch}^{2-}$ ($\text{Ch} = \text{chalcogenide}$) site disorder leads to a rearrangement of Li^+ from the 24 g to the 48 h site and widens the Li^+ diffusion pathways. The broadening of the Li^+ diffusion pathways is beneficial to fast Li^+ transport.

In addition to doping at the Li and S positions based on the Li_7PS_6 argyrodite structure, elemental substitution of P is also viable. Density functional theory (DFT) calculations predicted the thermodynamically stable occurrence of $\text{Li}_{7+x}\text{M}_x\text{P}_{1-x}\text{S}_6$ ($\text{M} = \text{Si}, \text{Ge}$), which has also been confirmed by the experimental results. Si and Ge aliovalent substitutions of the P in the 4b site in Li_7PS_6 structure help to stabilize the desired cubic high-temperature phase and enhance ionic conductivity to above 10^{-3} S/cm (Fig. 8a). These electrolytes were predicted to have a wide electrochemical window and good Li metal compatibility [91]. With the presence of Ge or Si, the lithium argyrodites $\text{Li}_{7+x}\text{Ge}_x\text{P}_{1-x}\text{S}_6$ ($0 < x \leq 0.35$) and $\text{Li}_{7+x}\text{Si}_x\text{P}_{1-x}\text{S}_6$ ($0 < x \leq 0.40$) can maintain the favorable HT- Li_7PS_6 -like phase even at -50°C . Similarly, Minafra et al. [92] demonstrated increased ionic conductivities of the Si doped $\text{Li}_{6+x}\text{P}_{1-x}\text{Si}_x\text{S}_5\text{Br}$ ($0 \leq x \leq 0.50$) electrolytes compared to $\text{Li}_6\text{PS}_5\text{Br}$. As shown in Fig. 8b, the ionic conductivity can be increased by three folds, from 0.7 to 2.4 mS/cm, when $x = 0.35$ and 0.5 (i.e. $\text{Li}_{6.35}\text{P}_{0.65}\text{Si}_{0.35}\text{S}_5\text{Br}$ and $\text{Li}_{6.5}\text{P}_{0.5}\text{Si}_{0.5}\text{S}_5\text{Br}$). This enhancement can be attributed to the fact that the incorporation of the larger Si^{4+} not only increased the carrier concentration (i.e., Li^+ concentration), but also the size of unit cell. The occupancy of ionic carriers at the transition state for lithium-ion hopping was increased.

As discussed before, $\text{Li}_6\text{PS}_5\text{I}$ displays the lowest Li^+ conductivity among the halogen containing $\text{Li}_6\text{PS}_5\text{X}$ ($\text{X} = \text{Cl}, \text{Br}, \text{I}$) argyrodite electrolytes due to its structurally ordered anions. Interrupting the anion structural order by substitutions is a possible way to enhance the conductivity. The aliovalent substitution of P^{5+} with Ge^{4+} can tune the lattice parameters, the Li occupancies and the Γ/S^{2-} site disorder in $\text{Li}_{6+x}\text{P}_{1-x}\text{Ge}_x\text{S}_5\text{I}$ ($0 \leq x \leq 0.80$) (Fig. 8c). Anion site disorder was observed. It was found that the activation barrier for ionic motion dropped significantly as a function of the increasing Ge content. The $\text{Li}_{6.6}\text{P}_{0.4}\text{Ge}_{0.6}\text{S}_5\text{I}$ electrolyte demonstrated a Li^+ conductivity of 5.4 ± 0.8 mS/cm in a cold-pressed state and 18.4 ± 2.7 mS/cm upon sintering [88]. The structural changes and increased lattice volume of the $\text{Li}_{6+x}\text{P}_{1-x}\text{Ge}_x\text{S}_5\text{I}$ argyrodites facilitated inter-cage jumps in the Li^+ diffusion network. This study successfully demonstrated favorable structural modification and anion site disorder in lithium argyrodites by aliovalent substitution (Fig. 8d and 8e). High ionic conductivity can be tuned accordingly.

Recently, two series of elemental substitutions in form of $\text{Li}_{6+x}\text{P}_{1-x}\text{M}_x\text{S}_5\text{I}$ ($\text{M} = \text{Si}$ and Sn) have been proposed to improve the ionic conductivity of $\text{Li}_6\text{PS}_5\text{I}$ [93,94]. Successful Si or Sn doping can significantly enhance the Li^+ conductivities, from 10^{-3} mS/cm for the unsubstituted $\text{Li}_6\text{PS}_5\text{I}$ to 2.0 ± 0.3 mS/cm for $\text{Li}_{6.7}\text{P}_{0.3}\text{Si}_{0.7}\text{S}_5\text{I}$ and 0.1 ± 0.015 mS/cm for $\text{Li}_{6.3}\text{P}_{0.7}\text{Sn}_{0.3}\text{S}_5\text{I}$ [95]. Similar changes in the Li-sublattice occurred despite the significant difference in ionic size of the dopants, indicating that the lithium substructure is most likely influenced by the occurring $\text{Li}^+ - \text{Li}^+$ interaction in $\text{Li}_{6+x}\text{P}_{1-x}\text{M}_x\text{S}_5\text{I}$ ($\text{M} = \text{Si}$ and Sn). The sharp decrease in activation energy at the same $\text{M}^{4+}/\text{P}^{5+}$ composition for all $\text{Li}_{6+x}\text{P}_{1-x}\text{M}_x\text{S}_5\text{I}$ ($\text{M} = \text{Si}, \text{Ge}$ and Sn) indicates that the energy landscape of lithium argyrodites can be tailored by inducing local disorder via aliovalent substitution of $\text{M}^{4+}/\text{P}^{5+}$. Another example was reported by Zhao et al. [96]. Recently, partial substitution of P^{5+} by Sn^{4+} in $\text{Li}_6\text{PS}_5\text{I}$ yielded much higher ionic conductivity (0.35 mS/cm vs. 0.0028 mS/cm). The resulting electrolyte also showed excellent air stability and Li metal anode compatibility.

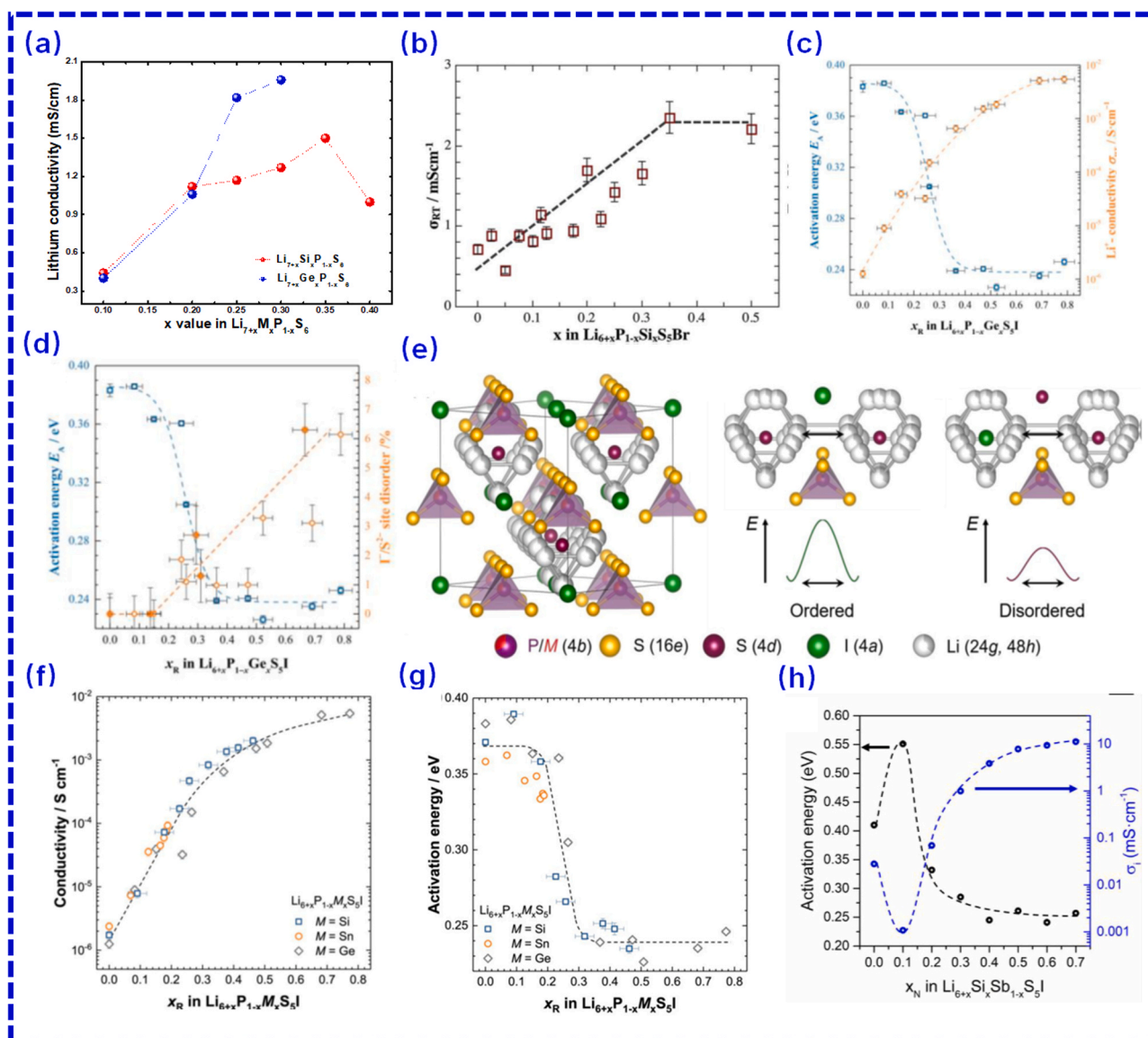


Fig. 8. The ionic conductivity of (a) $\text{Li}_{7+x}\text{P}_{1-x}\text{M}_x\text{S}_6$ ($M = \text{Si}, \text{Ge}$) and (b) $\text{Li}_{6+x}\text{P}_{1-x}\text{Si}_x\text{S}_5\text{Br}$ for all degrees of substitution in the solid solution [92]. (c) The activation energy and ionic conductivity of $\text{Li}_{6+x}\text{P}_{1-x}\text{Ge}_x\text{S}_5\text{I}$ as a function of the Ge content. (d) The refined S^{2-}/I disorder of $\text{Li}_{6+x}\text{P}_{1-x}\text{Ge}_x\text{S}_5\text{I}$ as a function of x_{R} . The activation barriers drop sharply at the onset composition for S^{2-}/I disorder, leading to a high ionic conductivity [88]. (e) Crystal structure of $\text{Li}_{6+x}\text{P}_{1-x}\text{M}_x\text{S}_5\text{I}$ ($M = \text{Si}, \text{Ge}$, or Sn). The I stacking forms a face-centered cubic lattice, with PS_4^{3-} units in the octahedral sites and free S^{2-} anions occupying 50% of the tetrahedral voids. The Li^+ forms pseudo-octahedral cages around the S^{2-} sites with two separate positions of 24 g and 48 h. The rate-determining step for lithium transport is the 48 h-48 h inter-cage jump. The right figure shows a proposed mechanism of the energy landscape flattening. (f) Ionic conductivity and (g) activation energy evolutions for the $\text{Li}_{6+x}\text{P}_{1-x}\text{M}_x\text{S}_5\text{I}$ ($M = \text{Si}, \text{Ge}$ and Sn) electrolytes as a function of the M content [95]. (h) The activation energy and ionic conductivities of the cold pressed $\text{Li}_{6+x}\text{Si}_x\text{Sb}_{1-x}\text{S}_5\text{I}$ as a function of the Si^{4+} content in the structure [97].

Furthermore, completely replacing P with Sb (Fig. 8(f–h)) leads to a new family of lithium argyrodites $\text{Li}_{6+x}\text{Sb}_{1-x}\text{M}_x\text{S}_5\text{I}$ ($M = \text{Si}, \text{Ge}$ and Sn). Zhou et al. [97] reported high room-temperature ionic conductivity of 14.8 mS/cm for cold-pressed pellets and up to 24 mS/cm for sintered pellets. In combination of theoretical and experimental results, they found that pushing Li^+ ions into the high energy sites of the lithium argyrodite structure can induce concerted Li^+ migration with a reduced migration energy barrier.

3.5. New halogen-free lithium argyrodite electrolytes

The halogen components in $\text{Li}_6\text{PS}_5\text{Cl}$ and $\text{Li}_6\text{PS}_5\text{Br}$ electrolytes can cause corrosion of Al current collectors at high voltages. The development of novel halogen-free lithium argyrodite electrolyte is of high interests. Schneider et al. [98] designed a series of halogen-free lithium

argyrodite fast conductors with good ionic conductivities up to 2–3.0 mS/cm. Based on $\text{Li}_7\text{P}_6\text{S}_6$, partial substitution of P by Si led to a general formula of $\text{Li}_{2x}\text{SiP}_2\text{S}_{x+7}$, such as $\text{Li}_{22}\text{SiP}_2\text{S}_{18}$. The demonstrated ionic conductivity was among the highest for silicon sulfide containing lithium argyrodite electrolytes.

Free of P and halogens, novel phosphorus- and halide-free superionic lithium argyrodites $\text{Li}_{4+x}\text{Al}_x\text{Si}_{1-x}\text{S}_4$ have been designed from a quasi-ternary $\text{Li}_2\text{S}-\text{Al}_2\text{S}_3-\text{SiS}_2$ system (Fig. 9a) [99]. A typical example is $\text{Li}_{6.15}\text{M}_{1.5}\text{S}_6$, where M generally represents any combination of Al and Si. The high-temperature phase of $\text{Li}_{6.15}\text{M}_{1.5}\text{S}_6$ (HT- $\text{Li}_{6.15}\text{M}_{1.5}\text{S}_6$) is constructed with a framework of orderly arranged $\text{M}(\text{S/O})_4$ units, with disordered Li/ M ions at the tetrahedral 48 h and 16e sites (Fig. 9b). This series of electrolytes showed a highest ionic conductivity of 0.254 mS/cm at room temperature as shown in Fig. 9c [100]. The Li^+ diffusion cage consists of six cation doublets, is formed by two

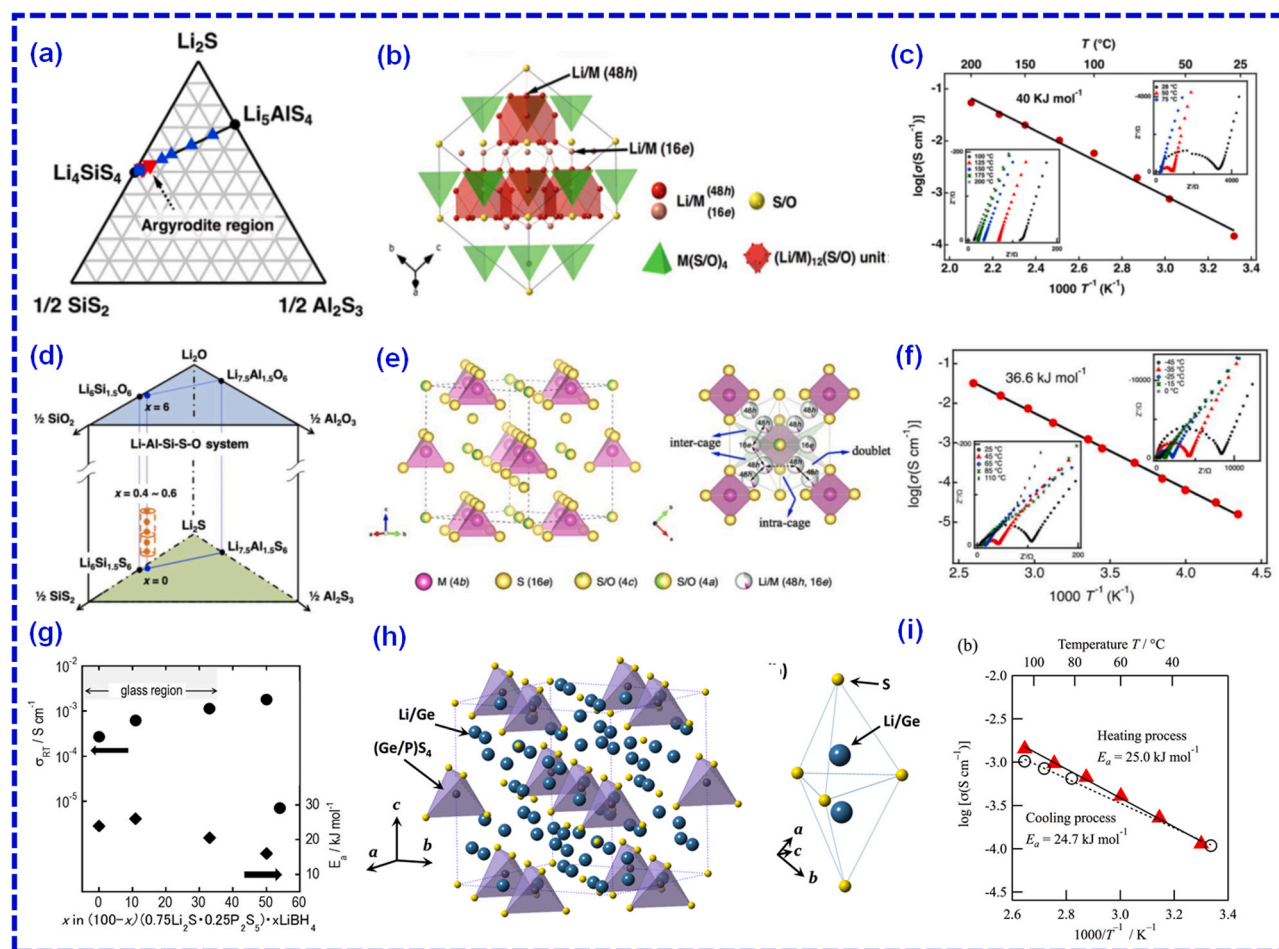


Fig. 9. (a) The phase diagram of the $\text{Li}_2\text{S}-\text{Al}_2\text{S}_3-\text{SiS}_2$ system. The blue triangle represents the Al-rich Li_5AlS_4 region, the blue square represents the Si-rich Li_4SiS_4 region and the red triangle represents the argyrodite region. (b) The framework structure and lithium ions that participate in ionic conduction of the HT- $\text{Li}_{6.15}\text{M}_{1.5}\text{S}_6$ ($M = \text{Al}_{0.1}\text{Si}_{0.9}$) and (c) the corresponding Arrhenius plots [100]. (d) The schematic phase diagram of the Li-Al-Si-S-O system. The argyrodite-type phase appears in the region indicated by the dashed cylinder. (e) The framework structure of the HT-argyrodite $\text{Li}_{6.15}\text{Al}_{0.15}\text{Si}_{1.35}\text{S}_{5.4}\text{O}_{0.6}$ (left) and the corresponding lithium diffusion pathways consist of three kinds of lithium jumps (right). The solid line, dashed line and dotted line represents the doublet, the intra-cage and the inter-cage lithium jumps, respectively. (f) The Arrhenius plot of $\text{Li}_{6.15}\text{Al}_{0.15}\text{Si}_{1.35}\text{S}_{5.4}\text{O}_{0.6}$ measured between -45 and 110°C [101]. (g) Ionic conductivity and the corresponding activation energy of $(100-x)(0.75\text{Li}_2\text{S}\cdot 0.25\text{P}_2\text{S}_5)\cdot x\text{LiBH}_4$ solid electrolytes at various compositions. [102] (h) **Left:** Crystal structure of the argyrodite-type $\text{Li}_7\text{Ge}_3\text{PS}_{12}$. The yellow and blue spheres correspond to S and Li/Ge atoms, respectively; the purple tetrahedron represents the $(\text{Ge}/\text{P})\text{S}_4$ units. **Right:** the coordination environment of the $(\text{Li}/\text{Ge})\text{S}_4$ tetrahedron. (i) Temperature-dependent ionic conductivity of $\text{Li}_7\text{Ge}_3\text{PS}_{12}$ electrolytes. The bold red triangles and hollow black circles represent the Li^+ conductivity of $\text{Li}_7\text{Ge}_3\text{PS}_{12}$ during heating and cooling processes, respectively [87].

face-shared $(\text{Li}/\text{M})(\text{S}/\text{O})_4$ tetrahedrons. The high Li^+ conductivity of HT- $\text{Li}_{6.15}\text{M}_{1.5}\text{S}_6$ is attributed to the disordered arrangement of Li^+ ions at the 48 *h* site together with Li^+ ions at the 16*e* site. This is a characteristic of HT-argyrodite ion conductors.

To further stabilize the argyrodite structure in the above Li-Al-Si-S system, O substitution is an effective strategy to enhance the structural stability and reproducibility of the relevant argyrodite phase at room temperature. A new family of lithium argyrodite electrolytes is summarized based on the Li-Al-Si-S-O diagram as shown in Fig. 9d. The formation of a pure argyrodite phase based on this new argyrodite family was highly dependent on the O content in the structure. Moreover, the oxygen-substituted samples showed significant improvement on ionic conductivity than previous results [101]. An amorphous phase occurred when the O content was too low, while secondary phases emerged at high oxygen contents. The composition was carefully optimized to $\text{Li}_{6.15}\text{Al}_{0.15}\text{Si}_{1.35}\text{S}_{5.4}\text{O}_{0.6}$ for a maximized Li^+ conductivity. As shown in Fig. 9e, the framework of $\text{Li}_{6.15}\text{Al}_{0.15}\text{Si}_{1.35}\text{S}_{5.4}\text{O}_{0.6}$ mainly consists of $M(4b)\text{S}_4(16e)$ ($M = \text{Al}_{0.1}\text{Si}_{0.9}$) tetrahedrons with isolated S/O ions at the 4*a* and 4*c* sites. The disordered Li/M ions are located at the tetrahedral 48 *h* and 16*e* sites, forming three possible Li^+ migration pathways in the argyrodite structure. Fig. 9e depicts the three typical

types of Li^+ jumps including the doublet jumps (solid line), the inter-cage jumps (dashed line) and the intra-cage jumps (dotted line). As shown in Fig. 9f, $\text{Li}_{6.15}\text{Al}_{0.15}\text{Si}_{1.35}\text{S}_{5.4}\text{O}_{0.6}$ had an ionic conductivity of 1.24 mS/cm at room temperature with an activation energy of 36.6 kJ/mol. The room-temperature ionic conductivity was almost four orders of magnitude higher than that of the thio-LISICON $\text{Li}_{4+x}\text{Al}_x\text{Si}_{1-x}\text{S}_4$ electrolytes [101].

Introduction of LiBH_4 into the sulfide glass matrix of $75\text{Li}_2\text{S}\cdot 25\text{P}_2\text{S}_5$ has been reported to improve the ionic conductivity. The ionic conductivity of $(100-x)(0.75\text{Li}_2\text{S}\cdot 0.25\text{P}_2\text{S}_5)\cdot x\text{LiBH}_4$ increased with increasing LiBH_4 content when *x* was in the range of $0 \leq x \leq 0.33$ [102]. High ionic conductivity up to 1.6 mS/cm at room temperature was demonstrated. At a higher LiBH_4 content ($x > 0.33$), the system turned into a family of lithium argyrodites, $\text{Li}_{7-x}\text{PS}_{6-x}(\text{BH}_4)_x$ (Fig. 9g). The BH_4 ions occupy the sites of Cl⁻ or Br⁻ ions based on the $\text{Li}_{7-x}\text{PS}_{6-x}\text{X}_x$ ($X = \text{Cl}, \text{Br}$) structure. The optimal composition $\text{Li}_6\text{PS}_5(\text{BH}_4)$ demonstrated a high Li^+ conductivity of 1.8 mS/cm at 25°C with an activation energy of 16 kJ/mol. The disorder of the $\text{S}^{2-}/\text{BH}_4$ distribution in the structure was essential [102]. A new kind of halogen-free stable lithium argyrodite, $\text{Li}_7\text{Ge}_3\text{PS}_{12}$, has been designed based on the ternary $\text{Li}_2\text{S}-\text{GeS}_2-\text{P}_2\text{S}_5$ system, which it is not originated from Li_7PS_6 [87]. Fig. 9h shows the

structure of the argyrodite-type $\text{Li}_7\text{Ge}_3\text{PS}_{12}$, in which Li^+ ions are distributed at the tetrahedral $48h$ site of a bi-pyramidal structure formed by two LiS_4 tetrahedrons connected through face sharing. The ionic conductivity of $\text{Li}_7\text{Ge}_3\text{PS}_{12}$ was 1.1×10^{-4} S/cm at room temperature (Fig. 9i). The activation energy of $\text{Li}_7\text{Ge}_3\text{PS}_{12}$ during the heating process was 25 kJ/mol, which is lower than that of Li_7PS_6 (32 kJ/mol). More recently, Strauss et al. [103] reported a metastable lithium argyrodite with the composition of $\text{Li}_7\text{GeS}_5\text{Br}$, showing an ionic conductivity of 0.63 mS/cm at 298 K with an activation energy of 0.43 eV.

4. Applications of lithium argyrodites in solid-state batteries

Since the discovery of Li argyrodites in 2008, the exploration of Li argyrodites as solid-state electrolytes (SSEs) for advanced all-solid-state batteries (ASSBs) has gained significant attention and achieved impressive progress. The electrochemical performance and cell design of different types of ASSBs using Li argyrodites as the electrolyte are summarized in Table S2 of Supplementary Information. In the early stage, it is very challenging to use the high-conductivity Li argyrodites ($\text{Li}_6\text{PS}_5\text{Cl}$ and $\text{Li}_6\text{PS}_5\text{Br}$) directly as the SSE layer or as a component for cathode composites [44,104,105]. Based on computational and experimental studies, it is widely acceptable that the major reason is originating from the interfacial problems towards either anode or cathode [45,106–114]. In this section, we summarize the interfacial issues at the Li metal/Li argyrodites and cathode/Li argyrodites interfaces. Meanwhile, the important but easily overlooked problem of the Li argyrodites themselves, the cognition of interface within the electrolytes and the degradation of the interface in full cells are overviewed. We also review the existing strategies that can boost the development of

high-performance ASSBs based on the Li argyrodites. Furthermore, we emphasize the significance of optimizing the fabrication process of using Li argyrodites. The solvent-related process for Li argyrodites is distinct from handling other SSEs, which plays an important role to facilitate the successful application of Li argyrodites in AASBs.

4.1. Interfacial challenges and electrochemical stability

Rather than the sluggish kinetics at the interface, the interfacial incompatibility is regarded as more of the essential obstacles that hinder the application of Li argyrodites [115]. The side reactions at interface with anode or cathode, the formation of Li dendrites and the incompatibility between oxide-based cathode materials and sulfide electrolytes are outstanding problems at the interface [116]. Meanwhile, the redox activities of the Li argyrodites themselves during electrochemical cycling are attracting increasing attention. The battery capacity contribution could be confusing in the presence of Li argyrodites. All these problems are reflected in full-cell performance, complicating the degradation mechanism.

4.1.1. Li metal anode interface

Due to the strong reducing capability of Li metal, all sulfide-based SSEs can be reduced by Li metal upon electrochemical cycling or even upon contact [117,118]. Early in 2015, Zhu et al. used computational simulation to determine the reduction potential of $\text{Li}_6\text{PS}_5\text{Cl}$ SSEs as 1.71 V (vs. Li/Li^+ , the same reference potential hereafter) and revealed the reduction products at the $\text{Li}/\text{Li}_6\text{PS}_5\text{Cl}$ interface as P, Li_2S and LiCl [107]. This is experimentally verified by Wenzel et al. [108] in 2018. They used X-ray photoelectron spectroscopy (XPS) combining with Li metal deposition and time-resolved electrochemical impedance

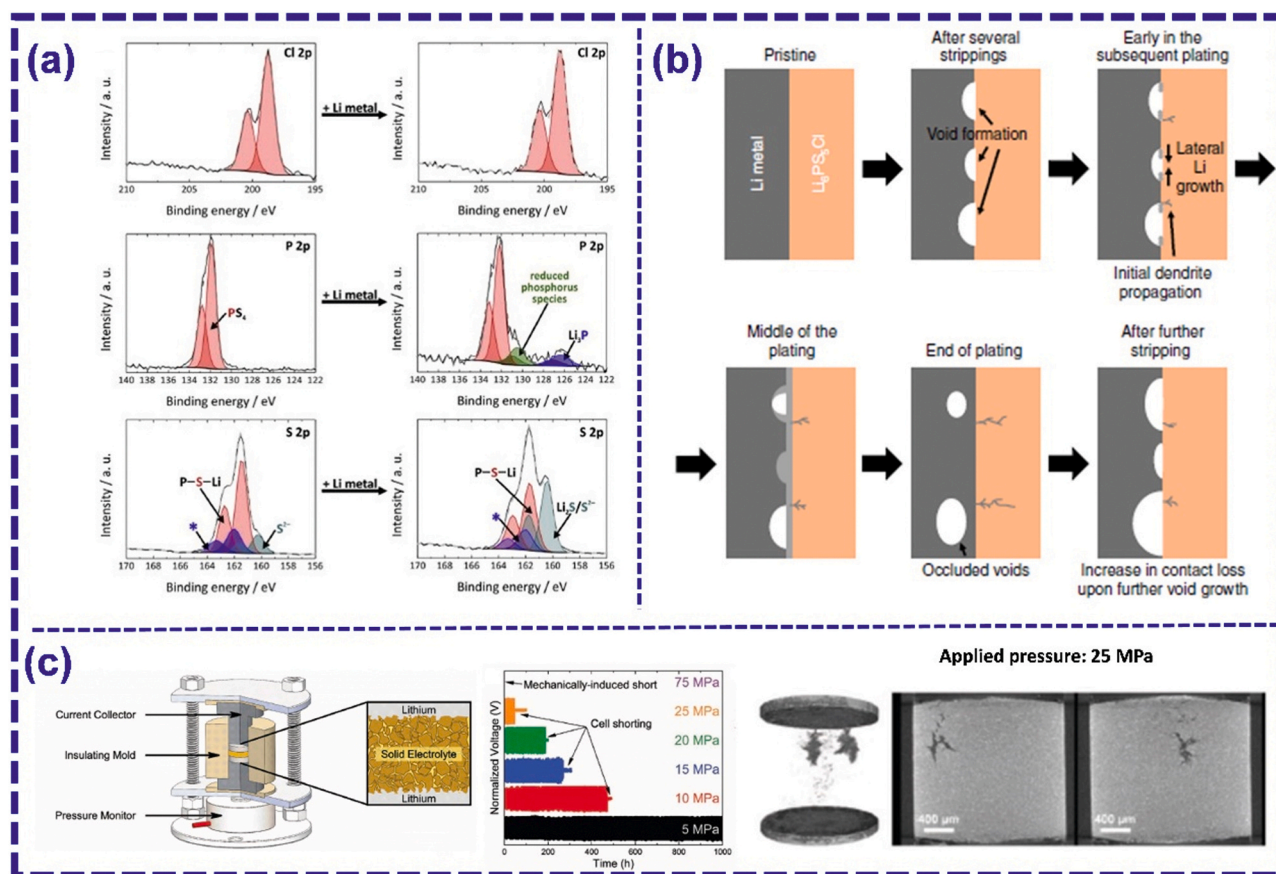


Fig. 10. Challenges of the Li-anode/Li-argyrodites interface. (a) XPS characterization of the interfacial composition between Li metal and $\text{Li}_6\text{PS}_5\text{Cl}$ SSEs [108]. (b) Schematic diagram of the formation of voids at the Li/Li-argyrodites interface [122]. (c) Pressure effect on the performance of Li/ $\text{Li}_6\text{PS}_5\text{Cl}$ /Li symmetric cells [123].

spectroscopy (EIS) to investigate the interfacial composition formed in-situ between Li metal and $\text{Li}_6\text{PS}_5\text{X}$ ($\text{X} = \text{Cl}, \text{Br}, \text{I}$) SSEs. The decomposed interphase of $\text{Li}/\text{Li}_6\text{PS}_5\text{X}$ mainly consisted of Li_3P , Li_2S and LiX compounds (Fig. 10a). The degradation of SSEs led to increased interfacial impedance.

Growth of Li dendrites is another problem at the interface between Li metal anode and Li argyrodites [117,119–121]. The uneven Li deposition at the anode interface causes that the Li dendrites penetrate through the grain boundary or the voids among the bulk of Li argyrodites, which deteriorates the battery. Very recently, Kasemchainan et al. [122] demonstrated that the critical current density is crucial for the Li plating and stripping behaviors using $\text{Li}_6\text{PS}_5\text{Cl}$ SSEs. As illustrated in Fig. 10b, once the Li is removed from the interface at a current density faster than it can be replenished, voids are generated in the Li bulk near the interface with the SSE layer and accumulate upon following cycles. The edges of these voids localize a higher current density than elsewhere and ultimately leads to Li dendrites formation. The stack pressure is another important factor that can determine the formation of Li dendrites. As shown in Fig. 10c, Doux et al. [123] designed a special cell with the feature of adjustable pressure and emphasized the importance of a reasonable pressure for long-life cycling of $\text{Li}/\text{Li}_6\text{PS}_5\text{Cl}/\text{Li}$ symmetric

cells. A suitable pressure can ensure a good contact between the Li metal and the $\text{Li}_6\text{PS}_5\text{Cl}$ SSEs in spite of the volume fluctuations of the Li metal electrodes during long-term cycling. Nevertheless, excess pressure (for example 25 MPa) showed inverse effect because the Li can creep into the pores of $\text{Li}_6\text{PS}_5\text{Cl}$ SSEs under high pressure and accelerated the growth of Li dendrites.

4.1.2. Cathode interface

Early in 2012, Boulineau et al. [44] experimentally demonstrated that $\text{Li}_6\text{PS}_5\text{X}$ ($\text{X} = \text{Cl}, \text{Br}$) SSEs can support reversible Li intercalation/deintercalation for LiCoO_2 (LCO) cathode materials (redox potential ~ 3.9 V, theoretical capacity ~ 140 mAh g^{-1}). However, the ASSB delivered limited reversible capacity of 46 mAh g^{-1} even at a low current density of 64 $\mu\text{A cm}^{-2}$. Zhu et al. [107] predicted the oxidation onset potential of $\text{Li}_6\text{PS}_5\text{Cl}$ SSEs to be 2.01 V with decomposed products of Li_3PS_4 , LiCl and S compounds. The degradation of $\text{Li}_6\text{PS}_5\text{Cl}$ at high voltages might be one of the major reasons for the low battery capacity output.

Even though the Li argyrodites show narrow electrochemical stability windows, the interfacial stability of the sulfide-based SSEs towards cathode materials has drawn significant interests since 2017. Auvergniot

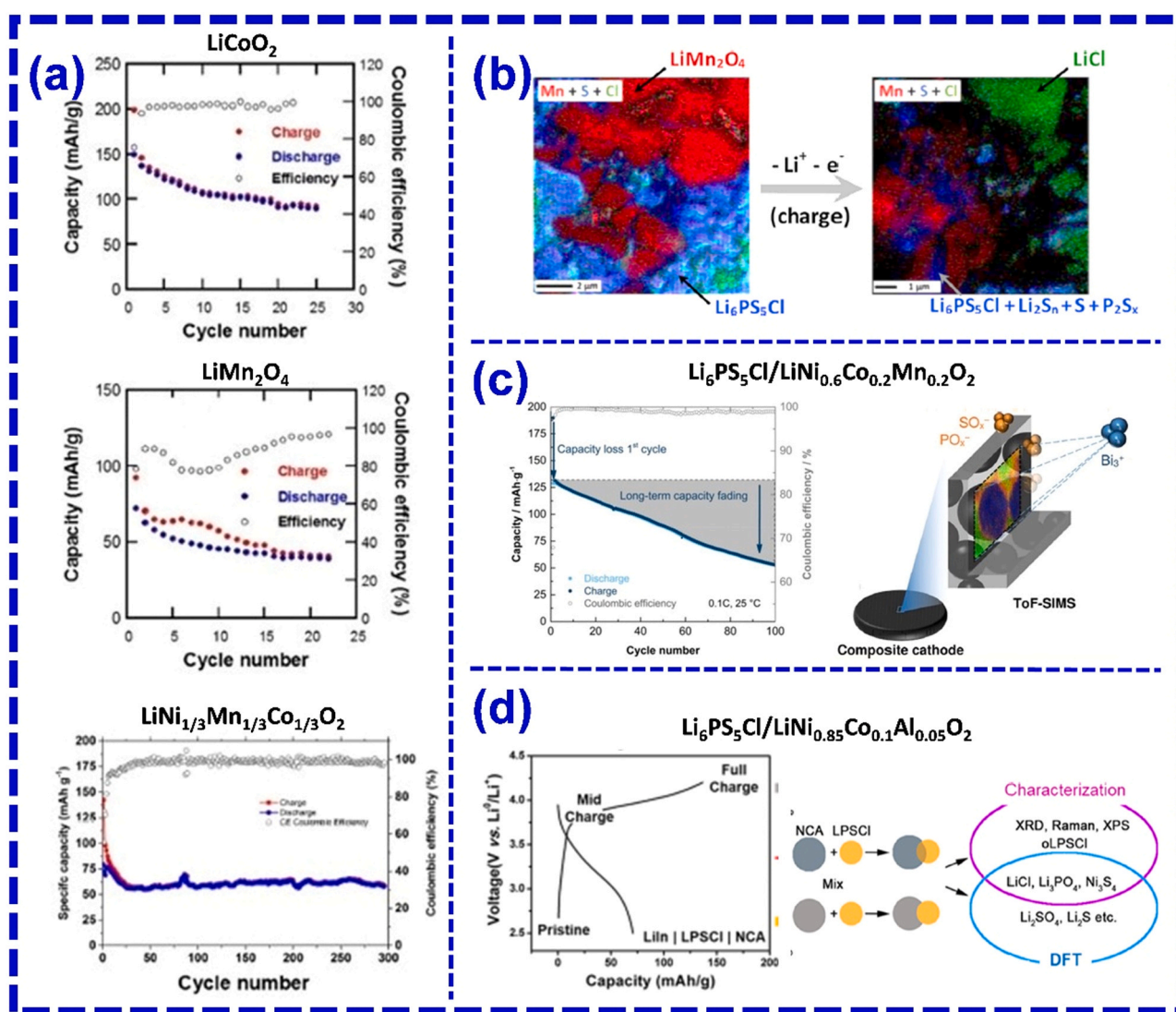


Fig. 11. Challenges of the cathode/argyrodite interface. (a) Cycling performance of ASSBs using Li Argyrodite electrolytes and different popular cathode materials [109]. (b) Using SAM to map the distribution of interfacial reaction products between $\text{Li}_6\text{PS}_5\text{Cl}$ SSEs and LMO cathode materials [109]. (c) Using TOF-SIMS to know the interface component between $\text{Li}_6\text{PS}_5\text{Cl}$ and NCM622 cathode materials [110]. (d) Experimental routes of studying the interface problem between $\text{Li}_6\text{PS}_5\text{Cl}$ and NCA cathode materials [111].

et al. [109] first studied the interfacial compatibility of argyrodite $\text{Li}_6\text{PS}_5\text{Cl}$ toward three kinds of popular cathode materials: LCO, $\text{LiNi}_{1/3}\text{Co}_{1/3}\text{Mn}_{1/3}\text{O}_2$ (NCM) and LiMn_2O_4 (LMO). As shown in Fig. 11a, rapid capacity decay was observed in all three cases. The XPS analyses to identify the side reaction products (such as S, polysulfides, P_2S_x , LiCl, Li_2S_x and even phosphates) from $\text{Li}_6\text{PS}_5\text{Cl}$ and the cathode active materials at the interface. Scanning auger microscopy (SAM) was employed to map the distribution of these products (Fig. 11b). After charging, the distribution of $\text{Li}_6\text{PS}_5\text{Cl}$ was overwhelmed by its decomposition products. Furthermore, Walther et al. [110] utilized time-of-flight secondary ion mass spectrometry (TOF-SIMS) to observe the interfacial composition between $\text{Li}_6\text{PS}_5\text{Cl}$ and $\text{LiNi}_{0.6}\text{Co}_{0.2}\text{Mn}_{0.2}\text{O}_2$ (NCM622) cathode materials (Fig. 11c). The interested interface was mainly composed of sulfates and phosphates, while transition-metal chlorides, phosphides, and sulfides can be neglected. Moreover, Banerjee et al. [111] segregated the effects of spontaneous reaction of $\text{Li}_6\text{PS}_5\text{Cl}$ SSEs and $\text{LiNi}_{0.85}\text{Co}_{0.1}\text{Al}_{0.05}\text{O}_2$ (NCA) cathode materials at the interface. By using various synchrotron-based characterization tools and first-principles calculations, the intrinsic electrochemical decomposition was studied (Fig. 11d). The interfacial products were Ni_3S_4 , LiCl, Li_3PO_4 and oxidized $\text{Li}_6\text{PS}_5\text{Cl}$ from the spontaneous chemical reaction between NCA and $\text{Li}_6\text{PS}_5\text{Cl}$.

4.1.3. Probing Li^+ transport at the interface

The interfacial ionic transport plays an important role in determining the electrochemical performance of ASSBs, but it is still very challenging to qualitatively or quantitatively study the Li^+ transport at the SSE/electrode interface. The limited knowledge regarding the interfacial ionic transport is promoting worldwide researchers to develop new characterization methods understanding the Li^+ motion at interface. To date, ^7Li solid-state NMR is one of few characterization methods reported give hints on the interfacial Li^+ transport. The ^7Li solid-state NMR probes local chemical environment of Li via the chemical shift

(resonance line positions) and quadrupolar interactions. If there are distinguished chemical shifts among different components, solid-state NMR can be used to identify the spontaneous Li-ion exchange between multiple Li-containing phases. In other words, it is possible to study the Li-ion exchange for interface between multiple electrode phases or a mixture of electrode and SSE. Yu et al. [45] performed one-dimensional ^7Li NMR exchange analyses to unambiguously characterize Li-ion transport across the interface of $\text{Li}_6\text{PS}_5\text{Cl}$ and Li_2S , giving direct quantitative insight into the impact of the interfacial Li^+ transport on all-solid-state batteries. The Li^+ transport across the $\text{Li}_6\text{PS}_5\text{Cl}/\text{Li}_2\text{S}$ interface was dramatically slower than that in the bulk $\text{Li}_6\text{PS}_5\text{Cl}$. In addition, two-dimensional exchange ^7Li NMR spectroscopy provides unique quantitative insight into the spontaneous Li-ion exchange at the interface of $\text{Li}_6\text{PS}_5\text{Br}/\text{Li}_2\text{S}$. As shown in Fig. 12a, the different chemical shifts of Li in $\text{Li}_6\text{PS}_5\text{Br}$ and Li_2S phases helped to distinguish Li^+ motions in the two phases. The Li^+ transport behaviors across the interface of the $\text{Li}_6\text{PS}_5\text{Br}/\text{Li}_2\text{S}$ mixture were analyzed at different stages in the electrode preparation process as well as before and after battery cycling. The study on the evolution of the resistance between the Li_2S cathode materials and the $\text{Li}_6\text{PS}_5\text{Br}$ SSEs was presented [106]. It is demonstrated that interfacial Li^+ transport across the electrode/electrolyte interfaces is the rate-limiting step for the overall Li^+ transport in ASSBs. The volumetric changes and redox instabilities of Li_2S electrode materials is responsible for the increase in impedance, which influences the interfacial composition and then the battery performance.

4.1.4. Redox activity of the argyrodite SSEs

Based on the calculation result by Zhu et al. [107], $\text{Li}_6\text{PS}_5\text{Cl}$ has a very narrow electrochemical stability window between 1.07 and 2.01 V. Revisiting reported data in Li-S ASSBs, the initial reversible capacities are obviously higher than theoretical capacities of Li_2S or S cathode materials (Fig. 12b) [48,50,55,126], which means that the decomposition of $\text{Li}_6\text{PS}_5\text{Cl}$ may be reversible to some extent. This is an important,

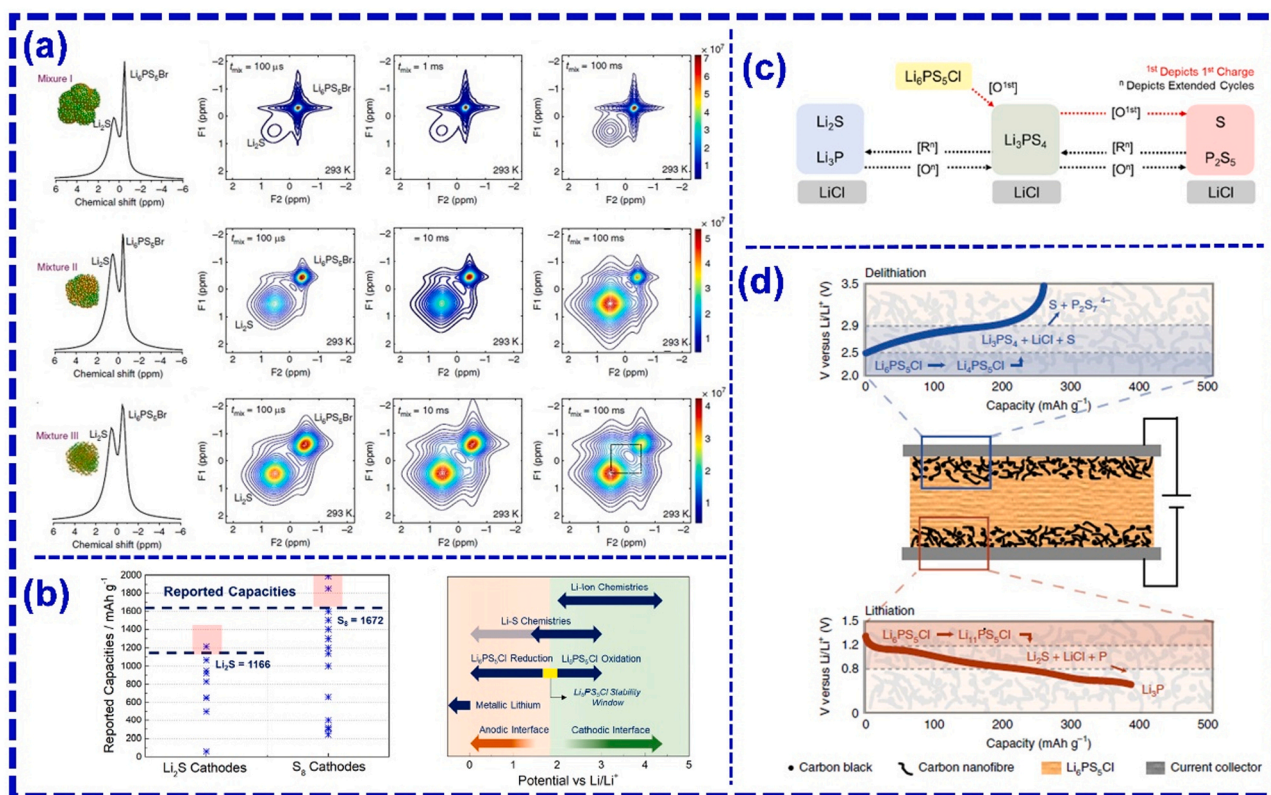


Fig. 12. (a) 2D NMR spectra for understanding the Li^+ conduction at the interface between $\text{Li}_6\text{PS}_5\text{Br}$ electrolyte and Li_2S cathode [106]. (b) Redox activity of Li argyrodites [124] and (c) the proposed reaction mechanism of $\text{Li}_6\text{PS}_5\text{Cl}$ [124]. (d) Lithiation and delithiation route of $\text{Li}_6\text{PS}_5\text{Cl}$ at different voltages [125].

but easily be neglected issue that the redox of Li Argyrodite SSEs can contribute to some reversible capacity in an appropriate working voltage range, while the redox reaction is believed not completely reversible. This was first pointed out by Auvergniot et al. [127] in 2017. Recently, Tan et al. [124] combined CV results of the Li-In/Li₆PS₅Cl/Li₆PS₅Cl-S cell in a voltage range of 0–4.2 V (vs. Li/Li⁺) with the ex-situ characterizations of XRD, XPS, Raman and MAS NMR to propose a possible mechanism based on the redox reaction of Li₆PS₅Cl SSE. Upon first charging, Li₆PS₅Cl is oxidized to Li₃PS₄, S and LiCl, but the process becomes really complicated during the subsequent charging and discharging cycles. Nevertheless, there is a redox reaction between the oxidants of Li₃PS₄, S and P₂S₅ and the reductants of Li₂S and Li₃P. Fig. 12c outlines the redox process for Li₆PS₅Cl. Meanwhile, Schwietert et al. [125] published their results to clarify the relationship between redox activity and electrochemical stability of Li₆PS₅Cl SSE. Although the oxidation and reduction reactions of Li₆PS₅Cl SSE occur at different voltages (as depicted in Fig. 12d), the authors believe that the practical electrochemical stability window of Li₆PS₅Cl based SSEs should be determined by the oxidation and reduction onset potentials of S and P for a broader context. The reversible redox beyond the Li₆PS₅Cl phase can help to explain the viable integration of Li₆PS₅Cl SSE and high-voltage cathode materials. Overall, the redox activity is one of the intrinsic properties for the Li argyrodite SSEs, which is due to the low anodic stability and high cathodic stability of sulfides. The redox reaction is not completely reversible, but inevitable for the applications of lithium argyrodites. However, the stabilized interphase derived from the redox reaction of lithium argyrodites (e.g., Li₆PS₅Cl) can deliver a higher practical electrochemical window compared with the theoretically calculated window (1.07–2.01 V), which can benefit to the application of lithium argyrodites for high-voltage ASSBs.

4.2. Strategies to improve the performance of argyrodites-based ASSBs

Good interfaces are regarded as a key to the success of ASSBs. Therefore, alleviating the interfacial problems discussed above is essential for realizing high-performance ASSBs. For the anode, using In or Li-M alloys (M = Sn, Al, Mg, etc.) instead of Li metal can achieve a relatively stable anode/SSEs interface, but at a cost of lower energy density because these alternative anodes have higher potential than Li

metal and thus lower working voltage for full cells. At cathode side, coating ionic conductive oxides (such as LiNbO_x, LiTaO_x, LiZrO_x, Li_{0.5}La_{0.5}TiO₃, etc.) on cathode materials is widely adopted to mitigate the side reactions between oxide cathodes and sulfide SSEs for interfacial compatibility [6,128–131]. Even though these strategies should be easily transferable to Li-argyrodite based ASSBs, but to our best knowledge, there is only a few strategies that are designed particularly for solving cathode/Li-argyrodites interfacial problems. Herein, we will focus on reviewing the development of Li-argyrodite electrolytes and their related effects on ASSBs performance. Strategies with successful demonstrations of improved performance of Li-argyrodite based ASSBs are also discussed.

4.2.1. Doping electrolyte

Effective anion or cation doping can improve the chemical and electrochemical stabilities of Li argyrodites (Fig. 13a). Zhang et al. [52] reported that O²⁻ can substitute the free S²⁻ anions in the crystal structure of Li₆PS₅Br. The Li₆PS_{5-x}O_xBr SSEs (0 ≤ x ≤ 1) with moderate concentration of O²⁻ can maintain an ionic conductivity above 1 × 10⁻³ S cm⁻¹. Importantly, the Li compatibility, high voltage compatibility and air stability were improved. The oxide-related chemistry helped to stabilize electrode/SSEs interface and improved the stability of Li-argyrodites in air [132]. Zhao et al. [133] adopted the favorable LiF-rich interface for stable Li anode interface. They incorporated F in the Li₆PS₅Cl host by partially replacing LiCl raw materials with LiF. The fluorinated Li-argyrodite electrolyte demonstrated excellent Li/SSEs interfacial stability, showing stable Li plating/stripping at a superhigh current density of 6.37 mA cm⁻² and a cutoff capacity of 5 mAh cm⁻² for over 250 h. The same group also proposed versatile Sn doping in Li₆PS₅I that achieved significantly increased the ionic conductivity (125 times increase) of relevant SSEs, good Li metal compatibility and air stability [96]. The highly ionic conductive electrolytes stabilized the Li metal interface with the LiI-containing interface, while the strong Sn-S chemical bonds improved resistance against oxidation in air. With an effective engineering strategy, the once unpopular Li₆PS₅I SSE can become favorable. Chen et al. [134] creatively used ZnO to co-dope Zn²⁺ and O²⁻ for a series of novel Li_{6-2x}Zn_xPS_{5-x}O_xBr SSEs. The Zn²⁺ was doped at the Li⁺ site and the O²⁻ partly occupy the position of free S²⁻. The Zn²⁺ doping introduced Li vacancies and ensured high ionic

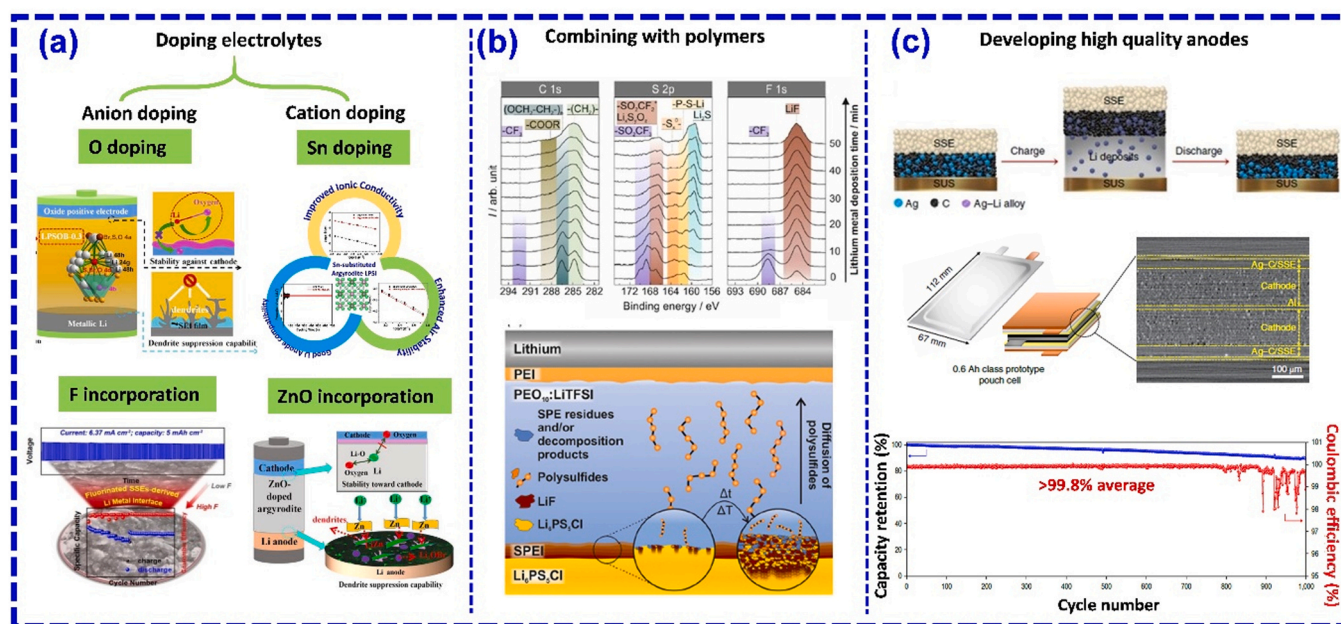


Fig. 13. Strategies to improve the performance for argyrodite-based ASSBs by (a) element doping [52, 96, 133, 134], (b) composite with polymers [136,137] and (c) development of Li-free anodes [138].

conductivities at the level of $1 \times 10^{-3} \text{ S cm}^{-1}$. Meanwhile, the in-situ formed Li-Zn alloy was beneficial to a stable Li metal/SSEs interface. Considering the effects of O incorporation, compatibility between the Li-argyrodite electrolyte and cathode was improved. Very recently, it is reported that the off-stoichiometric Li-argyrodites (e.g., $\text{Li}_{6.25}\text{PS}_{5.25}\text{Cl}_{0.75}$ and $\text{Li}_{5.5}\text{PS}_{4.5}\text{Br}_{1.5}$) with excess or deficient Li can be used directly with Li metal in full ASSBs for reversible electrochemical cycling [80,135]. However, the underlining mechanism is still poorly understood.

4.2.2. Composite with polymers

Composite polymer electrolytes (CPEs) were developed to improve the mechanical property and the interface stability toward Li metal. Simon et al. [136] reported successful fabrication of CPEs with PEO_{20} :LiTFSI and $\text{Li}_6\text{PS}_5\text{Cl}$ fillers by a scalable slurry-based process. The occurrence of LiF, polysulfides and Li_3PO_4 on the CPE surface was originated from the minor decomposition reactions between PEO_{20} :LiTFSI and $\text{Li}_6\text{PS}_5\text{Cl}$. The Li metal compatibility of this CPE was attributed to the in-situ generated LiF and Li_2S SEI components, which was characterized by the in-situ XPS and TOF-SIMS analyses (Fig. 13b). Four-point electrochemical impedance measurements determined the interface impedance to be as low as 2.4Ω at 80°C [137]. The low resistance and low activation energy of this electrochemically formed interface can protect $\text{Li}_6\text{PS}_5\text{Cl}$ from further decomposition at the Li anode interface.

4.2.3. Development of high-quality anode

Recently, Lee et al. [138] present a milestone performance of pouch cells using $\text{Li}_6\text{PS}_5\text{Cl}$ as the SSE, an in-house designed Ag-C anode and a Li_2O -ZrO (LZO) coated high-Ni NMC cathode. The pouch-type ASSBs realized a high areal capacity of 6.8 mAh cm^{-2} and high energy density of more than 900 Wh L^{-1} with an impressive electrochemical cycling ability over 1000 cycles at 60°C . The ultrathin Ag-C anode can

effectively regulate Li deposition and avoid growth of Li dendrites (Fig. 13c). This anode-free strategy eliminates the pre-loading of Li metal and solved problematic interface between fresh Li metal and $\text{Li}_6\text{PS}_5\text{Cl}$.

4.3. Influence of electrode processing and other factors

In addition to the intensive interfacial engineering efforts, a rational fabrication process for ASSBs is also highly related to the final battery performance. Since Li-argyrodites that can be prepared via liquid-phase routes [139], liquid-involved methods become possible for optimizing the fabrication process and integrating the electrodes, electrolytes and separators in different configurations. Contact between active materials and Li-argyrodites and grain boundaries in bulk SSEs must be considered. Moreover, the effects of binders and electronic conductive additives may not be straight forward.

4.3.1. Solvent-involved processing

Non-polar and weak-polar solvents, such as acetonitrile, ethyl propionate and ethanol (EtOH), are regarded as good candidates to dissolve the Li argyrodites with little degradation effect on the SSEs. In the reported studies, EtOH is the most widely used for the solvent involved process for Li argyrodites synthesis. The dissolution-precipitation method enables rotational designs of electrolyte configurations and solid electrode fabrication. Kim et al. [140] reported a scalable fabrication protocol for composite electrodes using homogeneous $\text{Li}_6\text{PS}_5\text{Cl}$ solutions in EtOH. As shown in Fig. 14a, the $\text{Li}_6\text{PS}_5\text{Cl}$ solution was infiltrated into the porous structure of LCO or graphite-based electrodes, providing intimate ionic contacts and favorable ionic percolation. The $\text{Li}_6\text{PS}_5\text{Cl}$ -infiltrated LCO and graphite electrodes showed superior battery performance than the electrodes obtained from conventional dry-mixing. The ASSB performance was even comparable to many liquid-electrolytes based cells. The similar process was adopted to

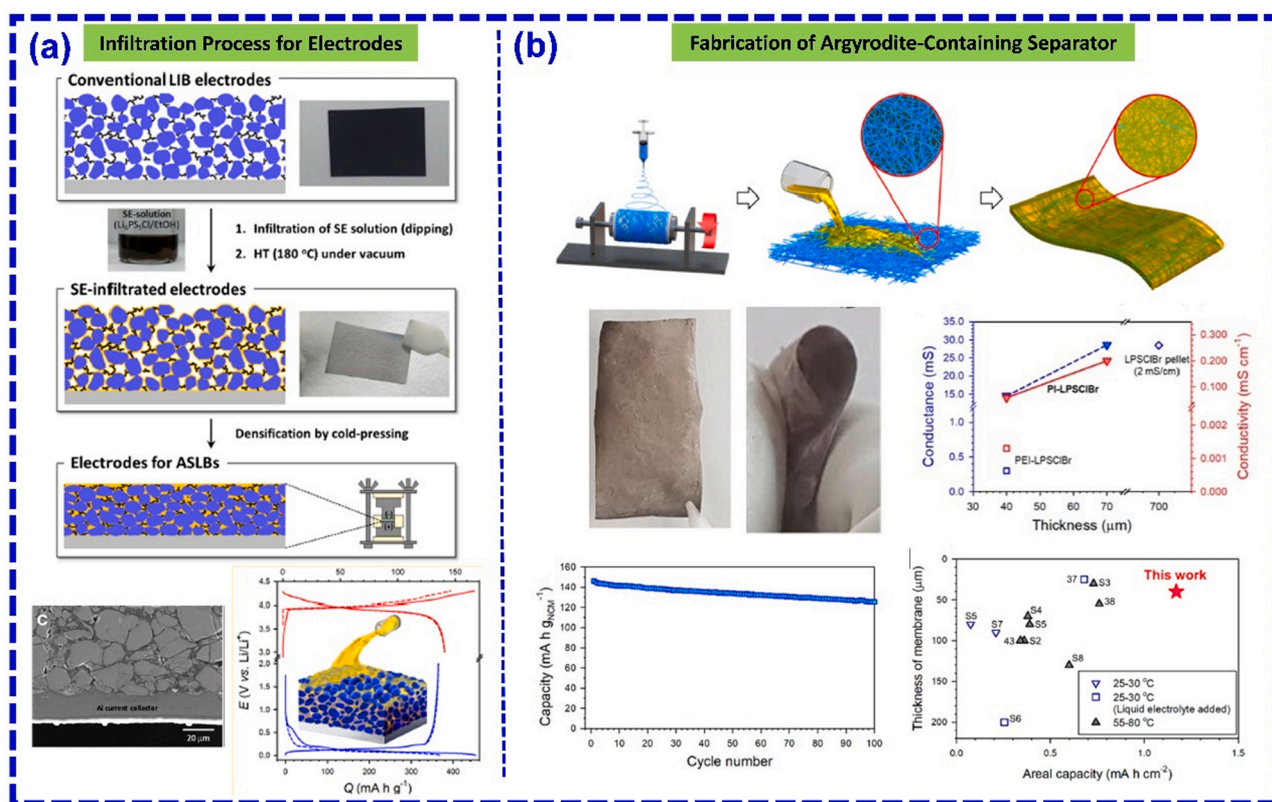


Fig. 14. Solvent-involved processes for better electrochemical performance. (a) The infiltration process for preparing $\text{Li}_6\text{PS}_5\text{Cl}$ based composite cathode [140]. (b) Preparation of thin SSE separators from a $\text{Li}_6\text{PS}_5\text{Cl}_{0.5}\text{Br}_{0.5}$ -EtOH solution and ASSBs performance using this thin SSE [141].

fabricate sheet-type Si electrodes [142]. Furthermore, they developed a new scalable fabrication process for thin (40–70 μm) and flexible Li^+ ion conducting membranes with high ionic conductivity and excellent thermal stability (up to $\sim 400^\circ\text{C}$) [141]. It was benefited from the porous structure and high thermal stability of polyimide nonwovens and highly conductive $\text{Li}_6\text{PS}_5\text{Cl}_{0.5}\text{Br}_{0.5}$ impregnation. Promising electrochemical performance at 30°C and excellent thermal stability were demonstrated by ASSBs using this ionic conductive membrane as separator, composite $\text{LiNi}_{0.6}\text{Co}_{0.2}\text{Mn}_{0.2}\text{O}_2$ cathode and composite graphite anode (Fig. 14b).

4.3.2. Binder effect

For practical applications, the polymer binder is essential and widely used to estimate the strain/stress and alleviate the volume change during the lithiation/delithiation of active electrode materials. For the fabrication of solid-state electrodes via solvent-involved methods, Navarro et al. [143] and Zhang et al. [144] demonstrated significantly enhanced capacity retention of NCM cathodes and improved cycling lives by introducing 0.5–1 wt% ethyl cellulose into the electrodes as binder. Their studies suggest that smooth Li^+ migration and stable interface between the active materials particles and Li argyrodites can be facilitated by an optimal content of a chemically compatible binder.

4.3.3. Electronic additive agent

Although interfacial electronic conductivity could accelerate the decomposition of sensitive SSEs at the electrode interface due to increased side reactions with enough electrons, electronic additives is essential for active materials with low intrinsic electronic conductivity. Strauss et al. [145] used the high-loading pelletized ASSBs as the prototype to study the effect of the carbon black with different specific surface areas. Size and LiNbO_3 surface coating of the Ni-rich layered oxide cathode (NCM 622) are tailored carefully to ensure uniformity. Their electrochemical performance results indicate that the addition of 1 wt% Super C65 carbon black (low surface area: $65\text{ m}^2\text{ g}^{-1}$) can improve the capacity and cycling stability compared to the additive-free cells, but the high-surface-area Ketjenblack (KB, $1400\text{ m}^2\text{ g}^{-1}$) exerted a severe negative effect on the cycling performance and interfacial stability.

5. Conclusions and perspective

Solid electrolytes are a critical component of next-generation solid-state batteries. Li-argyrodite electrolytes are a group of promising candidates with low cost, high ionic conductivity, good compatibility and favorable mechanical properties for solid-state batteries. The solid-state synthesis route is easy to scale up and produce repeatable Li-argyrodites with high ionic conductivity, while the wet chemical synthesis route can be a tool for designing a rational interface or composite electrodes with special configurations. Elementary Li-argyrodite electrolytes (e.g., Li_7PS_6 and $\text{Li}_6\text{PS}_5\text{Cl}$) have an adequate ionic conductivity at room temperature ($10^{-4}\sim 10^{-3}\text{ S/cm}$). Engineering strategies such as optimization of the synthesis parameters, partial substitution of the constituent elements and introduction of Li vacancies provide opportunities for higher Li^+ conductivities. As a classic example, the introduction of Cl^- or Br^- partly in place of S^{2-} leads to enhancement of ionic conductivities when the lattice polarizability and the distributions of Cl^- or Br^- ions over the 4a and 4c sites are optimized in the structure. Furthermore, Li-argyrodite based solid-state batteries have been demonstrated with different types of cathodes including LCO, NMC and S-based cathodes. Ingenious design of Li anode is crucial for achieving excellent cycling performance.

This review has discussed the key research aspects for Li-argyrodites, covering the synthesis, the ionic conduction mechanism, challenges and strategies to realize applications in solid-state batteries. Fruitful results have been reported regarding the development of Li-argyrodite electrolytes in terms of ionic conductivity, chemical and electrochemical

stabilities, and attempts for solid-state batteries. However, there are still significant challenges to be overcome for practical applications. Here we provide our perspectives some important future directions for the further development of Li-argyrodite electrolytes for high-performance solid-state batteries:

(1) Designing new synthesis route for Li-argyrodites

Mechanical milling, solid-state reactions and wet chemical process are three major synthesis routes for Li-argyrodite electrolytes. Mechanical milling with or without subsequent annealing remains the most common method, but the requirement of high-energy and high-rotational-speed milling is costly, time-consuming and difficult to scale up. The direct solid-state reaction route involving heating a mixture of precursors is simple and easily scalable, however, the products might not be homogenous or of high purity. Although the wet chemical process offers unique opportunities for designing interface and electrode composites, the poor ionic conductivity of the products and the toxic organic solvents used during the synthesis processes need to be taken into consideration. Therefore, improvements in current synthesis routes or development of a new synthesis route with high quality, good scalability and low cost to obtain Li-argyrodites are vital to accelerate their applications.

(2) Enhancing ionic conductivity of Li-argyrodites

The state-of-the-art Li-argyrodite electrolytes have an ionic conductivity in the order of 10^{-3} S/cm at room temperature. Operation of solid-state batteries at moderate current densities under ambient temperature and at low current densities at significantly low temperature (-30°C) is possible. Further enhancement in the ionic conductivity of Li-argyrodites should render better rate capabilities for the solid-state batteries. Reported strategies to improve ionic conductivity include the optimization of synthesis parameters, creating Li vacancy in the structure, tailoring the element disorder over the 4a and 4c sites and partial substitution of the constituents. To date, the hot-pressed Li-argyrodite with an optimal Li vacancy, $\text{Li}_{5.5}\text{PS}_{4.5}\text{Cl}_{1.5}$, was reported to deliver the highest ionic conductivity up to 10^{-2} S/cm at room temperature, which is comparable to the ionic conductivity of most commercial liquid electrolytes. Enhancing the ionic conductivity of the cold-pressed Li-argyrodites close to or even higher than liquid electrolytes is meaningful for future investigations.

(3) Improving the chemical and electrochemical stabilities of Li-argyrodites

Although Li-argyrodites have a high ionic conductivity, their sensitivity to air and moisture is a big challenge. The synthesis and handling of Li-argyrodites require an inert atmosphere, strongly impeding its applications for solid-state batteries in large scales. The reasons for the instability of Li-argyrodites in the air are two-fold, water and oxygen.

The hydrolysis reactions between Li-argyrodites and water molecules in air generates harmful H_2S gas. Intensive effects have been made to enhance the chemical stability and the electrochemical windows of Li-argyrodites. Simulations and experimental results demonstrated the substitution of S with O as a promising strategy to improve moisture resistance and reduce H_2S generation upon air exposure [52,76,146–148]. Adjusting composition of the starting materials such as Li_2O partly in place of the Li_2S or P_2O_5 partly replacing P_2S_5 can dope O in to the argyrodite structure and improve the chemical stability in air and moisture [149–151]. Another solution to compensate the hygroscopic nature of sulfide electrolytes is to introduce an H_2S absorbent such as metal oxides (Fe_2O_3 , Bi_2O_3 , ZnO , etc.) [147, 151–153]. The metal oxides show a largely negative Gibbs energy change (ΔG) with H_2S for spontaneous reactions and effective reduction of H_2S release.

The stability of sulfide electrolytes follows the rules of the hard and soft (Lewis) acids and bases (HSAB) theory [154]. The Li-argyrodites are also chemically unstable with O₂, because O₂ as a hard base will react preferentially with the hard acid P to replace the soft base in the P-S framework of Li-argyrodites. Based on the HSAB theory, aliovalent substitution of P by Sn can enhance air-stability. In addition, tailoring the composition of Li-argyrodites may also improve the chemical stability. The presence of Li₂S impurity in the Li-argyrodite electrolytes has been reported to cause H₂S generation, hence reducing the Li₂S content in Li-argyrodites could improve air- and moisture-stability.

Moreover, the chemical instability of Li-argyrodites against Li metal was predicted by simulation and characterized experimentally. It is challenging to directly use Li-argyrodites with Li metal anodes. However, our ongoing work achieve stable cycling of solid-state Li metal batteries using a Li-argyrodite electrolyte (Li_{6.25}PS_{5.25}Cl_{0.75}) for more than 500 cycle. Unraveling the structural evolution and specific hydrolysis mechanism of Li-argyrodite towards water and air and more in-depth understanding about the Li/Li-argyrodite interface could provide guidance for designing new Li-argyrodite electrolytes with good Li compatibility and air-stability.

(4) Solid-state batteries assembly and compatible anode for Li-argyrodites

Most electrochemical performance results reported to date are based on the laboratory model cells. The development of a feasible fabrication process for pouch cell is vital for future large-scale application. Significant research and development efforts have been invested, such as exploring organic solvents to improve the slurry-based processes. The recent work reported by Samsung has shown promising Li-argyrodite-based solid-state batteries using a Li-free anode (Ag-C compound anode) and demonstrated stable cycling performance over 1000 cycles at 60 °C. For future anode designs for Li-argyrodite based batteries, Li-free anodes are of great interests.

Declaration of Competing Interest

The authors declare that they have no known competing financial interests or personal relationships that could have appeared to influence the work reported in this paper.

Acknowledgements

This work was supported by Natural Sciences and Engineering Research Council of Canada (NSERC), Canada Research Chair Program (CRC), Ontario Research Fund (ORF), Canada Foundation of Innovation (CFI), and Western University.

Appendix A. Supporting information

Supplementary data associated with this article can be found in the online version at [doi:10.1016/j.nanoen.2021.105858](https://doi.org/10.1016/j.nanoen.2021.105858).

References

- [1] B. Scrosati, Recent advances in lithium ion battery materials, *Electrochim. Acta* 45 (2000) 2461–2466.
- [2] C. Yu, S. Ganapathy, E.R. van Eck, L. van Eijck, N. de Klerk, E.M. Kelder, M. Wagemaker, Investigation of Li-ion transport in Li₇P₃S₁₁ and solid-state lithium batteries, *J. Energy Chem.* 38 (2019) 1–7.
- [3] Z. Zheng, H.-H. Wu, H. Liu, Q. Zhang, X. He, S. Yu, V. Petrova, J. Feng, R. Kostecki, P. Liu, Achieving fast and durable lithium storage through amorphous FeP nanoparticles encapsulated in ultrathin 3D P-doped porous carbon nanosheets, *ACS Nano* 14 (2020) 9545–9561.
- [4] E. Quartarone, P. Mustarelli, Electrolytes for solid-state lithium rechargeable batteries: recent advances and perspectives, *Chem. Soc. Rev.* 40 (2011) 2525–2540.
- [5] E.P. Roth, C.J. Orendorff, How electrolytes influence battery safety, *Interface Mag.* 21 (2012) 45–49.
- [6] X. Yang, J. Luo, X. Sun, Towards high-performance solid-state Li-S batteries: from fundamental understanding to engineering design, *Chem. Soc. Rev.* 49 (2020) 2140–2195.
- [7] M. Tatsumisago, M. Nagao, A. Hayashi, Recent development of sulfide solid electrolytes and interfacial modification for all-solid-state rechargeable lithium batteries, *J. Asian Ceram. Soc.* 1 (2013) 17–25.
- [8] Q. Zhang, H. Chen, L. Luo, B. Zhao, H. Luo, X. Han, J. Wang, C. Wang, Y. Yang, T. Zhu, Harnessing the concurrent reaction dynamics in active Si and Ge to achieve high performance lithium-ion batteries, *Energy Environ. Sci.* 11 (2018) 669–681.
- [9] A. Opitz, P. Badami, L. Shen, K. Vignarooban, A.M. Kannan, Can Li-Ion batteries be the panacea for automotive applications, *Renew. Sustain. Energy Rev.* 68 (2017) 685–692.
- [10] L. Lu, X. Han, J. Li, J. Hua, M. Ouyang, A review on the key issues for lithium-ion battery management in electric vehicles, *J. Power Sour.* 226 (2013) 272–288.
- [11] J.C. Bachman, S. Muy, A. Grimaud, H.-H. Chang, N. Pour, S.F. Lux, O. Paschos, F. Maglia, S. Lupart, P. Lamp, Inorganic solid-state electrolytes for lithium batteries: mechanisms and properties governing ion conduction, *Chem. Rev.* 116 (2016) 140–162.
- [12] J. Gao, Y.-S. Zhao, S.-Q. Shi, H. Li, Lithium-ion transport in inorganic solid state electrolyte, *Chin. Phys. B* 25 (2016), 018211.
- [13] J. Janek, W.G. Zeier, A solid future for battery development, *Nat. Energy* 1 (2016) 16141.
- [14] X. Yao, B. Huang, J. Yin, G. Peng, Z. Huang, C. Gao, D. Liu, X. Xu, All-solid-state lithium batteries with inorganic solid electrolytes: review of fundamental science, *Chin. Phys. B* 25 (2016), 018802.
- [15] K. Takada, Progress and prospective of solid-state lithium batteries, *Acta Mater.* 61 (2013) 759–770.
- [16] W. Wu, J. Duan, J. Wen, Y. Chen, X. Liu, L. Huang, Z. Wang, S. Deng, Y. Huang, W. Luo, A writable lithium metal ink, *Sci. China Chem.* 63 (2020) 1483–1489.
- [17] J.W. Fergus, Ceramic and polymeric solid electrolytes for lithium-ion batteries, *J. Power Sour.* 195 (2010) 4554–4569.
- [18] K. Takada, Progress in solid electrolytes toward realizing solid-state lithium batteries, *J. Power Sour.* 394 (2018) 74–85.
- [19] Z. Zheng, P. Li, J. Huang, H. Liu, Y. Zao, Z. Hu, L. Zhang, H. Chen, M.-S. Wang, D.-L. Peng, High performance columnar-like Fe₂O₃@carbon composite anode via yolk@shell structural design, *J. Energy Chem.* 41 (2020) 126–134.
- [20] P. Knauth, Inorganic solid Li ion conductors: an overview, *Solid State Ion.* 180 (2009) 911–916.
- [21] J. Ma, B. Chen, L. Wang, G. Cui, Progress and prospect on failure mechanisms of solid-state lithium batteries, *J. Power Sour.* 392 (2018) 94–115.
- [22] J. Duan, Y. Zheng, W. Luo, W. Wu, T. Wang, Y. Xie, S. Li, J. Li, Y. Huang, Is graphite lithiophobic or lithiophilic? *Natl. Sci. Rev.* 7 (2020) 1208–1217.
- [23] T. Minami, A. Hayashi, M. Tatsumisago, Recent progress of glass and glass-ceramics as solid electrolytes for lithium secondary batteries, *Solid State Ion.* 177 (2006) 2715–2720.
- [24] A. Kulkarni, H. Maiti, A. Paul, Fast ion conducting lithium glasses—review, *Bull. Mater. Sci.* 6 (1984) 201–221.
- [25] M. Tatsumisago, A. Hayashi, Sulfide glass-ceramic electrolytes for all-solid-state lithium and sodium batteries, *Int. J. Appl. Glass Sci.* 5 (2014) 226–235.
- [26] Y.S. Jung, D.Y. Oh, Y.J. Nam, K.H. Park, Issues and challenges for bulk-type all-solid-state rechargeable lithium batteries using sulfide solid electrolytes, *Isr. J. Chem.* 55 (2015) 472–485.
- [27] Uv Alpen, A. Rabenau, G. Talat, Ionic conductivity in Li₃N single crystals, *Appl. Phys. Lett.* 30 (1977) 621–623.
- [28] T. Lapp, S. Skaarup, A. Hooper, Ionic conductivity of pure and doped Li₃N, *Solid State Ion.* 11 (1983) 97–103.
- [29] M. Matsuo, Si Orimo, Lithium fast-ionic conduction in complex hydrides: review and prospects, *Adv. Energy Mater.* 1 (2011) 161–172.
- [30] L. Duchêne, A. Remhof, H. Hagemann, C. Battaglia, Status and prospects of hydroborate electrolytes for all-solid-state batteries, *Energy Storage Mater.* 25 (2020) 782–794.
- [31] P.E. de Jongh, D. Blanchard, M. Matsuo, T.J. Udovic, S. Orimo, Complex hydrides as room-temperature solid electrolytes for rechargeable batteries, *Appl. Phys. A* 122 (2016) 251.
- [32] X. Li, J. Liang, N. Chen, J. Luo, K.R. Adair, C. Wang, M.N. Banis, T.-K. Sham, L. Zhang, S. Zhao, S. Lu, H. Huang, R. Li, X. Sun, Water-mediated synthesis of a superionic halide solid electrolyte, *Angew. Chem. Int. Ed.* 58 (2019) 16427–16432.
- [33] X. Li, J. Liang, J. Luo, M.N. Banis, C. Wang, W. Li, S. Deng, C. Yu, F. Zhao, Y. Hu, Air-stable Li₃InCl₆ electrolyte with high voltage compatibility for all-solid-state batteries, *Energy Environ. Sci.* 12 (2019) 2665–2671.
- [34] T. Asano, A. Sakai, S. Ouchi, M. Sakaida, A. Miyazaki, S. Hasegawa, Solid halide electrolytes with high lithium-ion conductivity for application in 4 V class bulk-type all-solid-state batteries, *Adv. Mater.* 30 (2018), 1803075.
- [35] W. Xiao, J. Wang, L. Fan, J. Zhang, X. Li, Recent advances in Li_{1+x}Al_xTi_{2-x}(PO₄)₃ solid-state electrolyte for safe lithium batteries, *Energy Storage Mater.* 19 (2019) 379–400.
- [36] C. Cao, Z.-B. Li, X.-L. Wang, X.-B. Zhao, W.-Q. Han, Recent advances in inorganic solid electrolytes for lithium batteries, *Front. Energy Res.* 2 (2014) 25.

- [37] N. Kamaya, K. Homma, Y. Yamakawa, M. Hirayama, R. Kanno, M. Yonemura, T. Kamiyama, Y. Kato, S. Hama, K. Kawamoto, A lithium superionic conductor, *Nat. Mater.* 10 (2011) 682–686.
- [38] Y. Kato, S. Hori, T. Saito, K. Suzuki, M. Hirayama, A. Mitsui, M. Yonemura, H. Iba, R. Kanno, High-power all-solid-state batteries using sulfide superionic conductors, *Nat. Energy* 1 (2016) 16030.
- [39] P. Adeli, J.D. Bazak, K.H. Park, I. Kochetkov, A. Huq, G.R. Goward, L.F. Nazar, Boosting solid-state diffusivity and conductivity in lithium superionic argyrodites by halide substitution, *Angew. Chem. Int. Ed.* 58 (2019) 8681–8686.
- [40] H.J. Deiseroth, S.T. Kong, H. Eckert, J. Vannahme, C. Reiner, T. Zaiss, M. Schlosser, $\text{Li}_6\text{PS}_5\text{X}$: a class of crystalline Li-rich solids with an unusually high Li^+ mobility, *Angew. Chem. Int. Ed.* 47 (2008) 755–758.
- [41] R.P. Rao, S. Adams, Studies of lithium argyrodite solid electrolytes for all-solid-state batteries: studies of lithium argyrodite solid electrolytes, *Phys. Status Solidi (a)* 208 (2011) 1804–1807.
- [42] R.P. Rao, N. Sharma, V. Peterson, S. Adams, Formation and conductivity studies of lithium argyrodite solid electrolytes using in-situ neutron diffraction, *Solid State Ion.* 230 (2013) 72–76.
- [43] P.R. Rayavarapu, N. Sharma, V.K. Peterson, S. Adams, Variation in structure and Li^+ -ion migration in argyrodite-type $\text{Li}_6\text{PS}_5\text{X}$ (X = Cl, Br, I) solid electrolytes, *J. Solid State Electrochem.* 16 (2012) 1807–1813.
- [44] S. Boulineau, M. Courty, J.-M. Tarascon, V. Viallet, Mechanochemical synthesis of Li-argyrodite $\text{Li}_6\text{PS}_5\text{X}$ (X = Cl, Br, I) as sulfur-based solid electrolytes for all solid state batteries application, *Solid State Ion.* 221 (2012) 1–5.
- [45] C. Yu, S. Ganapathy, N.J.J. de Klerk, I. Roslon, E.R.H. van Eck, A.P.M. Kentgens, M. Wagemaker, Unravelling Li^+ -ion transport from picoseconds to seconds: bulk versus interfaces in an argyrodite $\text{Li}_6\text{PS}_5\text{Cl}$ - Li_2S all-solid-state Li^+ -ion battery, *J. Am. Chem. Soc.* 138 (2016) 11192–11201.
- [46] C. Yu, S. Ganapathy, J. Hageman, L. van Eijck, E.R. van Eck, L. Zhang, T. Schwietert, S. Basak, E.M. Kelder, M. Wagemaker, Facile synthesis toward the optimal structure-conductivity characteristics of the argyrodite $\text{Li}_6\text{PS}_5\text{Cl}$ solid-state electrolyte, *ACS Appl. Mater. Interfaces* 10 (2018) 33296–33306.
- [47] C. Yu, S. Ganapathy, E.R.H. van Eck, L. van Eijck, S. Basak, Y. Liu, L. Zhang, H. Zandbergen, M. Wagemaker, Revealing the relation between the structure, Li^+ -ion conductivity and solid-state battery performance of the argyrodite $\text{Li}_6\text{PS}_5\text{Br}$ solid electrolyte, *J. Mater. Chem. A* 5 (2017) 21178–21188.
- [48] C. Yu, J. Hageman, S. Ganapathy, L. van Eijck, L. Zhang, K.R. Adair, X. Sun, M. Wagemaker, Tailoring $\text{Li}_6\text{PS}_5\text{Br}$ ionic conductivity and understanding of its role in cathode mixtures for high performance all-solid-state Li^+ -S batteries, *J. Mater. Chem. A* 7 (2019) 10412–10421.
- [49] C. Yu, Y. Li, M. Willans, Y. Zhao, K.R. Adair, F. Zhao, W. Li, S. Deng, J. Liang, M. N. Banis, Superionic conductivity in lithium argyrodite solid-state electrolyte by controlled Cl-doping, *Nano Energy* 69 (2020), 104396.
- [50] C. Yu, L. van Eijck, S. Ganapathy, M. Wagemaker, Synthesis, structure and electrochemical performance of the argyrodite $\text{Li}_6\text{PS}_5\text{Cl}$ solid electrolyte for Li^+ -ion solid state batteries, *Electrochim. Acta* 215 (2016) 93–99.
- [51] Z. Zhang, L. Zhang, Y. Liu, C. Yu, X. Yan, B. Xu, L.-m Wang, Synthesis and characterization of argyrodite solid electrolytes for all-solid-state Li^+ -ion batteries, *J. Alloy. Compd.* 747 (2018) 227–235.
- [52] Z. Zhang, L. Zhang, X. Yan, H. Wang, Y. Liu, C. Yu, X. Cao, L. van Eijck, B. Wen, All-in-one improvement toward $\text{Li}_6\text{PS}_5\text{Br}$ -based solid electrolytes triggered by compositional tune, *J. Power Sources* 410–411 (2019) 162–170.
- [53] R. Beeken, J. Garbe, J. Gillis, N. Petersen, B. Podoll, M. Stoneman, Electrical conductivities of the $\text{Ag}_6\text{PS}_5\text{X}$ and the $\text{Cu}_6\text{PSe}_5\text{X}$ (X = Br, I) argyrodites, *J. Phys. Chem. Solids* 66 (2005) 882–886.
- [54] C.C. Koch, J. Whittenberger, Mechanical milling/alloying of intermetallics, *Intermetallics* 4 (1996) 339–355.
- [55] S. Wang, Y. Zhang, X. Zhang, T. Liu, Y.-H. Lin, Y. Shen, L. Li, C.-W. Nan, High-conductivity argyrodite $\text{Li}_6\text{PS}_5\text{Cl}$ solid electrolytes prepared via optimized sintering processes for all-solid-state lithium-sulfur batteries, *ACS Appl. Mater. Interfaces* 10 (2018) 42279–42285.
- [56] S. Yubuchi, M. Uematsu, C. Hotehama, A. Sakuda, A. Hayashi, M. Tatsumisago, An argyrodite sulfide-based superionic conductor synthesized by a liquid-phase technique with tetrahydrofuran and ethanol, *J. Mater. Chem. A* 7 (2019) 558–566.
- [57] S. Yubuchi, S. Teragawa, K. Aso, K. Tadanaga, A. Hayashi, M. Tatsumisago, Preparation of high lithium-ion conducting $\text{Li}_6\text{PS}_5\text{Cl}$ solid electrolyte from ethanol solution for all-solid-state lithium batteries, *J. Power Sour.* 293 (2015) 941–945.
- [58] S. Yubuchi, M. Uematsu, M. Deguchi, A. Hayashi, M. Tatsumisago, Lithium-ion-conducting argyrodite-type $\text{Li}_6\text{PS}_5\text{X}$ (X = Cl, Br, I) solid electrolytes prepared by a liquid-phase technique using ethanol as a solvent, *ACS Appl. Energy Mater.* 1 (2018) 3622–3629.
- [59] N.C. Rosero-Navarro, A. Miura, K. Tadanaga, Composite cathode prepared by argyrodite precursor solution assisted by dispersant agents for bulk-type all-solid-state batteries, *J. Power Sour.* 396 (2018) 33–40.
- [60] D.A. Ziolkowska, W. Arnold, T. Druffel, M. Sunkara, H. Wang, Rapid and economic synthesis of a Li_7PS_6 solid electrolyte from a liquid approach, *ACS Appl. Mater. Interfaces* 11 (2019) 6015–6021.
- [61] S. Chida, A. Miura, N.C. Rosero-Navarro, M. Higuchi, N.H. Phuc, H. Muto, A. Matsuda, K. Tadanaga, Liquid-phase synthesis of $\text{Li}_6\text{PS}_5\text{Br}$ using ultrasonication and application to cathode composite electrodes in all-solid-state batteries, *Ceram. Int.* 44 (2018) 742–746.
- [62] Z. Zhang, L. Zhang, Y. Liu, X. Yan, B. Xu, L.-m Wang, One-step solution process toward formation of $\text{Li}_6\text{PS}_5\text{Cl}$ argyrodite solid electrolyte for all-solid-state lithium-ion batteries, *J. Alloy. Compd.* 812 (2020), 152103.
- [63] S. Choi, J. Ann, J. Do, S. Lim, C. Park, D. Shin, Application of rod-like $\text{Li}_6\text{PS}_5\text{Cl}$ directly synthesized by a liquid phase process to sheet-type electrodes for all-solid-state lithium batteries, *J. Electrochem. Soc.* 166 (2019) A5193–A5200.
- [64] L. Zhou, K.-H. Park, X. Sun, F. Lalère, T. Adermann, P. Hartmann, L.F. Nazar, Solvent-engineered design of argyrodite $\text{Li}_6\text{PS}_5\text{X}$ (X = Cl, Br, I) solid electrolytes with high ionic conductivity, *ACS Energy Lett.* 4 (2018) 265–270.
- [65] I. Hanghofer, B. Gadermaier, H.M.R. Wilkening, Fast rotational dynamics in argyrodite-type $\text{Li}_6\text{PS}_5\text{X}$ (X: Cl, Br, I) as seen by ^{31}P nuclear magnetic relaxation—on cation-anion coupled transport in thiophosphates, *Chem. Mater.* 31 (2019) 4591–4597.
- [66] I. Hanghofer, M. Brinek, S. Eisbacher, B. Bitschnau, M. Volck, V. Hennige, I. Hanzu, D. Rettenwander, H. Wilkening, Substitutional disorder: structure and ion dynamics of the argyrodites $\text{Li}_6\text{PS}_5\text{Cl}$, $\text{Li}_6\text{PS}_5\text{Br}$ and $\text{Li}_6\text{PS}_5\text{I}$, *Phys. Chem. Chem. Phys.* 21 (2019) 8489–8507.
- [67] A. Gautam, M. Sadowski, M. Ghidui, N. Minafra, A. Senyshyn, K. Albe, W. G. Zeier, Engineering the Site-Disorder and Lithium Distribution in the Lithium Superionic Argyrodite $\text{Li}_6\text{PS}_5\text{Br}$, *Adv. Energy Mater.* 11 (2021), 2003369.
- [68] R. Schlenker, A.-L. Hansen, A. Senyshyn, T. Zinkevich, M. Knapp, T. Hupfer, H. Ehrenberg, S. Indris, Structure and diffusion pathways in $\text{Li}_6\text{PS}_5\text{Cl}$ argyrodite from neutron diffraction, pair-distribution function analysis, and NMR, *Chem. Mater.* 32 (2020) 8420–8430.
- [69] M.A. Kraft, S.P. Culver, M. Calderon, F. Böcher, T. Krauskopf, A. Senyshyn, C. Dietrich, A. Zevalkink, Jr Janek, W.G. Zeier, Influence of lattice polarizability on the ionic conductivity in the lithium superionic argyrodites $\text{Li}_6\text{PS}_5\text{X}$ (X = Cl, Br, I), *J. Am. Chem. Soc.* 139 (2017) 10909–10918.
- [70] N.J. De Klerk, I. Roslon, M. Wagemaker, *Chem. Mater.* 28 (2016) 7955–7963.
- [71] S. Ganapathy, C. Yu, E.R. Van Eck, M. Wagemaker, Peeking across grain boundaries in a solid-state ionic conductor, *ACS Energy Lett.* 4 (2019) 1092–1097.
- [72] V. Epp, Ozl Gn, H.-Jr Deiseroth, M. Wilkening, Highly mobile ions: low-temperature NMR directly probes extremely fast Li^+ hopping in argyrodite-type $\text{Li}_6\text{PS}_5\text{Br}$, *J. Phys. Chem. Lett.* 4 (2013) 2118–2123.
- [73] J.A. Dawson, P. Canepa, T. Famprikis, C. Masquelier, M.S. Islam, Atomic-scale influence of grain boundaries on Li^+ -ion conduction in solid electrolytes for all-solid-state batteries, *J. Am. Chem. Soc.* 140 (2018) 362–368.
- [74] R. Böhmer, K. Jeffrey, M. Vogel, Solid-state Li^+ NMR with applications to the translational dynamics in ion conductors, *Prog. Nucl. Magn. Reson. Spectrosc.* 50 (2007) 87–174.
- [75] H.M. Chen, C. Maohua, S. Adams, Stability and ionic mobility in argyrodite-related lithium-ion solid electrolytes, *Phys. Chem. Chem. Phys.* 17 (2015) 16494–16506.
- [76] S.T. Kong, H.J. Deiseroth, J. Maier, V. Nickel, K. Weichert, C. Reiner, $\text{Li}_6\text{PO}_5\text{Br}$ and $\text{Li}_6\text{PO}_5\text{Cl}$: the first lithium-oxide-argyrodites, *Z. Anorg. Allg. Chem.* 636 (2010) 1920–1924.
- [77] A. Baktash, J.C. Reid, T. Roman, D.J. Searles, Diffusion of lithium ions in Lithium-argyrodite solid-state electrolytes, *npj Comput. Mater.* 6 (2020) 162.
- [78] W.D. Jung, J.-S. Kim, S. Choi, S. Kim, M. Jeon, H.-G. Jung, K.Y. Chung, J.-H. Lee, B.-K. Kim, J.-H. Lee, H. Kim, Superionic halogen-rich Li-argyrodites using in situ nanocrystal nucleation and rapid crystal growth, *Nano Lett.* 20 (2020) 2303–2309.
- [79] Z. Zhu, I.-H. Chu, S.P. Ong, $\text{Li}_3\text{Y}(\text{PS}_4)_2$ and $\text{Li}_5\text{PS}_4\text{Cl}_2$: new lithium superionic conductors predicted from silver thiophosphates using efficiently tiered ab initio molecular dynamics simulations, *Chem. Mater.* 29 (2017) 2474–2484.
- [80] C. Yu, Y. Li, W. Li, K.R. Adair, F. Zhao, M. Willans, J. Liang, Y. Zhao, C. Wang, S. Deng, R. Li, H. Huang, S. Lu, T.-K. Sham, Y. Huang, X. Sun, Enabling ultrafast ionic conductivity in Br-based lithium argyrodite electrolytes for solid-state batteries with different anodes, *Energy Storage Mater.* 30 (2020) 238–249.
- [81] P. Adeli, J.D. Bazak, A. Huq, G.R. Goward, L.F. Nazar, Influence of aliovalent cation substitution and mechanical compression on Li^+ -ion conductivity and diffusivity in argyrodite solid electrolytes, *Chem. Mater.* 33 (2021) 146–157.
- [82] X. Feng, P.-H. Chien, Y. Wang, S. Patel, P. Wang, H. Liu, M. Immediato-Scotto, Y.-Y. Hu, Enhanced ion conduction by enforcing structural disorder in Li-deficient argyrodites $\text{Li}_{6-x}\text{PS}_{5-x}\text{Cl}_{1+x}$, *Energy Storage Mater.* 30 (2020) 67–73.
- [83] P. Wang, H. Liu, S. Patel, X. Feng, P.-H. Chien, Y. Wang, Y.-Y. Hu, Fast ion conduction and its origin in $\text{Li}_{6-x}\text{PS}_{5-x}\text{Br}_{1+x}$, *Chem. Mater.* 32 (2020) 3833–3840.
- [84] Z. Zhang, J. Zhang, H. Jia, L. Peng, T. An, J. Xie, Enhancing ionic conductivity of solid electrolyte by lithium substitution in halogenated Li-Argyrodite, *J. Power Sour.* 450 (2020), 227601.
- [85] O. Pecher, S.T. Kong, T. Goebel, V. Nickel, K. Weichert, C. Reiner, H.J. Deiseroth, J. Maier, F. Haarmann, D. Zahn, Atomistic characterisation of Li^+ mobility and conductivity in $\text{Li}_{7-x}\text{PS}_{6-x}\text{I}_x$ argyrodites from molecular dynamics simulations, solid-state NMR, and impedance spectroscopy, *Chem. A Eur. J.* 16 (2010) 8347–8354.
- [86] T. Berges, S.P. Culver, N. Minafra, R. Koerver, W.G. Zeier, Competing structural influences in the Li superionic conducting argyrodites $\text{Li}_6\text{PS}_{5-x}\text{Se}_x\text{Br}$ ($0 \leq x \leq 1$) upon Se substitution, *Inorg. Chem.* 57 (2018) 13920–13928.
- [87] Y. Inoue, K. Suzuki, N. Matsui, M. Hirayama, R. Kanno, Synthesis and structure of novel lithium-ion conductor $\text{Li}_7\text{Ge}_2\text{PS}_{12}$, *J. Solid State Chem.* 246 (2017) 334–340.
- [88] M.A. Kraft, S. Ohno, T. Zinkevich, R. Koerver, S.P. Culver, T. Fuchs, A. Senyshyn, S. Indris, B.J. Morgan, W.G. Zeier, Inducing high ionic conductivity in the lithium superionic argyrodites $\text{Li}_{6+x}\text{P}_{1-x}\text{Ge}_x\text{S}_7\text{I}$ for all-solid-state batteries, *J. Am. Chem. Soc.* 140 (2018) 16330–16339.
- [89] M. Brinek, C. Hiebl, H.M.R. Wilkening, Understanding the origin of enhanced Li^+ -ion transport in nanocrystalline argyrodite-type $\text{Li}_6\text{PS}_5\text{I}$, *Chem. Mater.* 32 (2020) 4754–4766.

- [90] H. Schneider, S.J. Sedlmaier, H. Du, T. Kelley, K. Leitner, J. ter Maat, C. Scordilis-Kelley, A. Mudalige, J. Kulisch, L. Schneider, Stabilization of highly conductive lithium argyrodites by means of lithium substitution: the case of $\text{Li}_6\text{Fe}_0.5\text{PS}_6$, *ChemistrySelect* 4 (2019) 3351–3354.
- [91] Z. Zhang, Y. Sun, X. Duan, L. Peng, H. Jia, Y. Zhang, B. Shan, J. Xie, Design and synthesis of room temperature stable Li-argyrodite superionic conductors via cation doping, *J. Mater. Chem. A* 7 (2019) 2717–2722.
- [92] N. Minafra, S.P. Culver, T. Krauskopf, A. Senyshyn, W.G. Zeier, Effect of Si substitution on the structural and transport properties of superionic Li-argyrodites, *J. Mater. Chem. A* 6 (2018) 645–651.
- [93] Y. Lee, J. Jeong, H.-D. Lim, S.-O. Kim, H.-G. Jung, K.Y. Chung, S. Yu, Superionic Si-substituted lithium argyrodite sulfide electrolyte $\text{Li}_{6+x}\text{Sb}_{1-x}\text{Si}_x\text{S}_5$ for all-solid-state batteries, *ACS Sustain. Chem. Eng.* 9 (2021) 120–128.
- [94] J. Zhang, L. Li, C. Zheng, Y. Xia, Y. Gan, H. Huang, C. Liang, X. He, X. Tao, W. Zhang, Silicon-doped argyrodite solid electrolyte $\text{Li}_6\text{PS}_5\text{I}$ with improved ionic conductivity and interfacial compatibility for high-performance all-solid-state lithium batteries, *ACS Appl. Mater. Interfaces* 12 (2020) 41538–41545.
- [95] S. Ohno, B. Helm, T. Fuchs, G. Dewald, M.A. Kraft, S.P. Culver, A. Senyshyn, W. G. Zeier, Further evidence for energy landscape flattening in the superionic argyrodites $\text{Li}_{6+x}\text{P}_{1-x}\text{M}_x\text{S}_5$ (M = Si, Ge, Sn, *Chem. Mater.* 31 (2019) 4936–4944.
- [96] F. Zhao, J. Liang, C. Yu, Q. Sun, X. Li, K. Adair, C. Wang, Y. Zhao, S. Zhang, W. Li, A versatile Sn-substituted argyrodite sulfide electrolyte for all-solid-state Li metal batteries, *Adv. Energy Mater.* 10 (2020), 1903422.
- [97] L. Zhou, A. Assoud, Q. Zhang, X. Wu, L.F. Nazar, New family of argyrodite thioantimonate lithium superionic conductors, *J. Am. Chem. Soc.* 141 (2019) 19002–19013.
- [98] H. Schneider, H. Du, T. Kelley, K. Leitner, J. ter Maat, C. Scordilis-Kelley, R. Sanchez-Carrera, I. Kovalev, A. Mudalige, J. Kulisch, A novel class of halogen-free, super-conductive lithium argyrodites: synthesis and characterization, *J. Power Sour.* 366 (2017) 151–160.
- [99] M. Xu, Y. Sun, S. Hori, K. Suzuki, W. Huang, M. Hirayama, R. Kanno, A lithium conductor $\text{Li}_{6.96}\text{Sn}_{1.55}\text{Si}_{1.71}\text{P}_{0.8}\text{S}_{12}$ with a cubic argyrodite-type structure in the $\text{Li}_2\text{S}-\text{SnS}_2-\text{SiS}_2-\text{P}_2\text{S}_5$ system: synthesis, structure, and electrochemical properties, *Solid State Ion.* 356 (2020), 115458.
- [100] W. Huang, K. Yoshino, S. Hori, K. Suzuki, M. Yonemura, M. Hirayama, R. Kanno, Superionic lithium conductor with a cubic argyrodite-type structure in the Li–Al–Si–S system, *J. Solid State Chem.* 270 (2019) 487–492.
- [101] W. Huang, L. Cheng, S. Hori, K. Suzuki, M. Yonemura, M. Hirayama, R. Kanno, Ionic conduction mechanism of a lithium superionic argyrodite in the Li–Al–Si–S–O system, *Mater. Adv.* 1 (2020) 334–340.
- [102] A. Sakuda, A. Yamauchi, S. Yubuchi, N. Kitamura, Y. Idemoto, A. Hayashi, M. Tatsumisago, Mechanochemically prepared $\text{Li}_2\text{S}-\text{P}_2\text{S}_5-\text{LiBH}_4$ solid electrolytes with an argyrodite structure, *ACS Omega* 3 (2018) 5453–5458.
- [103] F. Strauss, T. Zinkevich, S. Indris, T. Brezesinski, $\text{Li}_7\text{GeS}_5\text{Br}$ —an argyrodite Li-ion conductor prepared by mechanochemical synthesis, *Inorg. Chem.* 59 (2020) 12954–12959.
- [104] S. Boulineau, J.-M. Tarascon, J.-B. Leriche, V. Viallet, Electrochemical properties of all-solid-state lithium secondary batteries using Li-argyrodite $\text{Li}_6\text{PS}_5\text{Cl}$ as solid electrolyte, *Solid State Ion.* 242 (2013) 45–48.
- [105] F. Stadler, C. Fietzek, Crystalline halide substituted Li-argyrodites as solid electrolytes for lithium secondary batteries, *ECS Trans.* 25 (2009) 177–183.
- [106] C. Yu, S. Ganapathy, E.R. Van Eck, H. Wang, S. Basak, Z. Li, M. Wagemaker, Accessing the bottleneck in all-solid-state batteries, lithium-ion transport over the solid-electrolyte-electrode interface, *Nat. Commun.* 8 (2017) 1086.
- [107] Y. Zhu, X. He, Y. Mo, Origin of Outstanding Stability in the Lithium Solid Electrolyte Materials: Insights from Thermodynamic Analyses Based on First-Principles Calculations, *ACS Appl. Mater. Interfaces* 7 (2015) 23685–23693.
- [108] S. Wenzel, S.J. Sedlmaier, C. Dietrich, W.G. Zeier, J. Janek, Interfacial reactivity and interphase growth of argyrodite solid electrolytes at lithium metal electrodes, *Solid State Ion.* 318 (2018) 102–112.
- [109] J. Auvergniot, A. Cassel, J.-B. Ledeuil, V. Viallet, V. Seznec, Rm Dedryvère, Interface stability of argyrodite $\text{Li}_6\text{PS}_5\text{Cl}$ toward LiCoO_2 , $\text{LiNi}_{1/3}\text{Co}_{1/3}\text{Mn}_{1/3}\text{O}_2$, and LiMn_2O_4 in bulk all-solid-state batteries, *Chem. Mater.* 29 (2017) 3883–3890.
- [110] F. Walther, R. Koerver, T. Fuchs, S. Ohno, J. Sann, M. Rohnke, W.G. Zeier, Jr Janek, Visualization of the interfacial decomposition of composite cathodes in argyrodite-based all-solid-state batteries using time-of-flight secondary-ion mass spectrometry, *Chem. Mater.* 31 (2019) 3745–3755.
- [111] A. Banerjee, H. Tang, X. Wang, J.-H. Cheng, H. Nguyen, M. Zhang, D.H. Tan, T. A. Wynn, E.A. Wu, J.-M. Doux, Revealing nanoscale solid–solid interfacial phenomena for long-life and high-energy all-solid-state batteries, *ACS Appl. Mater. Interfaces* 11 (2019) 43138–43145.
- [112] Y. Zhou, C. Doerr, J. Kasemchainan, P.G. Bruce, M. Pasta, L.J. Hardwick, Observation of interfacial degradation of $\text{Li}_6\text{PS}_5\text{Cl}$ against lithium metal and LiCoO_2 via in situ electrochemical Raman microscopy, *Batter. Supercaps* 3 (2020) 647–652.
- [113] J. Zhang, C. Zheng, L. Li, Y. Xia, H. Huang, Y. Gan, C. Liang, X. He, X. Tao, W. Zhang, Unraveling the intra and intercycle interfacial evolution of $\text{Li}_6\text{PS}_5\text{Cl}$ -based all-solid-state lithium batteries, *Adv. Energy Mater.* 10 (2020), 1903311.
- [114] Y. Li, W. Arnold, J.B. Jasinski, A. Thapa, G. Sumanasekera, M. Sunkara, B. Narayanan, T. Druffel, H. Wang, Interface stability of LiCl-rich argyrodite $\text{Li}_6\text{PS}_5\text{Cl}$ with propylene carbonate boosts high-performance lithium batteries, *Electrochim. Acta* 363 (2020), 137128.
- [115] Z. Qiao-Bao, G. Zheng-Liang, Y. Yong, Advance in interface and characterizations of sulfide solid electrolyte materials, *Acta Phys. Sin.* 69 (2020), 228803.
- [116] H. Fu, Q. Yin, Y. Huang, H. Sun, Y. Chen, R. Zhang, Q. Yu, L. Gu, J. Duan, W. Luo, Reducing interfacial resistance by Na-SiO₂ composite anode for NASICON-based solid-state sodium battery, *ACS Mater. Lett.* 2 (2019) 127–132.
- [117] Q. Zhang, D. Cao, Y. Ma, A. Natan, P. Aurora, H. Zhu, Sulfide-based solid-state electrolytes: synthesis, stability, and potential for all-solid-state batteries, *Adv. Mater.* 31 (2019), 1901131.
- [118] Z. Zhang, Y. Shao, B. Lotsch, Y.-S. Hu, H. Li, J. Janek, L.F. Nazar, C.-W. Nan, J. Maier, M. Armand, High-performance lead-free piezoelectrics with local structural heterogeneity, *Energy Environ. Sci.* 11 (2018) 3531–3539.
- [119] R. Chen, Q. Li, X. Yu, L. Chen, H. Li, Approaching practically accessible solid-state batteries: stability issues related to solid electrolytes and interfaces, *Chem. Rev.* 120 (2020) 6820–6877.
- [120] L. Xu, S. Tang, Y. Cheng, K. Wang, J. Liang, C. Liu, Y.-C. Cao, F. Wei, L. Mai, Interfaces in solid-state lithium batteries, *Joule* 2 (2018) 1991–2015.
- [121] S. Xin, Y. You, S. Wang, H.-C. Gao, Y.-X. Yin, Y.-G. Guo, Solid-state lithium metal batteries promoted by nanotechnology: progress and prospects, *ACS Energy Lett.* 2 (2017) 1385–1394.
- [122] J. Kasemchainan, S. Zekoll, D. Spencer Jolly, Z. Ning, G.O. Hartley, J. Marrow, P. G. Bruce, Critical stripping current leads to dendrite formation on plating in lithium anode solid electrolyte cells, *Nat. Mater.* 18 (2019) 1105–1111.
- [123] J.M. Doux, H. Nguyen, D.H. Tan, A. Banerjee, X. Wang, E.A. Wu, C. Jo, H. Yang, Y.S. Meng, Stack pressure considerations for room-temperature all-solid-state lithium metal batteries, *Adv. Energy Mater.* 10 (2020), 1903253.
- [124] D.H. Tan, E.A. Wu, H. Nguyen, Z. Chen, M.A. Marple, J.-M. Doux, X. Wang, H. Yang, A. Banerjee, Y.S. Meng, Elucidating reversible electrochemical redox of $\text{Li}_6\text{PS}_5\text{Cl}$ solid electrolyte, *ACS Energy Lett.* 4 (2019) 2418–2427.
- [125] T.K. Schwietert, V.A. Arszewska, C. Wang, C. Yu, A. Vasileiadis, N.J. de Klerk, J. Hageman, T. Hupfer, I. Kerkamm, Y. Xu, Clarifying the relationship between redox activity and electrochemical stability in solid electrolytes, *Nat. Mater.* 19 (2020) 428–435.
- [126] M. Chen, S. Adams, High performance all-solid-state lithium/sulfur batteries using lithium argyrodite electrolyte, *J. Solid State Electrochem.* 19 (2015) 697–702.
- [127] J. Auvergniot, A. Cassel, D. Foix, V. Viallet, V. Seznec, R. Dedryvère, Redox activity of argyrodite $\text{Li}_6\text{PS}_5\text{Cl}$ electrolyte in all-solid-state Li-ion battery: an XPS study, *Solid State Ion.* 300 (2017) 78–85.
- [128] Y. Xiao, L.J. Miara, Y. Wang, G. Ceder, Computational screening of cathode coatings for solid-state batteries, *Joule* 3 (2019) 1252–1275.
- [129] S.P. Culver, R. Koerver, W.G. Zeier, J. Janek, On the functionality of coatings for cathode active materials in thiophosphate-based all-solid-state batteries, *Adv. Energy Mater.* 9 (2019), 1900626.
- [130] F. Strauss, J.H. Teo, J. Maibach, A.Y. Kim, A. Mazilkin, J. Janek, T. Brezesinski, Li_2ZrO_3 -coated NCM622 for application in inorganic solid-state batteries: role of surface carbonates in the cycling performance, *ACS Appl. Mater. Interfaces* 12 (2020) 57146–57154.
- [131] F. Zhao, Y. Zhao, J. Wang, Q. Sun, K. Adair, S. Zhang, J. Luo, J. Li, W. Li, Y. Sun, X. Li, J. Liang, C. Wang, R. Li, H. Huang, L. Zhang, S. Zhao, S. Lu, X. Sun, Tuning bifunctional interface for advanced sulfide-based all-solid-state batteries, *Energy Storage Mater.* 33 (2020) 139–146.
- [132] T. Chen, D. Zeng, L. Zhang, M. Yang, D. Song, X. Yan, C. Yu, Sn-O dual-doped Li-argyrodite electrolytes with enhanced electrochemical performance, *J. Energy Chem.* 59 (2021) 530–537.
- [133] F. Zhao, Q. Sun, C. Yu, S. Zhang, K. Adair, S. Wang, Y. Liu, Y. Zhao, J. Liang, C. Wang, X. Li, X. Li, W. Xia, R. Li, H. Huang, L. Zhang, S. Zhao, S. Lu, X. Sun, Ultrastable anode interface achieved by fluorinating electrolytes for all-solid-state Li metal batteries, *ACS Energy Lett.* 5 (2020) 1035–1043.
- [134] T. Chen, L. Zhang, Z. Zhang, P. Li, H. Wang, C. Yu, X. Yan, L. Wang, B. Xu, Argyrodite Solid Electrolyte with a Stable Interface and Superior Dendrite Suppression Capability Realized by ZnO Co-Doping, *ACS Appl. Mater. Interfaces* 11 (2019) 40808–40816.
- [135] W. Xiao, H. Xu, M. Xuan, Z. Wu, Y. Zhang, X. Zhang, S. Zhang, Y. Shen, G. Shao, Stable all-solid-state battery enabled with $\text{Li}_{6.25}\text{PS}_{5.25}\text{Cl}_{0.75}$ as fast ion-conducting electrolyte, *J. Energy Chem.* 53 (2021) 147–154.
- [136] F.J. Simon, M. Hanauer, A. Hens, F.H. Richter, Jr Janek, Properties of the interphase formed between argyrodite-type $\text{Li}_6\text{PS}_5\text{Cl}$ and polymer-based PEO10: LiTFSI, *ACS Appl. Mater. Interfaces* 11 (2019) 42186–42196.
- [137] F.J. Simon, M. Hanauer, F.H. Richter, Jr Janek, Interphase formation of PEO20: LiTFSI– $\text{Li}_6\text{PS}_5\text{Cl}$ composite electrolytes with lithium metal, *ACS Appl. Mater. Interfaces* 12 (2020) 11713–11723.
- [138] Y.-G. Lee, S. Fujiki, C. Jung, N. Suzuki, N. Yashiro, R. Omoda, D.-S. Ko, T. Shiratsuchi, T. Sugimoto, S. Ryu, *Nat. Energy* (2020) 1–10.
- [139] A. Miura, N.C. Rosero-Navarro, A. Sakuda, K. Tadanaga, N.H.H. Phuc, A. Matsuda, N. Machida, A. Hayashi, M. Tatsumisago, Liquid-phase syntheses of sulfide electrolytes for all-solid-state lithium battery, *Nat. Rev. Chem.* 3 (2019) 189–198.
- [140] D.H. Kim, D.Y. Oh, K.H. Park, Y.E. Choi, Y.J. Nam, H.A. Lee, S.-M. Lee, Y.S. Jung, Infiltration of solution-processable solid electrolytes into conventional Li-ion-battery electrodes for all-solid-state Li-ion batteries, *Nano Lett.* 17 (2017) 3013–3020.
- [141] D.H. Kim, Y.-H. Lee, Y.B. Song, H. Kwak, S.-Y. Lee, Y.S. Jung, Thin and flexible solid electrolyte membranes with ultrahigh thermal stability derived from solution-processable Li argyrodites for all-solid-state Li-ion batteries, *ACS Energy Lett.* 5 (2020) 718–727.
- [142] D.H. Kim, H.A. Lee, Y.B. Song, J.W. Park, S.-M. Lee, Y.S. Jung, Sheet-type $\text{Li}_6\text{PS}_5\text{Cl}$ -infiltrated Si anodes fabricated by solution process for all-solid-state lithium-ion batteries, *J. Power Sour.* 426 (2019) 143–150.

- [143] N.C. Rosero-Navarro, T. Kinoshita, A. Miura, M. Higuchi, K. Tadanaga, Effect of the binder content on the electrochemical performance of composite cathode using $\text{Li}_6\text{PS}_5\text{Cl}$ precursor solution in an all-solid-state lithium battery, *Ionics* 23 (2017) 1619–1624.
- [144] J. Zhang, H. Zhong, C. Zheng, Y. Xia, C. Liang, H. Huang, Y. Gan, X. Tao, W. Zhang, All-solid-state batteries with slurry coated $\text{LiNi}_{0.8}\text{Co}_{0.1}\text{Mn}_{0.1}\text{O}_2$ composite cathode and $\text{Li}_6\text{PS}_5\text{Cl}$ electrolyte: effect of binder content, *J. Power Sour.* 391 (2018) 73–79.
- [145] F. Strauss, D. Stepien, J. Maibach, L. Pfaffmann, S. Indris, P. Hartmann, T. Brezesinski, Influence of electronically conductive additives on the cycling performance of argyrodite-based all-solid-state batteries, *RSC Adv.* 10 (2020) 1114–1119.
- [146] H. Xu, Y. Yu, Z. Wang, G. Shao, A theoretical approach to address interfacial problems in all-solid-state lithium ion batteries: tuning materials chemistry for electrolyte and buffer coatings based on $\text{Li}_6\text{PA}_5\text{Cl}$ halide chalcogenides, *J. Mater. Chem. A* 7 (2019) 5239–5247.
- [147] S. Chen, D. Xie, G. Liu, J.P. Mwizerwa, Q. Zhang, Y. Zhao, X. Xu, X. Yao, Sulfide solid electrolytes for all-solid-state lithium batteries: structure, conductivity, stability and application, *Energy Storage Mater.* 14 (2018) 58–74.
- [148] H. Muramatsu, A. Hayashi, T. Ohtomo, S. Hama, M. Tatsumisago, Structural change of $\text{Li}_2\text{S}-\text{P}_2\text{S}_5$ sulfide solid electrolytes in the atmosphere, *Solid State Ion.* 182 (2011) 116–119.
- [149] T. Ohtomo, A. Hayashi, M. Tatsumisago, K. Kawamoto, Glass electrolytes with high ion conductivity and high chemical stability in the system $\text{LiI}-\text{Li}_2\text{O}-\text{Li}_2\text{S}-\text{P}_2\text{S}_5$, *Electrochemistry* 81 (2013) 428–431.
- [150] T. Ohtomo, A. Hayashi, M. Tatsumisago, K. Kawamoto, Characteristics of the $\text{Li}_2\text{O}-\text{Li}_2\text{S}-\text{P}_2\text{S}_5$ glasses synthesized by the two-step mechanical milling, *J. Non Cryst. Solids* 364 (2013) 57–61.
- [151] A. Hayashi, H. Muramatsu, T. Ohtomo, S. Hama, M. Tatsumisago, Improved chemical stability and cyclability in $\text{Li}_2\text{S}-\text{P}_2\text{S}_5-\text{P}_2\text{O}_5-\text{ZnO}$ composite electrolytes for all-solid-state rechargeable lithium batteries, *J. Alloy. Compd.* 591 (2014) 247–250.
- [152] A. Hayashi, H. Muramatsu, T. Ohtomo, S. Hama, M. Tatsumisago, Improvement of chemical stability of Li_3PS_4 glass electrolytes by adding M_xO_y ($\text{M} = \text{Fe}, \text{Zn}, \text{and Bi}$) nanoparticles, *J. Mater. Chem. A* 1 (2013) 6320–6326.
- [153] G. Liu, D. Xie, X. Wang, X. Yao, S. Chen, R. Xiao, H. Li, X. Xu, High air-stability and superior lithium ion conduction of $\text{Li}_{3+3}\text{P}_1-\text{Zn S}_4-\text{O}$ by aliovalent substitution of ZnO for all-solid-state lithium batteries, *Energy Storage Mater.* 17 (2019) 266–274.
- [154] G. Sahu, Z. Lin, J. Li, Z. Liu, N. Dudney, C. Liang, Air-stable, high-conduction solid electrolytes of arsenic-substituted Li_4SnS_4 , *Energy Environ. Sci.* 7 (2014) 1053–1058.



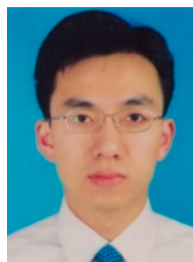
Dr. Chuang Yu received his Ph.D. degree from TU Delft (Delft, the Netherlands) in 2017. Afterward, he worked as a postdoctoral fellow in TU Delft (Delft, the Netherlands, 2017–2018) and Western University (London, Canada, 2018–2020). He is a Full Professor at the School of Electrical and Electronic Engineering at Huazhong University of Science and Technology (HUST). His current research interests focus on electrochemical energy storage and conversion. The synthesis, structure, dynamics, stability, and application of solid electrolytes in solid-state batteries is his main research field.



Feipeng Zhao is currently a Ph.D. candidate in Prof. Xueliang (Andy) Sun's Group at the University of Western Ontario, Canada. He received his B.S. degree and M.S. degree in Materials Science from Soochow University in 2014 and 2017, respectively. Currently, he is working on the synthesis and characterization of sulfide and halide electrolytes, and development of high-performance all-solid-state Li metal and Na metal batteries.



Jing Luo received her B.S. degree in Chemical Engineering from the University of Illinois-Urbana Champaign (U.S.A.) in 2013 and M.S. degree under the supervision of Prof. Nae-Lih Wu from National Taiwan University (Taiwan) in 2016. She is now pursuing her Ph.D. degree in Prof. Xueliang (Andy) Sun's group at University of Western Ontario, Canada. Her current research interests focus on solid electrolytes design and all-solid-state lithium batteries.



Prof. Long Zhang is a Professor at Yanshan University. He received his Ph.D. degree in Physical Chemistry from University of Vienna in 2010 and is honored with the den Loschmidt-Preis 2010 prize. Afterward, he worked as a postdoctoral fellow in Michigan State University for material research. His current research focuses on solid electrolytes and solid-state rechargeable batteries.



Prof. Xueliang (Andy) Sun is a Canada Research Chair in Development of Nanomaterials for Clean Energy, Fellow of the Royal Society of Canada and Canadian Academy of Engineering and Full Professor at the University of Western Ontario, Canada. Dr. Sun received his Ph.D. in materials chemistry in 1999 from the University of Manchester, UK, which he followed up by working as a postdoctoral fellow at the University of British Columbia, Canada and as a Research Associate at L'Institut National de la Recherche Scientifique (INRS), Canada. His current research interests are focused on advanced materials for electrochemical energy storage and conversion, including electrocatalysis in fuel cells and electrodes in lithium-ion batteries and metal-air batteries.